Calculation of Physical Processes at the LHC

A Dissertation

Presented for the

Doctor of Philosophy

Degree

The University of Tennessee, Knoxville

Usama Adnan al-Binni

December 2011

Acknowledgements

I wish to express deep gratitude to my advisor Dr. Siopsis for all he has done over the years. He has been a superb teacher, an invaluable guide and a wonderful thoughtful and patient person. It has been a privilege working with him. I also thank members of my committee, Dr. Freire, Dr. Guidry and Dr. Spanier for taking the time to read the work and provide constructive criticism and comments. I also thank Dr. Kamyshkov who was also a member but could not be available for the defence. I thank my parents, Adnan and Majida, for all they've done and their neverending support and faith in me, with my mother believing in me until her last day. I also thank my wife Amal for all her support and help and for being such a dependable partner. I also thank my daughter Leena who can bring a smile to my face no matter what I'm feeling. I thank my good friend Firas for being there for me whenever I needed him. I owe him so much. Finally, I'm also indebted to the University of Tennessee as an institution for giving opportunities like the one I took. The experience has been wonderful, instructive and and I'm sure it will be everlasting, and the people have been more than courteous and helpful, I'm grateful to all they've done, and in that regard my gratitude goes especially to Dr. Breinig for all her efforts.

Abstract

With the start of the age of the Large Hadron Collider (LHC) two challenges face theoreticians and computational physicists. The first is about understanding theories beyond the Standard Model and producing verifiable predictions that can be tested against what the LHC and subsequent machines would produce. The second is to improve computational methods so that the new experimental precision is matched by a theoretical one. But this improvement is also crucial for the detection of potential deviations from Standard Model predictions and possibly also finding the elusive Higgs. This work tries to address problems in both areas. In the first part we study the effects of adding tension in considering a black-hole on a brane. Such black-holes are predicted by some models as potential phenomena at the LHC. We calculate the effects of adding tension on observable quantities of black-holes, namely, quasi-normal mode frequencies and Hawking radiation, and we show how this improves predictions. In the second part we investigate the computational problem of extending the Britto-Cachazo-Feng-Witten (BCFW) method to 1-loop level. The BCFW has been successfully used in recent years to compute scattering amplitudes at tree-level by suitably complex-shifting external momenta and reducing diagrams to simpler ones. In our investigation we establish that the BCFW can be extended to 1-loop, which means that 1-loop integrands can be treated as trees and can be broken down further into even simpler trees using the BCFW. We explicitly look at the effects of the shift for the lowest three n-point cases, but also demonstrate how the result extends to arbitrary n.

Contents

List of Tables

List of Figures

Chapter 1

Introduction

1.1 Motivation and Outline

After many years of building, and several setbacks starting up, the Large Hadron Collider (LHC) is now finally up and running. Colliding two beams of protons at 14TeV center-of-mass energy, it is the most powerful machine of its kind ever built. For the first time in decades high-energy physics is being given a significant boost by the start of this project. Prospects of finding the Higgs, of discovering supersymmetry, of producing mini black-holes, and other potential discoveries, would open doors to radical developments in our understanding of what could possibly lie beyond the Standard Model of particle physics, which we know cannot be the complete story despite all its remarkable successes over the past few decades. For a review of the principles, physics and prospects of the LHC see Kane and Pierce (2008).

In order to start looking for new physics in the results of the LHC, the previously known results need to be reproduced to a higher precision, and this means that better computational methods are needed to go to higher orders in perturbation theory. But this is only one part of the endeavor. By detecting deviations from predictions of the Standard Model we need to be prepared with realistic predictions of the new physics capable of describing what we would be seeing in as much detail and precision as possible to differentiate between potential competing theories, but also to understand what we would be seeing. After all, most of the models beyond the Standard Model exist as pure theories with minimal input from experiment.

The present work was done as part of the effort to address these two needs; in the first part of the thesis we try to improve our theoretical understanding of observables of black-holes in the brane-world model by including brane-tension, a necessary ingredient in the string-inspired brane-world phenomenological models. The second part revolves around a theme in computation, a field that has witnessed many big improvements recently, both in theoretical and computerized implementations. The method we study, the Britto-Cachazo-Feng-Witten (BCFW) has implications both in gauge theory and perturbative quantum gravity.

This work is organized into two main parts, the first explores the only known exact solution describing a black-hole localized on a brane with finite tension. Following the outline, we review some of the preliminaries needed for both parts. Then, our investigation starts in chapter 2 by reviewing that solution and introducing the solution of the angular eigenvalue problem that appears in considering perturbations around the black-hole. In chapter 3 we study quasi-normal modes of these black-holes using the WentzelKramersBrillouin (WKB) method and in chapter 4 we investigate grey-body factors that appear in the study Hawking radiation, where we look at both low and high frequency regimes for various types of particles. The second part of this work is contained in chapter 5, where we consider the question of extending the powerful BCFW technique for calculating tree-level scattering amplitudes to loop-level amplitudes. This is followed by a statement of conclusions and outlook.

1.2 Brane-World Models and Extra Dimensions

The idea of extra dimensions has been a recurring theme throughout the physics of the 20th century. Starting with the pioneering work of Kaluza and Klein, all the way until modern day string theory, extra dimensions have proven to be a rich ground for extending and exploring ideas (for a mini review see Landsberg (2000)).

Using simple considerations based on Gauss's law in higher-dimensions, one can show that the scale of gravity would increase in the presence of extra dimensions. One implication of this is an enhancement of Schwarzschild radii:

$$r_h = r_S \sim \frac{1}{M_*}\left(\frac{M_{\mathrm{BH}}}{M_*}\right)^{\frac{1}{n+1}} \tag{1.1}$$

where M_* is the scale of gravity, M_{BH} is the black hole's mass, and n is the number of extra-dimensions. Such an enhancement means it is much easier to create black holes. Furthermore, the Hawking temperature depends on the number of extra dimensions, so that in principle, measuring it will yield a value of n:

$$T_H = \frac{n+1}{4\pi r_h} \tag{1.2}$$

Black holes in extra dimensions have been studied for quite some time (e.g. Myers and Perry (1986) and Tangherlini (1963)), for instance, the form of Schwarzschild metric in higher dimension has:

$$ds^2 = -f_n(r)dt^2 + \frac{1}{f_n(r)}dr^2 + r^2 d\Omega^2_{2+n} \tag{1.3}$$

and the angular part of the above metric is:

$$d\Omega^2_{2+n} = d\theta^2_{n+1} + \sin^2\theta_{n+1}\left(d\theta^2_n + \sin^2\theta_n\left(... + \sin^2\theta_2\left(d\theta^2_1 + \sin^2\theta_1 d\varphi^2\right)...\right)\right) \tag{1.4}$$

and the metric function $f(r)$ is given by:

$$f_n(r) = 1 - \left(\frac{r_h}{r}\right)^{n+1} \tag{1.5}$$

There are different ways to build models of higher-dimensional spacetime in brane-world scenarious. The first one, due to Antoniadis, Arkani-Hamed and Dimopoulos (ADD) and first explored in the pioneer works Arkani-Hamed et al. (1998), Antoniadis et al. (1998) and Arkani-Hamed et al. (1999). In this model we add n space-like extra dimensions without curvature. Generally, all these extra-dimensions are compactified to the same radius R, but not necessarily.

Another scheme, constructed by Randall and Sundrum (1998), assumes a 5-dimensional spacetime with non-factorizable geometry. In the so-called type RS-I model, two 3-branes are placed in a 5D anti-de Sitter space AdS_5 with an exponentially warped 5th dimension. In the discussion that follows we shall restrict discussion to ADD models, but we intend to include RS models in a future study.

1.3 Modern Computational Methods in Perturbative QCD and Gravity

The remarkable agreement we see between theoretical predictions and results from colliders is owed mainly to the fact that coupling in gauge theory is weak enough to allow computations through perturbation. This agreement is better in the electroweak sector than in the strong-interaction sector, which is governed by QCD. Experiments at the Tevatron in the past decade have demonstrated the importance of increased precision, but also, from the computational point of view, they showed that it is possible to go beyond leading order (LO) to next-to-leading order (NLO) and even next-to-next-to-leading order (NNLO) in far fewer cases.

Despite its intuitive nature, the use of Feynman diagrams for the calculation of scattering amplitude follows a rather inefficient algorithm that involves complicated and lengthy calculations that are redundant, and that is because vertices and propagators that make up the Feynman diagrams involve off-shell states. Numerous cancelations take place upon combining these gauge-dependent diagrams to form the gauge-independent total amplitude, and some gauge-independent terms repeat. The end result can often be cast in a very compact form, which indicates that there has to be a better deeper way of getting to that result without having to do all this needless work. Recent years have witnessed major advances in the computation of scattering amplitudes that depart from the traditional use of Feynman diagrams. Next, we present a general overview of these methods and some of their achievements in gauge theory, then we mention some of the connections gravity has to gauge theory and the impact of these developments on perturbative quantum gravity.

1.3.1 On-Shell Methods

In the 1960s an early attempt was made to use analytic properties of the S-matrix to 'bootstrap' calculations by reconstructing scattering amplitudes directly from their analytic properties (on-shell information) using branch-cuts and poles. Only limited development in that direction was achieved at the time (e.g. Olive (1964) and Chew (1966)), and the analyticity approach fell out of favor for the newer QCD techniques that were being developed. More recently (Bern et al. (1994) and Bern et al. (1995)) the approach has seen a vibrant revival that has witnessed a number of new calculations that up to that point had been considered computationally too hard, or even unattainable.

The approach is a generalization of the idea of using the unitarity of the S-matrix, which had already been used since the 1960s (e.g Cutkosky (1960), Feynman (1963)), where loop integrals are constructed from the branch cut information of the integral. This would use the usual physical momentum channels, but the newer version of unitary, dubbed *generalized unitarity* goes a step further by looking at cuts in unphysical channels as well, different singularities are considered and momenta are complexified. The idea of the unitarity method is to write down the 1-loop amplitude in terms of a basis of known master integrals (e.g. Bern et al. (2007)), we show the basis in figure (1.1) The problem then reduces to calculating the coefficients of these

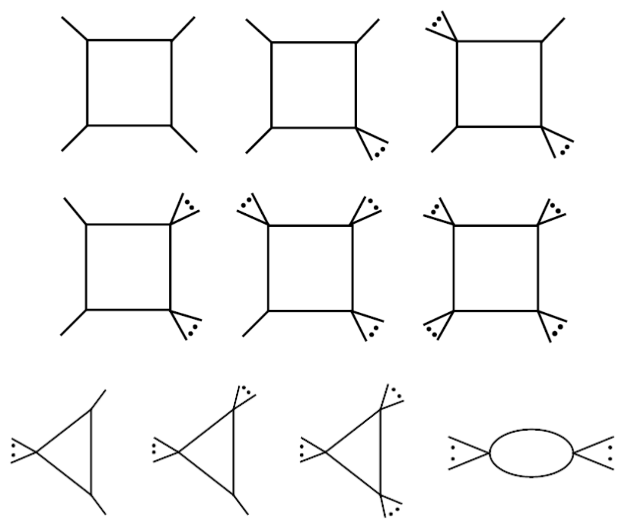

Figure 1.1: Basis of master integrals suitable used to write 1-loop integrals. The dots represent massive legs.

integrals. To get the full amplitude unitarity needs to be performed in $D = 4 - \varepsilon$ dimensions rather than four, otherwise additional rational terms need to be calculated separately from the coefficients of the master integrals. A review of advances and results has been conducted recently by Britto (2010) Ellis et al. (2011).

For trees, another approach was also developed in recent years based on an conjecture by Witten (2004) that scattering amplitudes in gauge theory can find simple representation in twistor space. Subsequently the method was developed by Britto et al. (2005a) and proved in Britto et al. (2005b). The main idea of the method is that by shifting two external legs in a tree diagram by a suitable complex momentum, it is possible to split the original tree into a sum of products of simpler trees. More details on how this works are provided in section 5.1

1.3.2 Quantum Gravity and Gauge Theory

It is a well-known fact that gravity poses problems when formulated as a point-like 4-dimensional quantum field theory. In particular, the resulting coupling constant κ is not dimensionless, but has the dimensions of length (in units of $\hbar = c = 1$):

$$\kappa = \sqrt{32\pi G_{\mathrm{N}}} \tag{1.6}$$

By power counting the theory is then non-renormalizable, as demonstrated for example in a classic paper by 't Hooft and Veltman (1974). No one knows of a symmetry so far that controls the divergences and construct an ultra-violet finite quantum theory of gravity. The intuitive conclusion is that if such a construction is to be made possible one has to go beyond conventional Einstein gravity in the high-energy limit. In the framework of string theory divergences are controlled by the introduction of a new scale in the form of string tension, which acts as a cut-off making the theory finite to all orders. But one wonders if it is not possible to do this in a point-like theory possessing enough symmetry. The only way to know a theory is divergent or not is to actually compute the divergence, but because of the technical difficulties involved, not many higher-order explicit calculations have been carried out, and the claims of divergence have mostly depended on power-counting arguments. This story, however, has changed over the last few years for two reasons; one is the new advances in perturbative gauge theory we have just reviewed, but the other is an interesting duality discovered between color and kinematics (Bern et al. (2010c)), which results in being able to write gravity amplitudes as two copies of gauge theory amplitudes (see Bern et al. (2010a),,Bern (2002)). By writing $\mathcal{N} = 8$ supergravity as two copies of $\mathcal{N} = 4$ Yang-Mills, it has been shown that the former is actually finite up to 4 loops and possibly further (Bern et al. (2010b), Bern et al. (2011)). This remarkable result means that some version of point-like gravity might be finite after all.

Chapter 2

Black-hole on a Tense Codimension-2 Brane

In most of the available work, to localize fields on a brane authors simply do a projection onto the brane in which all angular coordinates θ_i in (1.4) are set to $\pi/2$ except for the usual 4-dimensional θ and φ, e.g. in Kanti (2004) and Kanti et al. (2006). In a Schwarzschild background, this results in a 4D Schwarzschild written using the higher dimensional metric:

$$ds^2 = -f_n(r)dt^2 + \frac{1}{f_n(r)}dr^2 + r^2 d\Omega_2^2 \tag{2.1}$$

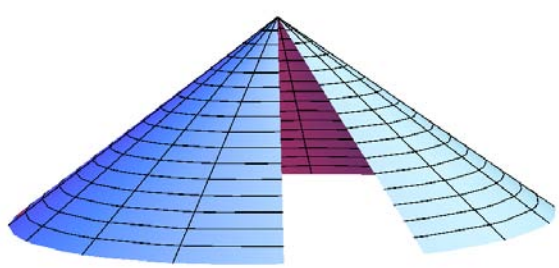

Figure 2.1: A deficit angle that forms in the presence of a conical singularity.

In using this metric to study brane-localized modes, such treatments are clearly neglecting the dynamical nature of the brane, which is represented through tension λ, and the main reason for that is the difficulty of obtaining higher-dimensional solutions of Einstein's equations in the presence of tension. One often finds this justified by the assumption that in order for a black hole to be treated semi-classically, it has to have a mass M_{BH} much bigger than the Planck scale, and this means that the tension does not perturb the black hole background and that at the scale of r_h the solution is flat. While this is in principle true, it turns out that for a black hole to be clear of the quantum regime in this context, given a gravity scale of the order of 1TeV, the mass of the black hole needs to be on the order of a just a few TeV (see Giddings and Thomas (2002). However, because brane tension will come from contributions to vacuum fluctuations coming from brane-localized fields, one expects brane tension to be of the same order as the fundamental scale of the theory, which means that in order to be realistic, tension needs to be taken into account.

Relatively recently, the first exact solution describing a Schwarzschild black hole on a tense codimension-2 3-brane was constructed by Kaloper and Kiley (2006) in 6-dimensional spacetime. The advantage of the codimension-2 setup is that the tension of the brane does not curve either the brane or the bulk, instead, a conical singularity creating a deficit angle $\Delta\varphi$ is formed, very much like what happens with a cosmic string, another codimension-2 setup. The deficit angle provides a self-tuning mechanism through the adaptation of the deficit angle to the amount of brane tension. In our 6-dimensional space the deficit angle looks like this:

$$\Delta\varphi = 2\pi(1-b)\lambda M_*^4 \tag{2.2}$$

where $0 < b \leq 1$ is a measure of the deficit angle. Clearly, after taking away the wedge that defines the deficit angle, we need to identify the edges of the cut, and this results in a restyling of the angle φ. If we go through the derivation steps followed in Kaloper and Kiley (2006), we end up with an *exact* solution that looks like Schwarzschild solution with the azimuthal angle rescaled:

$$ds_6^2 = -f(r)dt^2 + f(r)^{-1}dr^2 + r^2\left(d\theta_3^2 + \sin^2\theta_3\left(d\theta_2^2 + \sin^2\theta_2\left(d\theta_1^2 + b^2\sin^2\theta_1 d\varphi^2\right)\right)\right) \tag{2.3}$$

where the index n on f has been dropped because from now on we are only considering $n = 2$. One significant implication of using this metric is that the horizon radius r_h gets enhanced:

$$r_h = \left(\frac{\mu}{b}\right)^{1/3}, \qquad \mu = \frac{M_{\mathrm{MB}}}{4\pi^2 M_*^4} \tag{2.4}$$

More recently, another solution for a rotating black hole on a tense codimension-2 brane was found Kiley (2007). These solutions have opened up the way for much exploration of the effect of tension on already known quantities, (e.g. Dai et al. (2007), Kobayashi et al. (2008), Chen et al. (2007), Chen et al. (2008), and al Binni and Siopsis (2009)).

To study emissions from black holes, we need to rewrite the field equations describing these perturbations using the metric describing the black hole. It turns out that in doing so, we can always separate variables, so that we get a set of angular equations and a radial equation that can be written in a Schrödinger-like form for a function $\Psi(r)$ related to the radial function $R(r)$:

$$\frac{d^2\Psi\left(r_*\right)}{dr_*^2} + \left(\omega^2 - V\left[r\left(r_*\right)\right]\right)\Psi\left(r_*\right) = 0 \tag{2.5}$$

where r_* is the so-called tortoise coordinate given in terms of the metric function $f(r)$:

$$r_* = \int \frac{dr}{f(r)} \tag{2.6}$$

and $V(r)$ is an effective potential. In considering perturbations of integer spin around a Schwarzschild black hole we need to use the following potential (see Ishibashi and

Kodama (2003), Cardoso et al. (2006b) and Cardoso et al. (2006a)):

$$V_1 = f(r)\left[\frac{\eta_{D-3}}{r^2} + \frac{(D-2)(D-4)}{4r^2} + \frac{(1-p^2)\,(D-2)^2}{4}\frac{r_h^{D-3}}{r^{D-1}}\right],\ D = n+4 \tag{2.7}$$

with

$$p = \begin{cases} 0 & \text{scalar and gravitational tensor pert.} \\ 2 & \text{gravitational vector} \\ 2/(D-2) & \text{EM (gauge) vector} \\ 2(D-3)/(D-2) & \text{EM (scalar)} \end{cases} \tag{2.8}$$

and

$$\ell = \begin{cases} 0, 1, ... & \text{scalar} \\ 1, 2, ... & \text{EM} \\ 2, 3, ... & \text{gravitational} \end{cases} \tag{2.9}$$

and in which case $\Psi = r^{1+\frac{n}{2}}R$. Gravitational scalars are described by a different potential:

$$V_2 = f(r)\frac{Q(r)}{16r^2 H(r)^2} \tag{2.10}$$

where

$$\begin{aligned} Q(r) &= 6400\left(\frac{r_h}{r}\right)^9 + 1920\,(\eta_3 - 4)\left(\frac{r_h}{r}\right)^6 \\ &- 1920\,(\eta_3 - 4)\left(\frac{r_h}{r}\right)^3 + 16\,(\eta_3 - 4)^3 + 96\,(\eta_3 - 4)\,, \\ H(r) &= (\eta_3 - 4) + 10\left(\frac{r_h}{r}\right)^3 \end{aligned} \tag{2.11}$$

When we want to consider Standard Model perturbations, which are always localized on the brane, we need to use a modification of the Teukolsky (1973) Master Equation for the brane. For a Schwarzschild background it has the following form (see P. Kanti (2003) and Cvetic and Larsen (1998)):

$$\begin{aligned} &\left(fr^2\right)^s \frac{d}{dr}\left[\left(fr^2\right)^{1-s}\frac{dR_s}{dr}\right] + \left\{\frac{\omega^2 r^2}{f} + 2is\omega r\right. \\ &\left.-\frac{is\omega r}{f}(n+1)(1-f) - \Lambda - (2s-1)(s-1)(n+1)(1-f)\right\} R_s = 0 \end{aligned} \tag{2.12}$$

where

$$\Lambda = \ell(\ell+1) - s(s-1), \tag{2.13}$$

and s is spin. This equation can be recast in the Schrödinger-like form using the following potential:

$$\begin{aligned} V(r) = {} & f(r)\left(\frac{\eta_1}{r^2} + \frac{r_h^{n+1}}{r^{n+3}}\right) - \frac{2i\omega s}{r} + \frac{(3+n)is\omega r_h^{n+1}}{r^{n+2}} \\ & + \left\{(2s-1)(s-1) + \frac{1}{4}n\left[3(2s-1)^2 + 2s(n-1) + 5\right]\right\}\left[-\frac{r_h^{2(n+1)}}{r^{2(n+2)}} + \frac{r_h^{n+1}}{r^{n+3}}\right] \\ & + \frac{1}{4}s^2(n+1)^2\frac{r_h^{2(n+1)}}{r^{2(n+2)}} \end{aligned} \tag{2.14}$$

The corresponding angular equation reads:

$$\frac{1}{\sin\theta}\frac{d}{d\theta}\left(\sin\theta\frac{d\,{}_sS_\ell^m}{d\theta}\right) + \left(-\frac{2ms\cot\theta}{\sin\theta} - \frac{m^2}{\sin^2\theta} + s - s^2\cot^2\theta + \Lambda\right){}_sS_\ell^m(\theta) = 0 \tag{2.15}$$

where

$$e^{im\varphi}\,{}_sS_\ell^m(\theta) = {}_sY_\ell^m(\Omega_2) \tag{2.16}$$

are known as the spin-weighted spherical harmonics. We will be using the Teukolsky equation to consider vector bosons ($s = 1$) and massless fermions ($s = 1/2$). In all of the above we used the following definition:

$$\eta_{D-3} = \ell_D\left(\ell_D + D - 3\right) \tag{2.17}$$

In order to find Quasi-normal modes (QNMs) and study Hawking radiation using these equations in subsequent chapters, we need to have their eigenvalues ω. However, as can be seen, since the effective potentials contain the angular eigenvalues$\{\eta_{D-3}\}$, we have to first solve the combined angular eigenvalue problem, which is not trivial due to the presence of the angle deficit parameter b. In the absence of b, the equations reduce to the usual angular equations on a $D-2$ sphere. For scalar perturbations with $s = 0$ these equations for 2 extra dimensions look like this:

$$\begin{aligned}
\frac{1}{\sin^3\theta}\frac{\mathrm{d}}{\mathrm{d}\theta}\left(\sin^3\theta\frac{\mathrm{d}}{\mathrm{d}\theta}\Theta(\theta)\right)+\left(\eta_3-\frac{\eta_2}{\sin^2\theta}\right)\Theta(\theta)=0\\
\frac{1}{\sin^2\varphi}\frac{\mathrm{d}}{\mathrm{d}\varphi}\left(\sin^2\varphi\frac{\mathrm{d}}{\mathrm{d}\varphi}\Phi(\varphi)\right)+\left(\eta_2-\frac{\eta_1}{\sin^2\varphi}\right)\Phi(\varphi)=0\\
\frac{1}{\sin\chi}\frac{\mathrm{d}}{\mathrm{d}\chi}\left(\sin\chi\frac{\mathrm{d}}{\mathrm{d}\chi}\Gamma(\chi)\right)+\left(\eta_1-\frac{\eta_0}{\sin^2\chi}\right)\Gamma(\chi)=0\\
\frac{1}{b^2}\frac{\mathrm{d}^2}{\mathrm{d}\psi^2}\Xi(\psi)+\eta_0\Xi(\psi)=0
\end{aligned} \tag{2.18}$$

The η_0 is readily seen to be:

$$\eta_0 = \frac{m}{b}, \qquad m \in \mathbb{Z} \tag{2.19}$$

But the problem comes from the other ηs. The issue of finding these eigenvalues was addressed numerically by Dai et al. (2007) and analytically (perturbatively to first order in the tension $(1-b)$) by Chen et al. (2007), and what we did in al Binni and Siopsis (2007) was to arrive at analytical formulas for arbitrary tension. To start, let us consider a special case:

$$b = \frac{1}{N}, \qquad N \in \mathbb{N} \tag{2.20}$$

This set of special points includes high tension. Zero tension corresponds to the first point $(N = 1, b = 1)$ and maximum tension $(b \to 0)$ is an accumulation point of the set. By restricting attention to the set (2.20), the eigenvalue problem reduces to one solvable by regular spherical harmonics. Working our way up, we note that for $b = 1$ (regular sphere), the eigenvalue η_1 may be written as $\eta_1 = \ell_1(\ell_1 + 1)$, where ℓ_1 is an integer. We also have $\eta_0 = m \leq \ell_1$. It is easily seen that for an arbitrary b, η_1 is similarly given by:

$$\eta_1 = \lambda_1(\lambda_1 + 1), \qquad \lambda_1 = \ell_1 + (N-1)m = \ell_1 + \left(\frac{1}{b} - 1\right)m \tag{2.21}$$

Notice that $\lambda_1 \leq N\ell_1$ and so $\eta_0 = mN \leq N\ell_1$, which is the maximum value of λ_1. Going up to the next angular equation, we obtain the eigenvalue η_2 as:

$$\eta_2 = \lambda_2 \left(\lambda_2 + 2\right), \qquad \lambda_2 = \ell_2 + (N-1)m = \ell_2 + \left(\frac{1}{b} - 1\right) m \tag{2.22}$$

reducing to the standard result on a 3-sphere $\eta_2 = \ell_2 \left(\ell_2 + 2\right)$ with integer ℓ_2 when $b = 1$. And finally, carrying out the same steps for η_3 we get:

$$\eta_3 = \lambda_3 \left(\lambda_3 + 3\right), \qquad \lambda_3 = \ell_3 + (N-1)m = \ell_3 + \left(\frac{1}{b} - 1\right) m \tag{2.23}$$

Although this result was derived for integral $1/b$, it holds for arbitrary $1/b$ as well ($b \in (0, 1]$). This may be seen by first generalizing to rational values of b, which may also be done in terms of ordinary spherical harmonics and then to arbitrary b by noticing that the rational numbers form a dense subset of the interval $(0, 1]$. Alternatively, one may argue that the above expressions for the angular eigenvalues hold in general by analytic continuation. We have verified their validity numerically using the Milne-spline method (see Yano et al. (2003)) by least-square fitting the numerical results to the exact analytic expressions which resulted to a perfect fit. Figure 2.2 shows the flow of the eigenvalue η_3 with brane tension (as we vary b). It also demonstrates that our analytical expression for η_3 (2.23) reproduces the numerical results of Dai et al. (2007). Moreover, it is easily seen that (2.21-2.23) agree with the results of Chen et al. (2007) to first order in the tension $(1/b - 1)$. Turning to other types of perturbation, we note that the angular equations differ slightly from the set of scalar equations (2.17). For vector and tensor perturbations, η_3 ought to be replaced by $\eta_3 - 1$ and $\eta_3 - 2$, respectively.

More recently, Cho et al. (2008b) presented a rigorous derivation of a similar result for Dirac fermions using Jacobi polynomials.*

* Based on this, we can take things one step further by showing that by reducing (2.15) to a Jacobi equation we can arrive at the same result irrespective of spin, which therefore proves our initial result rigorously in 4 dimensions for arbitrary spin.

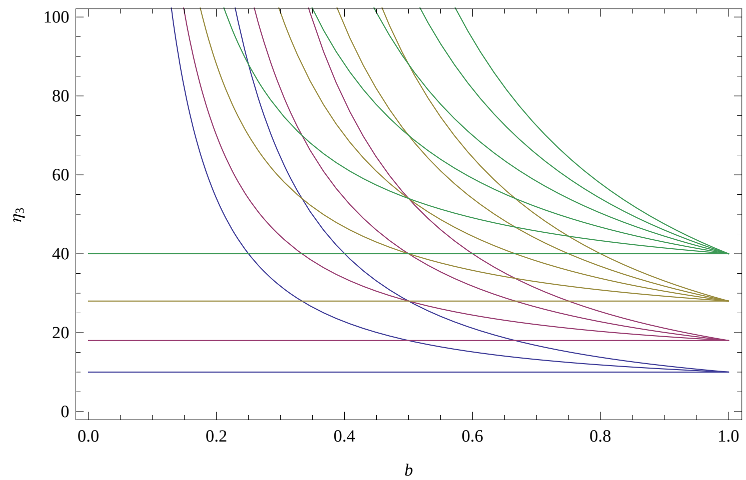

Figure 2.2: Flow of eigenvalue η_3 with the deficit angle parameter b.

In summary, we see that we can carry out calculations for Schwarzschild black holes on a tense codimension-2 three-brane in the same way we do the 6D Schwarzschild in the absence of tension, except that for well-defined modifications summarized in terms of the following rules:

$$r_h \to \frac{r_h}{\sqrt[3]{b}}, \qquad \ell_n \to \lambda_n = \ell + \left(\frac{1}{b} - 1\right) m, \qquad \varphi \to b\varphi \tag{2.24}$$

Chapter 3

Quasi-normal Frequencies of a Black-Hole on a Tense Brane

Besides Hawking radiation (Chapter 4), Quasi-normal modes (QNMs) represent two distinctive signatures of black-holes. In this chapter we will consider quasi-normal frequencies of a black-hole on a tense brane. QNMs are the damped oscillations that take place under the effect of perturbation to the black-hole background. The oscillation occurs at characteristic frequencies that are complex numbers whose imaginary parts represent the damping. QNMs have been studied extensively in the context of four-dimensional asymptotically flat spacetime (see Kokkotas and Schmidt (1999) and Nollert (1999)) for general reviews of the earlier work on the subject). When it comes to detection, neither Hawking radiation nor QNMs has been observed yet, and only indirect evidence has been used to infer the existence of astronomical black holes. Nevertheless, gravitational wave observation to be hopefully achieved by projects like LIGO should offer a chance to detect QNMs in the near future.

Aside from astronomical interest, QNMs have been gaining attention recently for several reasons. The study of QNMs can shed light on the AdS/CFT correspondence (see, e.g., Chan and Mann (1997) and Horowitz and Hubeny (2000)) and is relevant to the Barbero-Immirzi parameter (see Barbero (1995) and Immirzi (1997)) of loop quantum gravity (e.g., Rovelli and Smolin (1995), Rovelli (1998), Ashtekar and Lewandowski (1997)). In addition to these considerations, in brane-world models with large extra-dimensions gravity is much stronger than observed, and the production and evaporation of mini black holes becomes a viable possibility at the LHC Argyres et al. (1998); Banks and Fischler (1999); Emparan et al. (2000); Dimopoulos and Landsberg (2001); Giddings and Thomas (2002) (see Landsberg (2006) for a recent review). QNMs may then be observed at the LHC via the detection of the decay products of these mini black holes which will include Standard Model particles Berti et al. (2003); Kanti (2004); Kanti and Konoplya (2006); Kanti et al. (2006); Abdalla et al. (2006).

In a brane-world model the inclusion of tension affects potential observations depending on the amount of tension, and it is therefore advantageous to study the effect of tension on QNMs. The numerical study conducted by Dai et al. (2007) showed that as the black hole evaporates, the power emitted in the bulk decreases as the brane tension increases, which is a favorable state from the observational point of view.

That result shows that for high tension the semi-classical approximation becomes more reliable. Analytical results concerning the quasi-normal modes of scalar perturbations were derived in Chen et al. (2007) to first order in the brane tension. What we will do now is employ the results of the previous chapter to probe the full range of tension.

Having obtained an exact analytical expression for η_3 in (2.23) valid for an arbitrary brane tension ($0 < b \leq 1$), we may solve the radial equation (2.5) with the effective potentials (2.7) and (2.8) for the various perturbations to find the corresponding quasi-normal modes. In Chen et al. (2007) the third-order WKB approximation was used to obtain the quasi-normal modes of scalar perturbations. We will extend their results here by including scalar, electromagnetic and gravitational perturbations and deriving expressions that are valid for arbitrary brane tension.

3.1 WKB Approximation of Frequencies

The third-order WKB formulas suitable for calculating black hole quasi-normal modes were worked out by Iyer and Will (1987). The frequencies are given by

$$\omega_n^2 = \left[V_0 + (-2V_0'')^{1/2}\Lambda\right] - i\alpha(-2V_0'')^{1/2}(1+\Omega) \tag{3.1a}$$

where

$$\Lambda = \frac{1}{(-2V_0'')^{1/2}}\left\{\frac{1}{8}\left(\frac{V_0^{(4)}}{V_0''}\right)\left(\frac{1}{4}+\alpha\right) - \frac{1}{288}\left(\frac{V_0'''}{V_0''}\right)^2(7+60\alpha^2)\right\} \tag{3.1b}$$

$$\begin{aligned}\Omega = \frac{1}{(-2V_0'')^{1/2}}&\left\{\frac{5}{6912}\left(\frac{V_0^{(4)}}{V_0''}\right)(77+188\alpha^2) - \left(\frac{V'''^2_0 V_0^{(4)}}{V''^3_0}\right)\frac{51+100\alpha^2}{384}\right.\\ &\left. + \left(\frac{V_0^{(4)}}{V_0''}\right)^2\frac{67+68\alpha^2}{2304} + \left(\frac{V_0'''V_0^{(5)}}{V''^2_0}\right)\frac{19+28\alpha^2}{288} - \left(\frac{V_0^{(6)}}{V_0''}\right)\frac{5+4\alpha^2}{288}\right\}\end{aligned} \tag{3.1c}$$

and

$$\alpha = n + \frac{1}{2}, \qquad V_0^{(s)} = \left.\frac{d^sV}{dr_*^s}\right|_{r_*=r_*(r_p)} \tag{3.1d}$$

with r_p being the peak of the potential. Sample numerical results using the above formulas for the various types of perturbation (defined through the effective potentials V_1 (2.7) and V_2 (2.10)) are shown in Tables 3.1 and 3.2.

We may also obtain explicit analytic expressions for the frequencies by expanding in inverse powers of the angular momentum quantum number ℓ_3. We obtain

$$\omega_n = \omega_n^{(0)} + \omega_n^{(1)}\,\frac{1}{\ell_3} + \mathcal{O}(1/\ell_3^2) \tag{3.2}$$

where the leading contribution is given by

$$\omega_n^{(0)} = \frac{\sqrt{3}}{2^{2/3}5^{5/6}r_h}\,\left[2\lambda_3 + 3 - i\sqrt{3}(2n+1)\right] \tag{3.3}$$

Table 3.1: 3rd-order WKB approximation of the fundamental frequency. First four columns correspond to the potential V_1 (2.7); last column is for V_2 (2.10). $\mu = 2$ and $\ell_3 = 5$.

b	$p = 0$	$p = \frac{1}{2}$	$p = \frac{3}{2}$
		$m = 0$	
1.0	$2.94965 - 0.394141i$	$2.9356 - 0.392963i$	$2.82469 - 0.38449i$
0.9	$2.84786 - 0.380539i$	$2.83429 - 0.379402i$	$2.72721 - 0.371221i$
0.7	$2.61901 - 0.349959i$	$2.60653 - 0.348913i$	$2.50805 - 0.34139i$
0.5	$2.34114 - 0.31283i$	$2.32999 - 0.311895i$	$2.24196 - 0.30517i$
0.3	$1.97459 - 0.263851i$	$1.96519 - 0.263062i$	$1.89094 - 0.25739i$
0.1	$1.36911 - 0.182944i$	$1.36259 - 0.182397i$	$1.3111 - 0.178464i$
0.01	$0.635483 - 0.084915i$	$0.632456 - 0.0846613i$	$0.608561 - 0.0828358i$
0.001	$0.294965 - 0.0394141i$	$0.29356 - 0.0392963i$	$0.282469 - 0.038449i$
		$m = 5$	
1.0	$2.94965 - 0.394141i$	$2.9356 - 0.392963i$	$2.82469 - 0.38449i$
0.9	$3.09052 - 0.380255i$	$3.07804 - 0.379296i$	$2.9793 - 0.372292i$
0.7	$3.47992 - 0.34922i$	$3.47056 - 0.34864i$	$3.39632 - 0.344283i$
0.5	$4.1372 - 0.311811i$	$4.13093 - 0.311522i$	$4.08098 - 0.309295i$
0.3	$5.51032 - 0.262764i$	$5.50697 - 0.262668i$	$5.48028 - 0.261908i$
0.1	$10.8286 - 0.182101i$	$10.8278 - 0.182093i$	$10.8213 - 0.182027i$
0.01	$48.9429 - 0.0845181i$	$48.9429 - 0.0845181i$	$48.9426 - 0.0845178i$
0.001	$226.561 - 0.0392298i$	$226.561 - 0.0392298i$	$226.561 - 0.0392298i$

b	$p = 2$	V_2
	$m = 0$	
1.0	$2.73082 - 0.37905i$	$2.60248 - 0.362449i$
0.9	$2.63657 - 0.365969i$	$2.51267 - 0.349941i$
0.7	$2.4247 - 0.33656i$	$2.31076 - 0.32182i$
0.5	$2.16745 - 0.300852i$	$2.06559 - 0.287676i$
0.3	$1.8281 - 0.253749i$	$1.74219 - 0.242635i$
0.1	$1.26753 - 0.175939i$	$1.20797 - 0.168234i$
0.01	$0.588336 - 0.0816639i$	$0.560688 - 0.0780873i$
0.001	$0.273082 - 0.037905i$	$0.260248 - 0.0362449i$
	$m = 5$	
1.0	$2.73082 - 0.37905i$	$2.60248 - 0.362449i$
0.9	$2.89524 - 0.367484i$	$2.7834 - 0.354961i$
0.7	$3.33248 - 0.340972i$	$3.25169 - 0.334445i$
0.5	$4.0377 - 0.307481i$	$3.98527 - 0.304652i$
0.3	$5.45701 - 0.261261i$	$5.42979 - 0.260422i$
0.1	$10.8156 - 0.18197i$	$10.809 - 0.181903i$
0.01	$48.9423 - 0.0845175i$	$48.942 - 0.0845172i$
0.001	$226.561 - 0.0392298i$	$226.561 - 0.0392298i$

Table 3.2: 3rd-order WKB approximation of the first harmonic. First four columns correspond to the potential V_1 (2.7); last column is for V_2 (2.10). $\mu = 2$ and $\ell_3 = 5$.

b	$p = 0$	$p = \frac{1}{2}$	$p = \frac{3}{2}$
		$m = 0$	
1.0	$2.85074 - 1.1942i$	$2.83667 - 1.19065i$	$2.72427 - 1.16507i$
0.9	$2.75236 - 1.15298i$	$2.73878 - 1.14956i$	$2.63025 - 1.12486i$
0.7	$2.53118 - 1.06033i$	$2.51869 - 1.05718i$	$2.41889 - 1.03447i$
0.5	$2.26263 - 0.947833i$	$2.25147 - 0.945018i$	$2.16225 - 0.924716i$
0.3	$1.90838 - 0.799434i$	$1.89896 - 0.797059i$	$1.82372 - 0.779935i$
0.1	$1.32319 - 0.554296i$	$1.31667 - 0.55265i$	$1.26449 - 0.540777i$
0.01	$0.614173 - 0.257282i$	$0.611143 - 0.256517i$	$0.586926 - 0.251006i$
0.001	$0.285074 - 0.11942i$	$0.283667 - 0.119065i$	$0.272427 - 0.116507i$
		$m = 5$	
1.0	$2.85074 - 1.1942i$	$2.83667 - 1.19065i$	$2.72427 - 1.16507i$
0.9	$3.00273 - 1.1503i$	$2.99022 - 1.14741i$	$2.8904 - 1.12629i$
0.7	$3.41427 - 1.05338i$	$3.40488 - 1.05163i$	$3.33014 - 1.03851i$
0.5	$4.09324 - 0.938259i$	$4.08695 - 0.937391i$	$4.03683 - 0.930697i$
0.3	$5.48691 - 0.789232i$	$5.48356 - 0.788943i$	$5.45683 - 0.786663i$
0.1	$10.8229 - 0.546384i$	$10.8221 - 0.546359i$	$10.8156 - 0.546161i$
0.01	$48.9427 - 0.253555i$	$48.9426 - 0.253555i$	$48.9423 - 0.253554i$
0.001	$226.561 - 0.117689i$	$226.561 - 0.117689i$	$226.561 - 0.117689i$

b	$p = 2$	V_2
	$m = 0$	
1.0	$2.62697 - 1.14859i$	$2.50456 - 1.09858i$
0.9	$2.53632 - 1.10895i$	$2.41813 - 1.06067i$
0.7	$2.3325 - 1.01984i$	$2.22381 - 0.975436i$
0.5	$2.08503 - 0.911635i$	$1.98787 - 0.871946i$
0.3	$1.75858 - 0.768902i$	$1.67663 - 0.735427i$
0.1	$1.21933 - 0.533127i$	$1.16251 - 0.509917i$
0.01	$0.565964 - 0.247456i$	$0.539591 - 0.236682i$
0.001	$0.262697 - 0.114859i$	$0.250456 - 0.109858i$
	$m = 5$	
1.0	$2.62697 - 1.14859i$	$2.50456 - 1.09858i$
0.9	$2.804 - 1.11174i$	$2.69594 - 1.07411i$
0.7	$3.26539 - 1.02852i$	$3.18572 - 1.00894i$
0.5	$3.99329 - 0.92524i$	$3.94102 - 0.91675i$
0.3	$5.43352 - 0.78472i$	$5.40629 - 0.7822i$
0.1	$10.8098 - 0.545989i$	$10.8033 - 0.545789i$
0.01	$48.942 - 0.253553i$	$48.9417 - 0.253552i$
0.001	$226.561 - 0.117689i$	$226.561 - 0.117689i$

in terms of the radius of the horizon (2.4) and the angular quantum number λ_3 (2.23). It is independent of the type of perturbation and reduces to the zero tension result (Schwarzschild black hole):

$$\omega_n \approx \frac{1}{2r_h}\left(\frac{2}{D-1}\right)^{\frac{1}{D-3}}\sqrt{\frac{D-3}{D-1}}\left[2\ell_3 + D - 3 - i\sqrt{D-3}\,(2n+1)\right] \tag{3.4}$$

for $D = 6$. The first-order correction in (3.2) is given by

$$\omega_n^{(1)} = \frac{1}{\sqrt{3}\;2^{5/3}5^{11/6}r_h}\;\left[5 - 42(n+n^2) - 48p^2\right] \tag{3.5}$$

for perturbations governed by the effective potential $V_1(r)$ (eq. (2.7)), and by

$$\omega_n^{(1)} = \frac{\sqrt{3}}{2^{2/3}5^{5/6}r_h}\;\left[-\frac{15}{2} + 3(n+n^2)\right] \tag{3.6}$$

for scalar gravitational perturbations governed by $V_2(r)$ (eq. (2.10)). It should be pointed out that the first-order WKB estimate of Chen et al. (2007)

$$\omega^2 = V_0 - i\alpha(-2V_0'')^{1/2} \tag{3.7}$$

suffices for the derivation of the above analytical asymptotic expressions. For the purpose of comparison with the results in Chen et al. (2007), we look at scalar perturbations by setting $p = 0$, $n = 0$, $\ell_3 = 5$ and $\mu = 2$ letting m take the values 1 and 5 (for $m = 0$ or $b = 1$ the two approaches agree, because the angular eigenvalue η_3 (2.23) agrees with its value on a regular sphere). This is shown in Table 3.3 where we see that while the two cases agree perfectly on the imaginary part of the frequencies for any tension, the real part is over-estimated in the perturbative calculation of Chen et al. (2007) at high tension (small b). Figures 3.1 and 3.2 show the real and imaginary parts of the frequency as a function of b, respectively, for the chosen set of parameters. The agreement on the imaginary parts can be traced to the asymptotic expression (3.2) which is valid for large ℓ_3. Unlike the real part, the imaginary

Table 3.3: A comparison of fundamental quasi-normal frequencies using *(a)* the exact expression (2.23) for η_3 and *(b)* first-order approximate eigenvalues calculated in Chen et al. (2007). We set $\ell_3 = 5$, $\mu = 2$.

b	*(a)*	*(b)*
	$m = 1$	
0.9	$2.89639 - 0.380476i$	$2.89863 - 0.380473i$
0.7	$2.79116 - 0.349752i$	$2.8203 - 0.349721i$
0.5	$2.70024 - 0.312448i$	$2.82885 - 0.312347$
0.3	$2.68138 - 0.263264i$	$3.15335 - 0.263078i$
0.1	$3.26011 - 0.182229i$	$5.50665 - 0.182137i$
0.01	$10.2961 - 0.0845195i$	$24.8883 - 0.0845183i$
	$m = 5$	
0.9	$3.09052 - 0.380255i$	$3.09339 - 0.380252i$
0.7	$3.47992 - 0.34922i$	$3.51179 - 0.349203i$
0.5	$4.1372 - 0.311811i$	$4.25276 - 0.311786i$
0.3	$5.51032 - 0.262764i$	$5.84111 - 0.262748i$
0.1	$10.8286 - 0.182101i$	$12.0048 - 0.182099i$
0.01	$48.9429 - 0.0845181i$	$55.6375 - 0.0845181i$

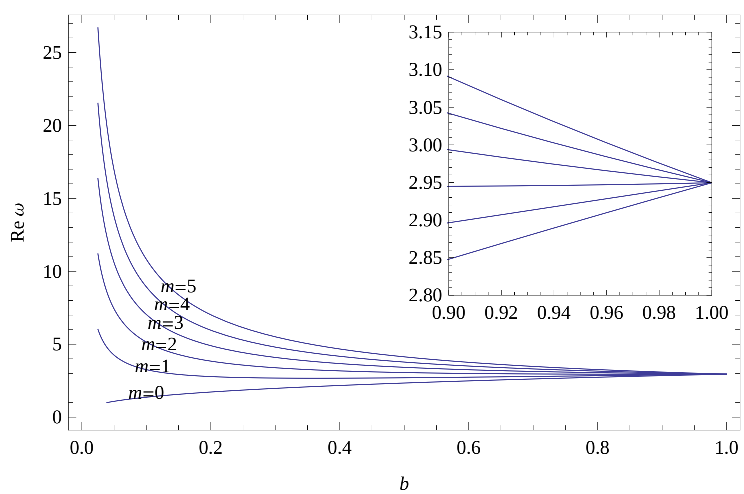

Figure 3.1: The real part of the fundamental frequency as a function of the tension b for scalar perturbations with $\mu = 2$, $\ell_3 = 5$ and $m = 0, \ldots, 5$ (bottom to top). Detail showing degeneracy at zero tension ($b = 1$).

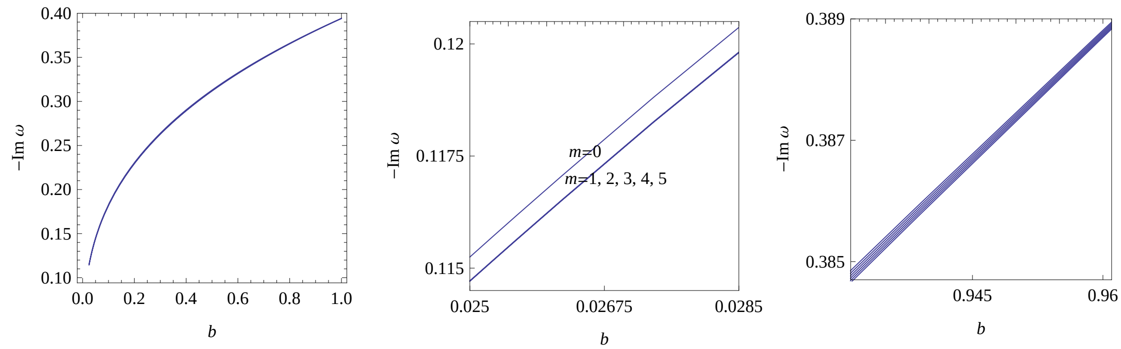

Figure 3.2: The imaginary part of the fundamental frequency for scalar perturbations with $\mu = 2$ and $\ell_3 = 5$ and $M = 2$. Detail showing splitting with m at high ($b \to 0$) and low ($b \to 1$) tension.

part does not vary with tension except through the value of the radius of the horizon $\Im\omega \sim 1/r_h \sim b^{1/3}$ (eq. (2.4)). This also shows that the imaginary part of the frequency (damping) vanishes at high tension ($b \to 0$).

The real part, which represents the actual frequency of oscillation, also goes to zero at high tension ($\Re\omega \sim b^{1/3}$ as $b \to 0$) for $m = 0$. For all other values of the magnetic quantum number ($m \neq 0$), the real part diverges as $\Re\omega \sim b^{-2/3}$. This level splitting is reminiscent of the Zeeman effect for an atom in a strong magnetic field and is attributed to the spatial symmetry of the states.

At the other end of the spectrum (vasnishing tension, $b \to 1$), frequencies become degenerate, as expected, because spherical symmetry is restored in the absence of a brane (Schwarzschild solution).

Figure 3.3 shows the dependence of the fundamental frequency on the type of perturbation. The graphs are in agreement with the analytic result (3.2), which shows that the dependence on the type of perturbation is a next-to-leading-order effect (expanding in inverse powers of the angular momentum quantum number). Similar results hold for higher harmonics as well. In figure 3.4, in addition to the type of perturbation, the magnetic quantum number m is also allowed to vary. For the potential V_1 (2.7), the real part decreases as the parameter p labeling the type of perturbation decreases and the real part of the frequency for V_2 (2.10) is lower than

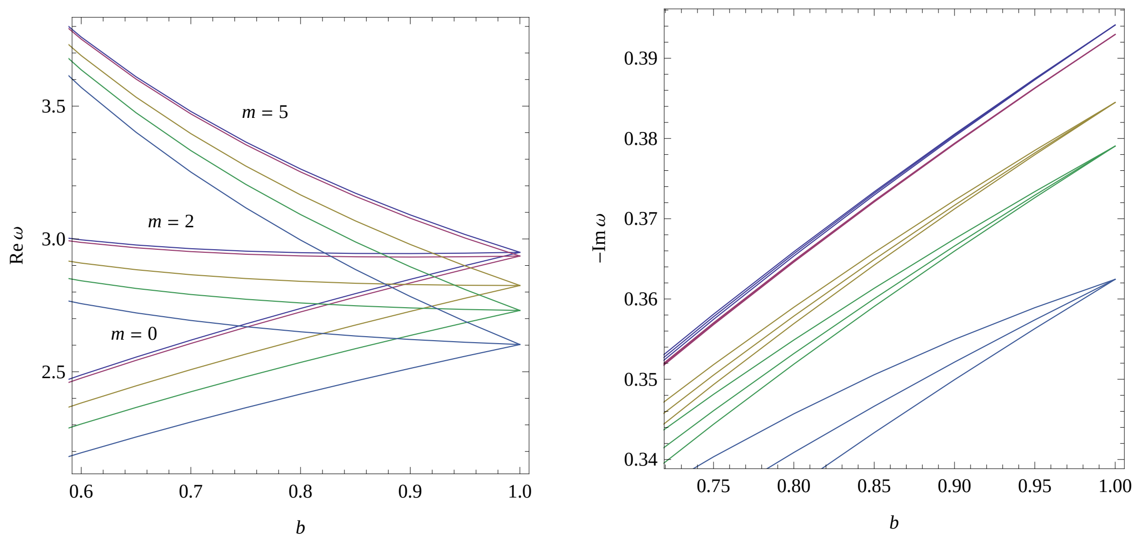

Figure 3.3: Real and imaginary parts of the fundamental frequency as a function of the tension b for different perturbations with $\mu = 2$, $\ell_3 = 5$, $m = 0, 2, 5$. Top to bottom: $p = 0, \frac{1}{2}, \frac{3}{2}, 2$ (2.7) and scalar gravitational (2.10).

the rest. The (negative) imaginary part of the frequency exhibits a similar behavior, except that now we see more change in the general shape depending on the type of perturbation.

The numerical accuracy of the analytic expression for quasi-normal frequencies (eqs. (3.2), (3.3) and (3.4)) is explored in Tables 3.4 and 3.5. Evidently, the agreement is fairly good throughout the range of b, for both high and low brane tension. The agreement becomes better as the angular momentum quantum number ℓ_3 increases, as expected. The tables only show results for the fundamental frequency, however similar agreement is obtained for higher harmonics.

3.2 Summary and Discussion

We analyzed the effect of brane tension on the low-lying quasi-normal modes of a black hole localized on a tense 3-brane in six flat dimensions Kaloper and Kiley (2006). In the presence of the brane, the symmetry is no longer spherical, resulting in angular wave equations for which an analytic solution is not available. The properties

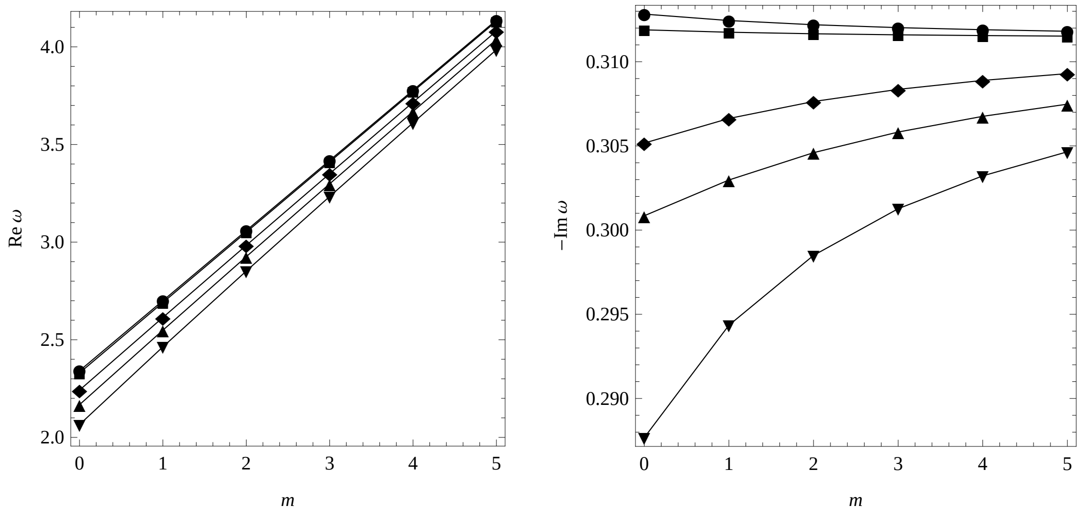

Figure 3.4: Dependence of the fundamental frequency on m for $b = 0.5$ and $\ell_3 = 5$. p (2.7) increases from top to bottom; scalar gravitational (2.10) is represented by inverted triangles.

Table 3.4: Comparison between the $\mathcal{O}(1/\ell_3^2)$ analytic expression (3.2) and the WKB approximation of fundamental quasi-normal frequencies for the potential V_1 (2.7).

b	analytic	1st-order WKB	3rd-order WKB
		$\ell_3 = 5,\ m = 0,\ p = \frac{1}{2}$	
1.0	$2.93385 - 0.392298i$	$3.00359 - 0.392395i$	$2.9356 - 0.392963i$
0.9	$2.8326 - 0.37876i$	$2.89994 - 0.378853i$	$2.83429 - 0.379402i$
0.7	$2.60497 - 0.348323i$	$2.6669 - 0.348409i$	$2.60653 - 0.348913i$
0.5	$2.32859 - 0.311367i$	$2.38395 - 0.311444i$	$2.32999 - 0.311895i$
0.3	$1.96401 - 0.262617i$	$2.01071 - 0.262682i$	$1.96519 - 0.263062i$
0.1	$1.36177 - 0.182089i$	$1.39415 - 0.182133i$	$1.36259 - 0.182397i$
0.01	$0.632078 - 0.0845181i$	$0.647105 - 0.0845389i$	$0.632456 - 0.0846613i$
0.001	$0.293385 - 0.0392298i$	$0.300359 - 0.0392395i$	$0.29356 - 0.0392963i$
		$\ell_3 = 10,\ m = 5,\ p = \frac{3}{2}$	
1.0	$5.13159 - 0.392298i$	$5.17978 - 0.389449i$	$5.14172 - 0.389687i$
0.9	$5.19747 - 0.37876i$	$5.24531 - 0.376253i$	$5.21026 - 0.376461i$
0.7	$5.41823 - 0.348323i$	$5.46515 - 0.346517i$	$5.43666 - 0.346666i$
0.5	$5.87062 - 0.311367i$	$5.91599 - 0.31026i$	$5.89493 - 0.31035i$
0.3	$6.9731 - 0.262617i$	$7.01534 - 0.262142i$	$7.00269 - 0.26218i$
0.1	$11.8435 - 0.182089i$	$11.8768 - 0.182033i$	$11.8732 - 0.182038i$
0.01	$49.4141 - 0.0845181i$	$49.4307 - 0.0845178i$	$49.4306 - 0.0845178i$
0.001	$226.78 - 0.0392298i$	$226.788 - 0.0392298i$	$226.788 - 0.0392298i$

Table 3.5: Comparison between the $\mathcal{O}(1/\ell_3^2)$ analytic expression (3.2) and the WKB approximation of fundamental quasi-normal frequencies for the potential V_2 (2.10).

b	analytic	1st-order WKB	3rd-order WKB
		$\ell_3 = 10,\, m = 0$	
1.0	$5.03948 - 0.392298i$	$5.05884 - 0.383546i$	$5.02112 - 0.383837i$
0.9	$4.86556 - 0.37876i$	$4.88426 - 0.370309i$	$4.84784 - 0.370591i$
0.7	$4.47457 - 0.348323i$	$4.49176 - 0.340552i$	$4.45828 - 0.34081i$
0.5	$3.99984 - 0.311367i$	$4.0152 - 0.304421i$	$3.98527 - 0.304652i$
0.3	$3.37359 - 0.262617i$	$3.38655 - 0.256758i$	$3.36131 - 0.256953i$
0.1	$2.33912 - 0.182089i$	$2.34811 - 0.178026i$	$2.3306 - 0.178161i$
0.01	$1.08572 - 0.0845181i$	$1.08989 - 0.0826325i$	$1.08177 - 0.0826952i$
0.001	$0.503948 - 0.0392298i$	$0.505884 - 0.0383546i$	$0.502112 - 0.0383837i$
		$\ell_3 = 10,\, m = 5$	
1.0	$5.03948 - 0.392298i$	$5.05884 - 0.383546i$	$5.02112 - 0.383837i$
0.9	$5.10854 - 0.37876i$	$5.13417 - 0.371112i$	$5.09939 - 0.371363i$
0.7	$5.33645 - 0.348323i$	$5.37525 - 0.342898i$	$5.34693 - 0.34307i$
0.5	$5.79752 - 0.311367i$	$5.84989 - 0.308097i$	$5.82891 - 0.308197i$
0.3	$6.91144 - 0.262617i$	$6.97585 - 0.261239i$	$6.96322 - 0.261279i$
0.1	$11.8007 - 0.182089i$	$11.8656 - 0.18193i$	$11.862 - 0.181934i$
0.01	$49.3943 - 0.0845181i$	$49.4302 - 0.0845172i$	$49.43 - 0.0845172i$
0.001	$226.771 - 0.0392298i$	$226.788 - 0.0392298i$	$226.788 - 0.0392298i$

of the black hole as the brane tension varies were studied numerically by Dai et al. (2007) as well as analytically to first order in the tension by Chen et al. (2007). We presented an analytic solution to the angular eigenvalue problem for arbitrary tension (parametrized by $b \in (0, 1]$ which is related to the deficit angle which appears in the presence of the brane). This enabled us to obtain explicit analytic expressions for quasi-normal modes of various types of perturbation. We compared the analytic expressions to numerical results using 3rd-order WKB approximation and found good agreement. We discussed the effect of brane tension on the frequencies. For low tension ($b \to 1$), we recovered the results of spherical geometry (Schwarzschild black hole).

For high tension ($b \to 0$), the imaginary part of all frequencies (damping) was seen to vanish as $b^{1/3}$ (being inversely proportional to the radius of the horizon). The real part (representing the actual oscillation) also vanished for $m = 0$ but diverged as $b^{-2/3}$ for $m \neq 0$, similarly to the Zeeman effect for an atom in a strong magnetic field.

Chapter 4

Hawking Radiation from a Black-Hole on a Tense Brane

Hawking radiation is one of the key signatures to look for when searching for black holes. It has a unique status in that it exists on the borders between classical gravitation and quantum theory. Hawking (1975) predicted that a black hole would emit radiation due to quantum effects, but due to the smallness of the effect, it has never ever been observed for astronomical black-holes candidates. The possibility of producing mini black-holes at the LHC offers the prospect of studying the effect experimentally for the first time.

Ideally, Hawking radiation is supposed to be a perfect black-body radiation, but for an observer at infinity the radiation appears modified. This is because in escaping from the black hole the radiation needs to cross the non-trivial potential around the black hole which implies that part of the radiation will backscatter, resulting in a frequency-dependent factor that modifies the otherwise ideal black body radiation. This is known as a grey-body radiation and has a spectrum described by a modified black-body emission rate, which in $D = 4 + n$ dimensions is of the form

$$\frac{\mathrm{d}E(\omega)}{\mathrm{d}t} = \sum_{\ell,\kappa} \sigma_{\ell,\kappa}(\omega) \frac{\omega}{e^{\omega/T_{\mathrm{H}}} \mp 1} \frac{\mathrm{d}^{n+3}k}{(2\pi)^{n+3}} \tag{4.1}$$

where ℓ stands for the angular momentum quantum number, and κ for any other quantum numbers of the emitted particles. $\sigma_{\ell,\kappa}(\omega)$ is the grey-body factor modifying the black-body radiation at the horizon to the spectrum observed at asymptotic infinity away from the black hole. As mentioned in chapter 2, Hawking temperature T_{H} for a Schwarzschild black-hole is enhanced in the presence of extra-dimensions, which is a relevant factor as far as the possibility of observation goes. Experimental observation of Hawking radiation is a very exciting prospect as it constitutes direct observational evidence of black-holes, but it also should provide a rich source of information about the dimensionality and structure of spacetime as well as constituting a first step toward establishing quantum gravity as a discipline accessible to experimental investigation.

In this chapter we explore the effects of including brane tension on observational quantities related to Hawking radiation, where we obtain analytical expressions for low-frequency grey-body factors for bulk as well as brane-localized emissions, and and then compare with exact numerical results. We then calculate analytically grey-body factors in the case of large imaginary frequencies, again for emissions both in the bulk and on the brane. In the tensionless limit, our expressions are valid for arbitrary number of extra dimensions.

4.1 Low-frequency grey-body factors

Calculations of grey-body in the case of low-frequency have been already been performed both for bulk by Kanti and March-Russell (2002); Creek et al. (2006), and Cardoso et al. (2006b) and brane-localized emissions by P. Kanti (2003); Ida et al. (2003, 2005). In this section we shall extend these results to include brane tension.

In general, one tries to find an approximate solution of the radial equation which is valid at infinity and another one valid near the horizon. Then by matching the two solutions in the common domain of validity one can extract the coefficients of reflection and transmission and hence deduce the absorption coefficient (grey-body factor) as a function of frequency.

For bulk emissions of integer spin, we can use the Ishibashi-Kodama 'master equation' (see Ishibashi and Kodama (2003); Cardoso et al. (2006b)), in which the potential in $D = n + 4$ dimensions is given in eq. (2.7).

Gravitational scalar fields are governed by the more complicated potential of (2.10), but, as found by Cardoso et al. (2006b), they can be described approximately by (2.7) when p is taken to be:

$$p_{\text{grav-scalar}} \sim 2 + 0.674 D^{-0.5445} \tag{4.2}$$

Specifically, for the case we are interested in, $n = 2$, we have

$$p_{\text{grav-scalar}} = 2.25 \tag{4.3}$$

Writing the radial equation in terms of $R(r) = r^{-1-\frac{n}{2}}\Psi(r_*)$ for $n = 2$, we end up with

$$\frac{f}{r^4}\frac{\mathrm{d}}{\mathrm{d}r}\left[r^4 f R'(r)\right] + \left[\omega^2 - f\left(\frac{\lambda_3(3+\lambda_3)}{r^2} - 4p^2\frac{1}{r^5}r_h^3\right)\right]R(r) = 0 \tag{4.4}$$

where we have replaced ℓ by λ_3 (eq. (2.24)) in order to account for the brane tension. Near the horizon, it is convenient to make the change of variables $r \to f(r)$ (note that $f(r) \to 0$ as $r \to r_h$). The resulting equation is

$$(1-f)\left(f\frac{\mathrm{d}^2}{\mathrm{d}f^2}R_{NH} + \frac{\mathrm{d}}{\mathrm{d}f}R_{NH}\right) + \left(\frac{(\omega r_h)^2}{9f(1-f)} - \frac{\lambda_3(3+\lambda_3)}{9(1-f)} + \frac{4}{9}p^2\right)R_{NH} = 0 \tag{4.5}$$

whose general solution can be written in terms of hypergeometric functions,

$$R_{\mathrm{NH}}(f) = A_- f^{\alpha}(1-f)^{\beta}F(a,b,c;f) + A_+ f^{-\alpha}(1-f)^{\beta}F(a-c+1, b-c+1, 2-c; f) \tag{4.6}$$

where

$$
\begin{aligned}
&\alpha = \frac{i\omega r_h}{3}, \quad \beta = \frac{1}{2} - \frac{1}{3}\sqrt{\left(\lambda_3 + \frac{3}{2}\right)^2 - (\omega r_h)^2}, \\
&a = \alpha + \beta - \frac{2}{3}p = -\frac{i\omega r_h}{3} + \frac{1}{2} - \frac{1}{3}\sqrt{\left(\lambda_3 + \frac{3}{2}\right)^2 - (\omega r_h)^2} - \frac{2}{3}p, \\
&b = \alpha + \beta + \frac{2}{3}p = -\frac{i\omega r_h}{3} + \frac{1}{2} - \frac{1}{3}\sqrt{\left(\lambda_3 + \frac{3}{2}\right)^2 - (\omega r_h)^2} + \frac{2}{3}p, \\
&c = 1 + 2\alpha = 1 + \frac{2}{3}i\omega r_h
\end{aligned}
\tag{4.7}
$$

Imposing the boundary condition that at the horizon the solution be purely in-going, we obtain the constraint

$$A_+ = 0 \tag{4.8}$$

Far from the horizon ($f \to 1$), the asymptotic solution (4.6) under the constraint (4.8) behaves as

$$
\begin{aligned}
R_{\mathrm{NH}}(f) \sim A_- \Bigg[&\left(\frac{r_h}{r}\right)^{3\beta} \frac{\Gamma(1+2\alpha)\Gamma(1-2\beta)}{\Gamma\left(1+\alpha-\beta+\frac{2}{3}p\right)\Gamma\left(1+\alpha-\beta-\frac{2}{3}p\right)} \\
&+ \left(\frac{r_h}{r}\right)^{3(1-\beta)} \frac{\Gamma(1+2\alpha)\Gamma(2\beta-1)}{\Gamma\left(\alpha+\beta-\frac{2}{3}p\right)\Gamma\left(\alpha+\beta+\frac{2}{3}p\right)} \Bigg]
\end{aligned}
\tag{4.9}
$$

which follows from standard identities of hypergeometric functions.

In the far field region, as $r \to \infty$, or correspondingly $f \to 1$, the radial wave equation may be approximated by

$$g''(r) + \frac{1}{r}g'(r) + \left[\omega^2 - \left(\frac{9}{4} + \lambda_3(\lambda_3+3)\right)\frac{1}{r^2}\right] g(r) = 0 \tag{4.10}$$

where we defined $g(r) = r^{3/2}R(r)$. The solution can be written in terms of Bessel functions,

$$R_{\mathrm{FF}}(r) = \frac{g(r)}{r^{3/2}} = \frac{1}{r^{3/2}}\left(B_+ J_{\lambda_3+3/2}(\omega r) + B_- Y_{\lambda_3+3/2}(\omega r)\right) \tag{4.11}$$

In the low frequency regime,

$$\omega r_h \ll 1 \tag{4.12}$$

the asymptotic solution (4.11) may be approximated near the horizon by

$$R_{\rm FF}(r) \sim B_+ \frac{\left(\frac{\omega}{2}\right)^{\lambda_3+3/2}}{\Gamma\left(\lambda_3+5/2\right)} r^{\lambda_3} - B_- \frac{\Gamma\left(\lambda_3+3/2\right)}{\pi}\left(\frac{\omega}{2}\right)^{-\lambda_3-3/2} r^{-\lambda_3-3} \tag{4.13}$$

Matching the two asymptotic solutions in the intermediate region ((4.9) and (4.13), respectively), we obtain

$$\frac{B_+}{B_-} = -\frac{\Gamma(1-2\beta)\Gamma\left(\alpha+\beta-\frac{2}{3}p\right)\Gamma\left(\alpha+\beta+\frac{2}{3}p\right)\Gamma\left(\lambda_3+5/2\right)\Gamma\left(\lambda_3+3/2\right)}{\pi\Gamma\left(1+\alpha-\beta+\frac{2}{3}p\right)\Gamma\left(1+\alpha-\beta-\frac{2}{3}p\right)\Gamma(2\beta-1)}\left(\frac{2}{\omega r_h}\right)^{2\lambda_3+3} \tag{4.14}$$

where we used $\beta \approx -\lambda_3/3$ (eq. (4.7)), on account of (4.12).

The reflection coefficient is

$$\mathcal{R} = \frac{\text{outgoing amplitude}}{\text{incoming amplitude}} = \frac{B_+ - iB_-}{B_+ + iB_-} \tag{4.15}$$

from which we deduce the bulk absorption probability

$$\left|\mathcal{A}_p^{\rm bulk}\right|^2 = 1 - |\mathcal{R}|^2 = \frac{2i\left(B^* - B\right)}{BB^* + i\left(B^* - B\right) + 1} \quad , \quad B = \frac{B_+}{B_-} \tag{4.16}$$

After some algebraic manipulations, in the low frequency regime (4.12) we arrive at the explicit expression for the absorption probability,

$$\left|\mathcal{A}_p^{\rm bulk}\right|^2 = 4\pi\left(\frac{\omega r_h}{2}\right)^{4+2\lambda_3}\left[\frac{\Gamma\left(1+\frac{\lambda_3+2p}{3}\right)\Gamma\left(1+\frac{\lambda_3-2p}{3}\right)}{\Gamma\left(1+\frac{2\lambda_3}{3}\right)\Gamma\left(\lambda_3+\frac{5}{2}\right)}\right]^2 \tag{4.17}$$

which reduces to the tensionless result in the limit $b \to 1$ (see, e.g., Kanti and March-Russell (2002); Creek et al. (2006); Cardoso et al. (2006a)).

Evidently, the dependence of the absorption probability on the brane tension is complicated. To study its behavior, let us first look at some graphical representations

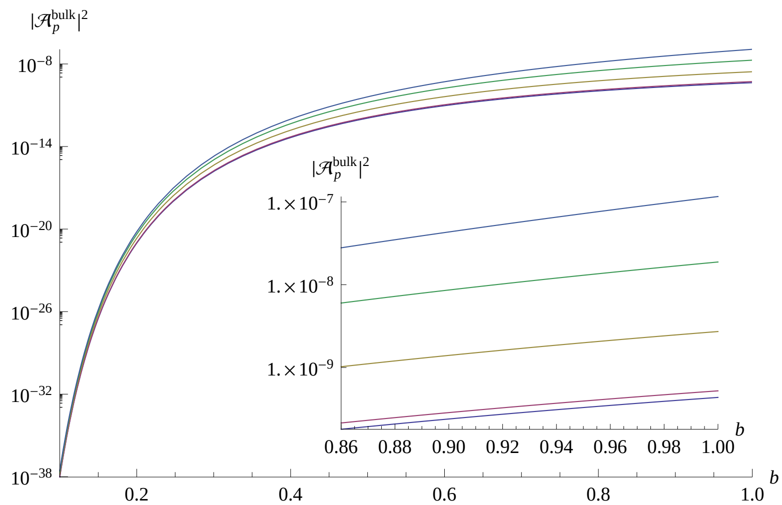

Figure 4.1: Low frequency absorption probability for bulk emissions as a function of b. Parameter $p \in \left\{0, \frac{1}{2}, \frac{3}{2}, 2, 2.25\right\}$ from eq. (2.8) increases from bottom to top. Here, $\ell_3 = 2$, $m = 1$, $\omega = 0.2$, and $\mu = 1$.

of this result. Figure (4.1) depicts the absorption probability as a function of b with ω fixed. As can be seen, all types of perturbation exhibit the same qualitative behavior with the probability vanishing as $b \to 0$ and increasing monotonically as $b \to 1$. This behavior persists qualitatively at high frequency as demonstrated in figure (4.2) which was obtained from points generated by exactly solving for absorption probability numerically. A further demonstration of how tension suppresses the absorption probability is provided in figure (4.3), where probability *vs* frequency in the case of a scalar perturbation is plotted for various values of b in the small frequency regime. The graph also has points representing exact numerical calculations. As expected, the predictions of the analytical formula diverge from the exact values with increasing frequency. Finally, figure (4.4) shows the effect of the magnetic quantum number m in the case of scalar emission. The qualitative behavior of all curves is the same, however the absorption probability varies over many orders of magnitude depending on m. In figs. (4.3) and (4.4), the type of perturbation chosen has a negligible effect on the outcome.

Moving on to the case of brane localized modes (the photon, massless fermion and scalar), we notice that because we are projecting onto the brane, angles χ and

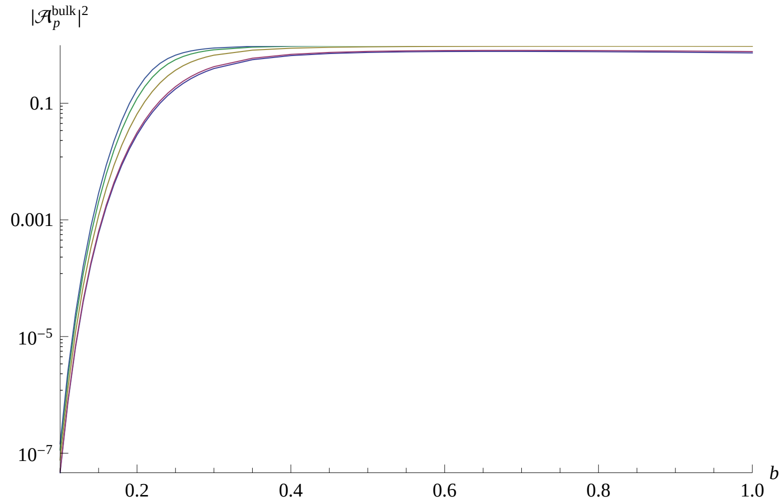

Figure 4.2: High frequency absorption probability for bulk emissions as a function of b. Parameter $p \in \left\{0, \frac{1}{2}, \frac{3}{2}, 2, 2.25\right\}$ from eq. (2.8) increases from bottom to top. Here, $\ell_3 = 2$, $m = 1$, $\omega = 2.2$, and $\mu = 1$.

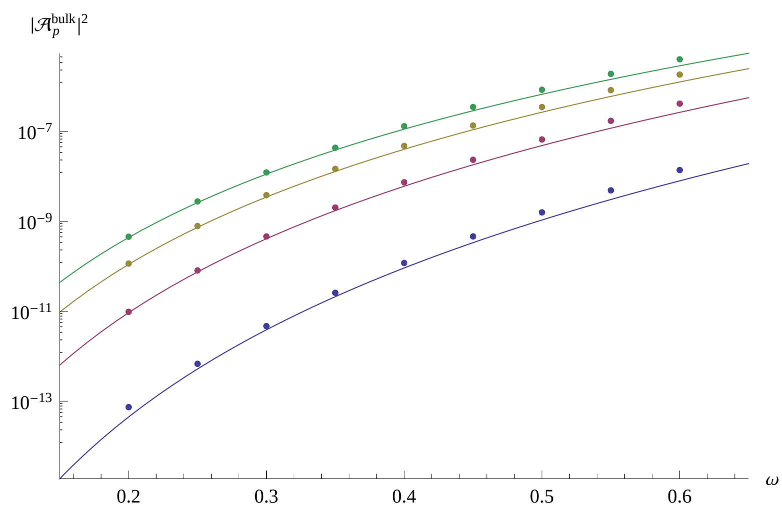

Figure 4.3: Absorption probability for bulk scalars ($p = 0$) as a function of ω for various values of brane tension, where $b \in \{0.4, 0.6, 0.8, 1\}$ increasing from bottom to top, with $\ell_3 = 2, m = 1, \mu = 1$. The points on the graph come from exact numerical calculations.

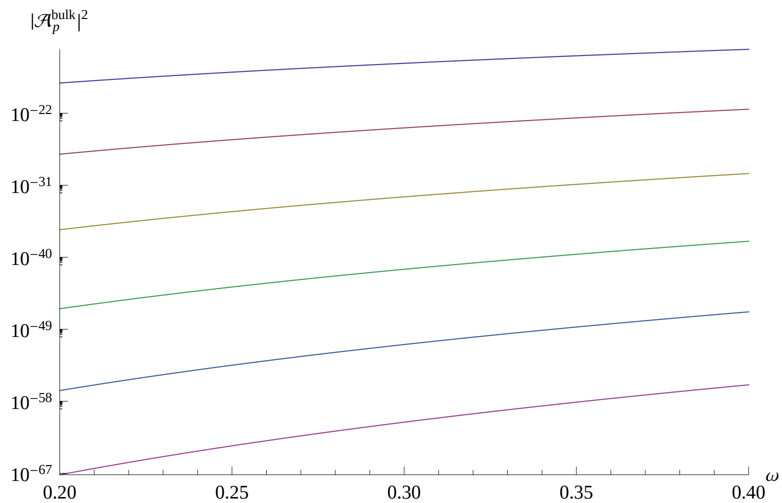

Figure 4.4: Bulk absorption probability for scalars for different values of m: for $\ell_3 = 5$, and $m \leq \ell_3$, m increasing top to bottom, where $b = 0.3$, $\mu = 1$.

ψ will be fixed, so that the dependence of the metric on b will only be through r_h inside the metric function f, and aside from that the results of the grey-body factors will be identical to those in the tensionless case. To find these grey-body factors we follow the same procedure as above, but instead using an equation analogous to the Teukolsky equation on the brane. For a static background, the radial wave equation is the one given in equations (2.12) and (2.13), with the corresponding angular equation in (2.15). For $s = \frac{1}{2}$, the absorption probability as found by P. Kanti (2003) is:

$$\left|\mathcal{A}_{s=1/2}^{\text{brane}}\right|^2 = 4\pi \left(\frac{\omega r_h}{2^{5/3}}\right)^{2j+1} \frac{1}{\left[\Gamma\left(j+1\right)\right]^2} \tag{4.18}$$

and for $s = 1$

$$\left|\mathcal{A}_{s=1}^{\text{brane}}\right|^2 = \frac{1}{9}\left(2\omega r_h\right)^{2j+2} \left[\frac{\Gamma\left(\frac{j}{3}\right)\Gamma\left(\frac{j+1}{3}\right)\Gamma\left(j+2\right)}{\Gamma\left(\frac{2j+1}{3}\right)\Gamma\left(2j+2\right)}\right]^2 \tag{4.19}$$

where j is the total angular momentum in both cases.

For brane-localized scalars P. Kanti (2003) found:

$$\left|\mathcal{A}_{s=0}^{\mathrm{brane}}\right|^2 = \frac{16\pi}{9}\left(\frac{\omega r_h}{2}\right)^{2j+2}\left[\frac{\Gamma\left(\frac{j+1}{3}\right)\Gamma\left(1+\frac{j}{3}\right)}{\Gamma\left(\frac{1}{2}+j\right)\Gamma\left(1+\frac{2j+1}{3}\right)}\right]^2 \tag{4.20}$$

Upon comparison of (4.19) and (4.20), we obtain

$$\frac{\left|\mathcal{A}_{s=0}^{\mathrm{brane}}\right|^2}{\left|\mathcal{A}_{s=1}^{\mathrm{brane}}\right|^2} = \left(\frac{j}{1+j}\right)^2 \tag{4.21}$$

which shows that (in this frequency regime) the gauge vector and scalar behave the same up to a multiplicative factor, which tends to unity for large j. But one can see from the expressions above that only the first few values of j contribute to the emission spectrum making the emission rate for scalars higher than for gauge vectors in this frequency range, which can be seen numerically in the absence of tension in the results of Jung and Park (2007). At higher frequencies the situation reverses, and the rate for scalars becomes smaller. Graphs analogous to those for bulk emissions are shown in figures (4.8) and (4.9) for scalars. For low frequencies, the behavior with tension is now reversed, where emission is enhanced with increased tension, for higher frequencies the trend is not as conclusive. The difference between the two behaviors can be understood based on two competing effects: the enhancement of geometrical cross-section with tension implies an increased rate of emission for both bulk and brane-localized modes, and the fact that the angular eigenvalues increase with tension, and that they appear only in the bulk potential causing the potential barrier to increase, which results in suppression that appears only in bulk emissions.

From an experimental point of view, it is of great interest to know the relative emissivities between brane and bulk modes. The above discussion seems to hint that the inclusion of tension favors the EHM conjecture (see Emparan et al. (2000)), namely, that black-holes emit mainly on the brane. To verify this in our case, let us consider the emission spectrum as defined in eq. (4.1) for scalars. For that, we need to write the grey-body factor $\sigma_{\ell,\kappa}(\omega)$ in terms of the absorption probability $|\mathcal{A}|^2$ and scalar multiplicities $N_{\ell,m}$. For either bulk or brane-localized emissions we have the following form:

$$\frac{\mathrm{d}E(\omega)}{\mathrm{d}t\,\mathrm{d}\omega} = \frac{1}{2\pi}\sum_{\ell,m} N_{\ell,m}\,|\mathcal{A}_{\ell,m}|^2\,\frac{\omega}{e^{\omega/T_{\mathrm{H}}}-1} \tag{4.22}$$

In the bulk, the scalar multiplicities according to Dai et al. (2007) are:

$$N^{\mathrm{scal}}_{\ell_3,m} = \begin{cases} m=0, & \frac{1}{2}(\ell_3+2)(\ell_3+1) \\ m\neq 0, & (\ell_3-m+2)(\ell_3-m+1) \end{cases} \tag{4.23}$$

whereas on the brane they become the usual $2\ell+1$. Starting with the bulk, we numerically solve eq. (4.4) for the absorption probability with $p=0$, and using eq. (4.23), we end up with the spectrum shown in fig. (4.10). A similar calculation done this time for brane-localized scalars is done by projecting the bulk equation on the brane, and the result is shown in fig. (4.5). We notice now that in both figures, the emission rates are enhanced with tension. The reason for this comes primarily not from the grey-body factor, but rather from the denominator in the black-body distribution which depends on the Hawking temperature, and which is common to both types of emission. We can discount this effect by looking at the relative emissivity, in which we take the ratio of the emission rate in the bulk to that on the brane. Figure (4.6) shows this for scalars.

Similar plots are obtained for gauge vectors. On the brane, we again have the multiplicities $2\ell+1$, but in the bulk we have

$$N^{\mathrm{vec}}_{\ell_3,m} = \begin{cases} m=0, & \frac{1}{2}\ell_3(3\ell_3+5) \\ m\neq 0, & 3(\ell_3-m+2)(\ell_3-m+1) \end{cases} \tag{4.24}$$

In the bulk, we solve eq. (4.4) with $p=\frac{1}{2}$, and on the brane eq. (2.12) is solved with $s=1$. The results of doing this are shown in figures (4.11) through (4.13). In this case the emissivity is only partial, since the scalar degree of freedom is not included.

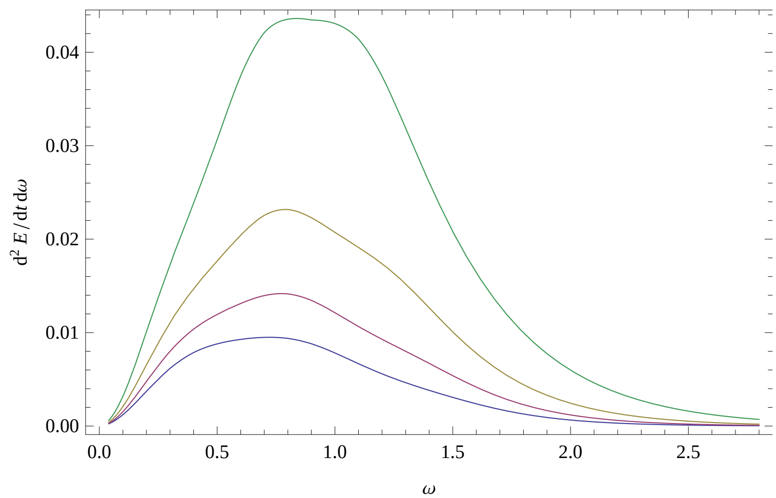

Figure 4.5: Energy emission spectrum for scalars on the brane for various values of brane tension, with $b \in \{0.4, 0.6, 0.8, 1\}$ increasing from top to bottom.

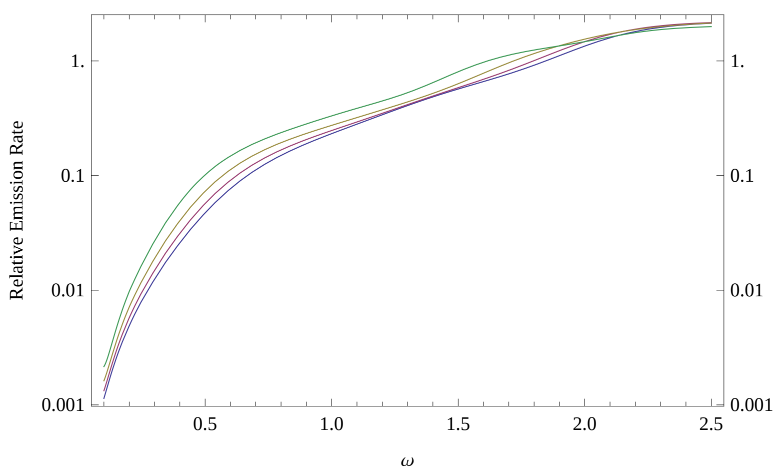

Figure 4.6: Relative bulk-to-brane emissivity for scalars for different values of brane tension, with $b \in \{0.4, 0.6, 0.8, 1\}$ increasing from top to bottom.

We can see that in both cases, the emission rate is greater on the brane than in the bulk, in the range shown, in support of the EHM claim.

4.2 High-Frequency Grey-Body Factors

Next we turn our attention to grey-body factors at large imaginary frequencies. We shall discuss different values of spin and take into account the extra dimensions as well as the brane tension in the codimension-2 model. The calculation will follow the method of Andersson and Howls (2004) which was then used by Cho (2006). It is a combination of the monodromy argument of Motl and Neitzke (2003) and the standard complex-coordinate WKB method.

The first step is to rewrite the master equation (2.5) in a form suitable for the application of the WKB method. To this end, we introduce the redefinition of the wavefunction,

$$\Psi = \frac{\phi}{\sqrt{f}} \tag{4.25}$$

which reduces (2.5) to

$$\phi''(r) + Q^2(r)\phi(r) = 0 \tag{4.26}$$

The resulting WKB solution is

$$\phi_{1,2}^{(t)} = \frac{1}{\sqrt{Q(r)}} \exp\left[\pm i \int_t^r Q\left(r'\right)\, dr'\right] \tag{4.27}$$

with t being a reference point, and

$$Q^2(r) = \frac{1}{f^2(r)}\left[\omega^2 - V(r) + \frac{1}{4}(f'(r))^2 - \frac{1}{2}f(r)f''(r)\right] \tag{4.28}$$

Integer spin particle are described by the potential (2.7).

Following Motl and Neitzke (2003), we will go around a contour in the complex r-plane and impose preservation of monodromy. Because of the exponential nature of the WKB solutions, dominance will be exchanged between the two exponentials as we move around the complex plane. This implies that some terms that are exponentially small and can be overlooked in one region of the complex plane can grow exponentially in a different region. To take this into account, one needs to resort to the Stokes phenomenon which keeps track of these changes.

In such an analysis, we need to pay attention to the zeroes and poles of $Q(r)$. In particular, it can be shown that from each simple zero of Q there emanate 3 Stokes lines along which $Q(r)\mathrm{d}r$ is imaginary. This means that one of the two solutions $\phi_{1,2}^{(t)}$ will grow exponentially whereas the other one will decay as we move away from the reference point t. On the other hand, we can also define anti-Stokes lines emanating from each zero of Q along which $Q(r)\mathrm{d}r$ is real and $\phi_{1,2}^{(t)}$ are oscillatory functions. By crossing anti-Stokes lines, the exponential behaviors of the two solutions are switched, while extending the solution across a Stokes line, the linear combination defining the solution is changed in a well-defined way: the coefficient of the dominant term stays the same, but that of the sub-dominant term picks up a contribution proportional to the coefficient of the dominant term. Thus we see that the appropriate contour that can be used will trace anti-Stokes lines and cross Stokes lines. Figure (4.7) shows such a contour for Schwarzschild geometry assuming (large) purely imaginary frequency.

One can see from the potential (2.7) that for $|\Im\omega| \to \infty$, all zeroes of Q approach the origin and the potential may be approximated by its expansion around $r = 0$. In this case, the ℓ-dependent terms are negligible. They enter in subleading contributions (see Musiri and Siopsis (2003); van den Brink (2004)). Near $r = 0$, keeping only the most singular term, the potential in (2.7), which describes integer-spin perturbations, becomes:

$$V_{\text{bulk}} \sim \frac{1}{4}(2+n)^2(p^2-1)\frac{r_h^{2(1+n)}}{r^{2(2+n)}} \tag{4.29}$$

and the resulting WKB equation is:

$$\psi''(r) + R_0(r)\psi(r) \simeq 0 \tag{4.30}$$

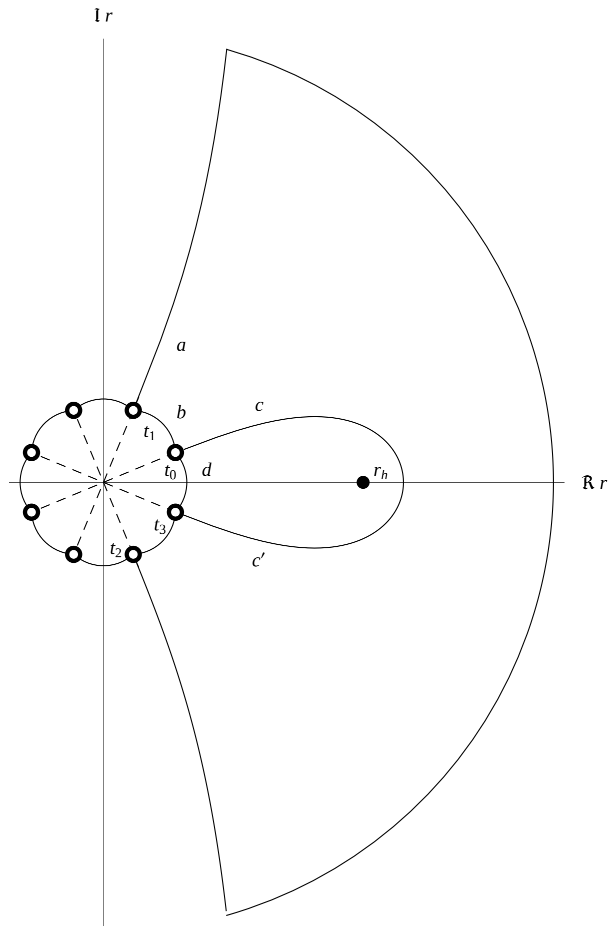

Figure 4.7: Stokes lines structure for the Schwarzschild black hole in 6D in the complex r-plane for large imaginary frequency. Empty circles are the zeros of Q and the filled circle is the horizon radius

where

$$R_0(r) = \left(\frac{r}{r_h}\right)^{2n+2}\left[\omega^2 - \frac{1}{4r^{2(n+2)}}\left(\left(p^2-1\right)(n+2)^2 + (n+1)(n+3)\right)r_h^{2(n+1)}\right] \tag{4.31}$$

However, one can show Andersson and Howls (2004) that the solutions $\phi_{1,2}^{(t)}$ so obtained by identifying $R_0(r)$ with $Q^2(r)$, do not have the right behavior near the origin when compared with the exact solution near there. This can be rectified by using a slightly different $R(r)$, which is permissible. The modified form turns out to be:

$$R(r) = R_0(r) - \frac{1}{4r^2} \equiv Q^2(r) = \left(\frac{r}{r_h}\right)^{2(n+1)}\left[\omega^2 - \frac{(n+2)^2p^2}{4r^{2(n+2)}}r_h^{2(n+1)}\right] \tag{4.32}$$

For $\omega = -i|\omega|$, the zeros of Q^2 are:

$$r_k = \left(\frac{(n+2)p}{2|\omega|}\right)^{\frac{1}{(n+2)}} r_h^{\frac{n+1}{n+2}} e^{\frac{\pi i}{n+2}\left(k+\frac{1}{2}\right)}, \quad k = 0, 1, \cdots 2(2+n)-1 \tag{4.33}$$

These zeros will serve as reference points for the phase integrals, because in doing so, the Stokes constants are either $+i$ for traveling anti-clockwise (or $-i$ for clockwise), and so, we will need to switch between reference points as we go around the contour:

$$\phi_{1,2}^{(t_k)} = e^{\mp i\nu_{jk}}\phi_{1,2}^{(t_j)} \tag{4.34}$$

with

$$\nu_{jk} = \int_{r_j}^{r_k} Q\,\mathrm{d}r = \frac{\omega}{r_h^{n+1}}\int_{r_j}^{r_k} r^{n+1}\left[1 - \frac{(n+2)^2p^2}{4\omega^2 r^{2(n+2)}}r_h^{2(n+1)}\right]^{1/2}\mathrm{d}r \tag{4.35}$$

where j and k label two consecutive zeros. Using the substitution $y \equiv \frac{2\omega r^{n+2}}{(n+2)pr_h^{n+1}}$, followed by $y \equiv \cosh x$, we get:

$$\nu_{jk} = \int_{r_j}^{r_k} Q\,dr = \frac{p}{2}\int_{e^{i\pi j}}^{e^{i\pi k}}\left[1 - \frac{1}{y^2}\right]^{1/2} dy = \left(\frac{e^{i\pi j} - e^{i\pi k}}{2}\right)\frac{\pi p}{2} \tag{4.36}$$

so that:

$$\nu_{10} = \nu_{30} \equiv \nu = -\frac{\pi p}{2} \equiv \nu_{\text{bulk}} \tag{4.37}$$

It is also possible to consider a massless Dirac fermion propagating in the bulk, which can be relevant in split-fermion theories where rapid proton decay can suppressed by introducing bulk fermions Cho et al. (2008a, 2007) that are superpartners to localized scalars and gauge bosons. A master equation potential based on a higher-dimensional Dirac equation potential was derived in Cho et al. (2007):

$$V_{\text{bulk-Dirac}} = f\frac{\mathrm{d}}{\mathrm{d}r}\left[\sqrt{f}\left(\frac{\ell + \frac{D-2}{2}}{r}\right)\right] + f\left(\frac{\ell + \frac{D-2}{2}}{r}\right)^2 \tag{4.38}$$

By expanding near $r = 0$, we find this potential to be proportional to $r^{-(7+3n)/2}$, which, for the present purpose, can be treated as zero when compared to the other bulk perturbation given by (4.29). At this approximation, therefore, we may use $p = 1$ for a bulk Dirac fermion.

Turning our attention to the actual calculation of grey-body factors, we see that since ω in the present case is not real, the conservation of flux will take on the following generalized form:

$$T(\omega)T(-\omega) + R(\omega)R(-\omega) = 1 \tag{4.39}$$

and therefore, we consider two separate solutions representing the boundary condition at physical infinity; one with frequency ω and the other with $-\omega$. In the first case, the reflected wave at infinity is represented by $\phi_1^{(t_1)}(r)$, while the ingoing wave by $\phi_2^{(t_1)}(r)$. For $-\omega$, the two solutions switch roles, but the calculation is effectively the same, and we shall combine them into one by writing the wavefunction in general as:

$$\psi = Xe^{i\theta}\phi_1^{(t_j)} + Ye^{-i\theta}\phi_2^{(t_j)} \tag{4.40}$$

where θ is a phase angle. In the case of $+\omega$, $X = R_+$ and $Y = 1$, whereas for $-\omega$, $X = 1$ and $Y = R_-$. For $\Re(\omega M) > 0$, the outgoing wave boundary condition at spatial infinity can be analytically continued to the anti-Stokes line labeled a in the figure. To find the the T's and R's we need to travel a path on anti-Stokes lines starting and ending at point a. The solution ψ_a at point a for $\pm\omega$ is described by the wavefunction given in (4.40) with $j = 1$. Since we don't cross any Stokes lines in extending the solution to t_1, the above expression remains valid there, but in going to point b we do cross a Stokes line, and to account for the Stokes phenomenon we need to add to ψ_a a contribution proportional to ϕ_2 with the constant of proportionality equal to the Stokes constant multiplied by the coefficient of the dominant function on the Stokes line, ϕ_1 in this case, so that:

$$\psi_b = \psi_a - iXe^{i\theta}\phi_2^{(t_1)} = Xe^{i\theta}\phi_1^{(t_1)} + \left(Ye^{-i\theta} - iXe^{i\theta}\right)\phi_2^{(t_1)} \tag{4.41}$$

To extend the solution to point c, we now need to change the lower limit of integration to have t_0 as reference:

$$\psi_b = Xe^{i\theta-i\nu}\phi_1^{(t_0)} + \left(Ye^{-i\theta+i\nu} - iXe^{i\theta+i\nu}\right)\phi_2^{(t_0)} \tag{4.42}$$

In going to point c there will be no exchange in dominance, since we cross no anti-Stokes lines:

$$\psi_c = \psi_b - iXe^{i\theta-i\nu}\phi_2^{(t_0)} = Xe^{i\theta-i\nu}\phi_1^{(t_0)} + \left(Ye^{-i\theta+i\nu} - iXe^{i\theta+i\nu} - iXe^{i\theta-i\nu}\right)\phi_2^{(t_0)} \tag{4.43}$$

We now go to point c', and in doing so we cross no Stokes lines, so that the combination (4.43) remains valid, but now the integral is evaluated around a contour that loops around the pole $r = r_h$. Replacing that contour by the one to the left of the pole, we have:

$$\psi_{c'} = Xe^{i\theta-i\nu}e^{i\Gamma}\phi_1^{(t_0)} + \left(Ye^{-i\theta+i\nu} - iXe^{i\theta+i\nu} - iXe^{i\theta-i\nu}\right)\phi_2^{(t_0)}e^{-i\Gamma} \tag{4.44}$$

where Γ is the integral encircling $r = r_h$ clockwise:

$$\Gamma_{\text{bulk}} = \oint Q \,\mathrm{d}r = -2\pi i \operatorname*{Res}_{r=r_h} Q = -i\pi\sqrt{1 + \left(\frac{2\omega r_h}{n+1}\right)^2} \approx -\frac{1}{2}i\pi\beta \tag{4.45}$$

where $\beta = 1/T_{\mathrm{H}}$. To connect the solution to point d, we need to change the lower integration limit to t_3:

$$\psi_{c'} = Xe^{i\theta}e^{i\Gamma}\phi_1^{(t_3)} + \left(Ye^{-i\theta} - iXe^{i\theta-2i\nu} - iXe^{i\theta}\right)\phi_2^{(t_3)}e^{-i\Gamma} \tag{4.46}$$

and now to connect to point d, we need to cross the anti-Stokes line to get inside the loop, and this means that ϕ_1 and ϕ_2 will interchange dominance; further, the Stokes constant is now i, since we have reversed direction:

$$\begin{aligned}
\psi_d &= \psi_{c'} + i\left(Ye^{-i\theta} - iXe^{i\theta-2i\nu} - iXe^{i\theta}\right)\phi_1^{(t_3)}e^{-i\Gamma} \\
&= \left[Xe^{i\theta}e^{i\Gamma} + \left(iYe^{-i\theta} + Xe^{i\theta-2i\nu} + Xe^{i\theta}\right)e^{-i\Gamma}\right]\phi_1^{(t_3)} \\
&+ \left(Ye^{-i\theta} - iXe^{i\theta-2i\nu} - iXe^{i\theta}\right)\phi_2^{(t_3)}e^{-i\Gamma}
\end{aligned} \tag{4.47}$$

Then switching back to point t_0:

$$\begin{aligned}
\psi_d = &\left[Xe^{i\theta}e^{i\Gamma}e^{-i\nu} + \left(iYe^{-i\theta}e^{-i\nu} + Xe^{i\theta-3i\nu} + Xe^{i\theta}e^{-i\nu}\right)e^{-i\Gamma}\right]\phi_1^{(t_0)} \\
&+ \left(Ye^{-i\theta}e^{i\nu} - iXe^{i\theta-i\nu} - iXe^{i\theta}e^{i\nu}\right)\phi_2^{(t_0)}e^{-i\Gamma}
\end{aligned} \tag{4.48}$$

Going back to point c and crossing a Stokes line, we encircle the pole at the origin:

$$\begin{aligned}
\psi_{\bar{c}} = &\left[\left(2e^{-i\nu} + e^{i\nu} + e^{-3i\nu}\right)e^{i(\theta-\Gamma)}X + e^{i(-\nu+\Gamma+\theta)}X + i\left(e^{-i\nu} + e^{i\nu}\right)e^{-i(\Gamma+\theta)}Y\right]\phi_1^{(t_0)} \\
&+ e^{-i\Gamma}\left[-ie^{i(-\nu+\theta)}X - ie^{i(\nu+\theta)} + e^{i(\nu-\theta)}\right]\phi_2^{(t_0)}
\end{aligned} \tag{4.49}$$

where the bar is to indicate that we have encircled the pole at the origin. Connecting to point b:

$$\begin{aligned}\psi_{\bar{b}} = &\left[\left(2e^{-i\nu} + e^{i\nu} + e^{-3i\nu}\right) e^{-i\Gamma} X + e^{i(-\nu+\Gamma)} X + i\left(e^{-i\nu} + e^{i\nu}\right) e^{-i(\Gamma+2\theta)} Y\right] e^{i\theta} \phi_1^{(t_0)} \\ &+ \left[i\left(e^{-i\Gamma} e^{-2i\nu-i\Gamma} + e^{i\Gamma}\right) e^{i(\theta-\nu)} X - e^{-i(\nu+\Gamma+\theta)} Y\right] \phi_2^{(t_0)}\end{aligned} \tag{4.50}$$

switching to reference point t_1:

$$\begin{aligned}\psi_{\bar{b}} = &\left[\left(2 + e^{2i\nu} + e^{-2i\nu}\right) e^{-i\Gamma} X + e^{i\Gamma} X + i\left(1 + e^{2i\nu}\right) e^{-i(\Gamma+2\theta)} Y\right] e^{i\theta} \phi_1^{(t_1)} \\ &+ \left[i\left(e^{-i\Gamma} + e^{-2i\nu-i\Gamma} + e^{i\Gamma}\right) e^{i(\theta-2\nu)} X - e^{-i(2\nu+\Gamma+\theta)} Y\right] \phi_2^{(t_1)}\end{aligned} \tag{4.51}$$

and finally returning to point a:

$$\begin{aligned}\psi_{\bar{a}} = &\, e^{-i\Gamma}\left[e^{i\theta}\left(2(1+\cos(2\nu)) + e^{2i\Gamma}\right) X + 2ie^{i(\nu-\theta)} \cos(\nu) Y\right] \phi_1^{(t_1)} \\ &+ e^{-i\Gamma}\left[2ie^{i(\theta-\nu)} \cos\nu \left(1 + e^{2i\Gamma} + 2\cos(2\nu)\right) X - e^{-i\theta}(1 + 2\cos(2\nu)) Y\right] \phi_2^{(t_1)}\end{aligned} \tag{4.52}$$

To find $R(\omega)$ we need to properly impose the boundary conditions on X and Y, where Y will be set to unity, then we identify the coefficient of ϕ_1 in $\psi_{\bar{a}}$ as the same coefficient appearing in ψ_a, except that because of the trip around the contour we have gained a phase:

$$e^{-i\Gamma}\left[e^{i\theta}\left(2(1+\cos(2\nu)) + e^{2i\Gamma}\right) R + 2ie^{i(\nu-\theta)} \cos(\nu)\right] = e^{i\theta} X e^{-i\Gamma} \tag{4.53}$$

Solving for R gives us the desired result:

$$R(\omega) = -e^{i(\nu-2\theta)} \frac{2i\cos\nu}{e^{\beta\omega} + 1 + 2\cos(2\nu)} \tag{4.54}$$

To find the corresponding T, we notice that the boundary condition at the horizon, with ϕ_2 dominating can be connected to point d, which was reached by moving along an anti-Stokes line along which ϕ_2 is dominant when $\omega \to -i\infty$. Therefore, we can make the following identification:

$$\psi_d = \cdots + Te^{-i\theta}\phi_2^{(t_3)}e^{-i\Gamma} \tag{4.55}$$

comparing with the expression obtained in (4.48), we can solve for $T(\omega)$:

$$T(\omega) = \frac{e^{\beta\omega} - 1}{1 + 2\cos(2\nu) + e^{\beta\omega}} \tag{4.56}$$

For the case of $-\omega$, we just flip the roles of X and Y, so that $Y = R(-\omega)$ is now obtained as follows:

$$\psi_{\bar{a}} = \cdots + R(-\omega)e^{-i\theta}\phi_2^{(t_1)}e^{i\Gamma} \tag{4.57}$$

with $X \equiv 1$. By comparing with (4.52), we find:

$$R(-\omega) = 2ie^{i(2\theta-\nu)}\cos\nu \tag{4.58}$$

Likewise, to find $T(-\omega)$, we make the identification

$$\psi_d = Te^{-i\theta}\phi_1^{(t_3)}e^{-i\Gamma} + \cdots \tag{4.59}$$

and by comparing with the expression in (4.48) we find that:

$$T(-\omega) = 1 \tag{4.60}$$

The grey-body factor that results from this reads:

$$\gamma(\omega) = T(\omega)T(-\omega) = \frac{e^{\beta\omega} - 1}{1 + 2\cos(2\nu) + e^{\beta\omega}} \tag{4.61}$$

This result is consistent with the asymptotic quasinormal frequencies found by Cho (2006) in 4D, and it also implies Neitzke (2003)'s results for scalar perturbation around a Schwarzschild hole for dimensions $D \geq 4$, where the only modification due to extra dimensions appears through the Hawking temperature (cf. eq. (1.2)). Further, in the 6D model that includes tension, one finds that an additional modification appears (cf. eq. (2.24)). Moving on to brane-localized emissions, we need to use eq. (2.12) as the radial master equation. This would describe scalar emissions ($s = 0$), massless Dirac fermions ($s = \frac{1}{2}$), and gauge photons ($s = 1$). To apply our method, we need to put that equation in the Schrödinger form, in which case the potential according to Jung and Park (2007) looks like this:

$$\begin{aligned} V_s(r) = \frac{f}{r^2}\left[\mathcal{A}_{js} + q_{ns}(1-f) + \frac{s^2}{4f}\left\{(n+1)(1-f) - 2f\right\}^2 + sf\right] \\ + \frac{i\omega s}{r}\left\{(n+1)(1-f) - 2f\right\} \end{aligned} \tag{4.62}$$

where

$$q_{ns} = (2s+n+1)(ns+s+1) - (s/2)(n+1)(n+4)$$

and

$$\mathcal{A}_{js} = j(j+1) - s(s+1)$$

To also talk about the graviton localized to the brane, we have to use another potential ($e.g$ Park (2006)):

$$V_G(r) = \frac{f}{r^2}\left[j(j+1) - \left\{(n+1)^2 + 2\right\}(1-f)\right] \tag{4.63}$$

However, for our purpose, what we care about is the behavior of these potentials near $r = 0$. Keeping only the most singular term in both cases, we can combine the two potentials into one expression:

$$V_{\text{brane}} \sim \sigma_n \frac{r_h^{2(1+n)}}{r^{2(2+n)}} \tag{4.64}$$

with

$$\sigma_n = \begin{cases} \frac{1}{4}s^2(n-1)^2 - \frac{1}{2}sn(n-1) - (n+1), & \text{for } s = 0, \frac{1}{2}, 1 \\ (n+1)^2 + 2, & \text{for } s = 2 \end{cases} \tag{4.65}$$

To find the greybody factors in this case, we duplicate our steps for bulk emissions, and we find that the only difference occurs in the ν, which we can readily find by comparing the expressions (4.64) and (4.29):

$$\nu_{\text{brane}} = -\pi\sqrt{\frac{\sigma_n}{(n+2)^2} + \frac{1}{4}} \tag{4.66}$$

In this case, the value of the contour integral Γ_{brane} is found to be:

$$\Gamma_{\text{brane}} = \oint Q\,\mathrm{d}r = -i\pi\sqrt{1 - \left(\frac{s(n+1) + 2i\omega r_h}{n+1}\right)^2} \approx -\frac{1}{2}i\pi\beta \tag{4.67}$$

which is asymptotically the same as Γ_{bulk}.

In looking at these results, we see that the grey-body factors in all cases are governed by (4.61) with differences coming through the value of ν. Tables (4.1) and (4.2) summarize this for bulk and brane-localized emissions, respectively.

Table 4.1: Expressions for ν for different bulk perturbations

Perturbation	ν_{bulk}
scalar & gravi-tensor	0
gravi-vector	$-\pi$
EM vector	$-\frac{1}{n+2}\pi$
EM scalar	$-\frac{n+1}{n+2}\pi$
gravi-scalar	$\sim -\frac{\pi}{2}\left[2 + 0.674(n+4)^{-0.5445}\right]$
Dirac fermion	$-\frac{\pi}{2}$

Table 4.2: Expressions for ν for different brane-localized perturbations

Spin	ν_{brane}
0	$-\frac{\pi n}{2(n+2)}$
$\frac{1}{2}$	$-\frac{\pi}{2^{3/2}}\frac{\sqrt{1+n^2}}{n+2}$
1	$-\pi\frac{\sqrt{n(n-2)+2}}{2(n+2)}$
2	$-\pi\sqrt{\frac{(n+1)^2+2}{(n+2)^2} + \frac{1}{4}}$

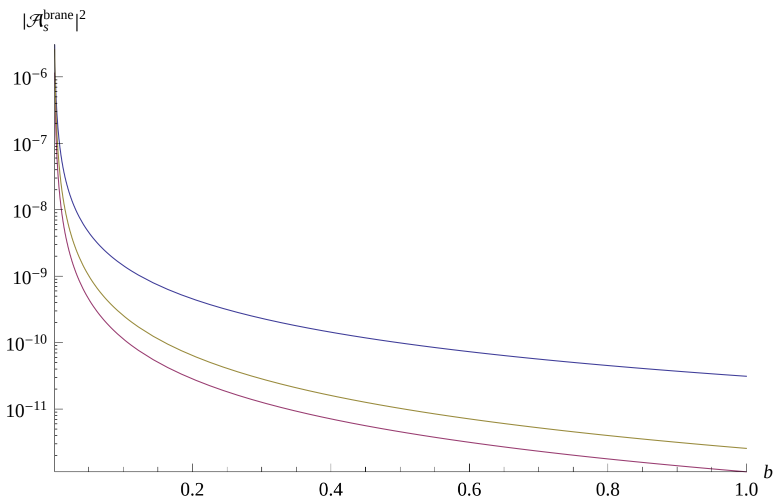

Figure 4.8: Absorption probability for brane-localized emissions as a function of b. The curves from top to bottom correspond to $s = \frac{1}{2}$, $s = 0$ and $s = 1$, respectively. Here, $\ell = 2$, $\omega = 0.02$, and $\mu = 1$.

Recalling that the asymptotic quasinormal frequencies are the poles of the greybody factor, we see that the usual formula still holds in form:

$$\frac{\omega}{T_{\rm H}} = 2\pi i \left(\tilde{n} + \tfrac{1}{2}\right) + \ln\left(1 + 2\cos 2\nu\right) \tag{4.68}$$

where $\tilde{n}$ is the mode number. Now, however, ν has structure that depends on the number of extra dimensions; as already found in Park (2006).

As a special case, the addition of tension in an $n = 2$ spacetime, will only modify $T_{\rm H}$, where it can be seen from equations (2.24) and (1.2) that the Hawking temperature decreases with brane tension:

$$T_{\rm H} \to b^{1/3} T_{\rm H} \tag{4.69}$$

Since this occurs in an exponential, even a moderate value of b can be considerably magnified, and $\gamma(\omega)$ would tend to one faster with frequency.

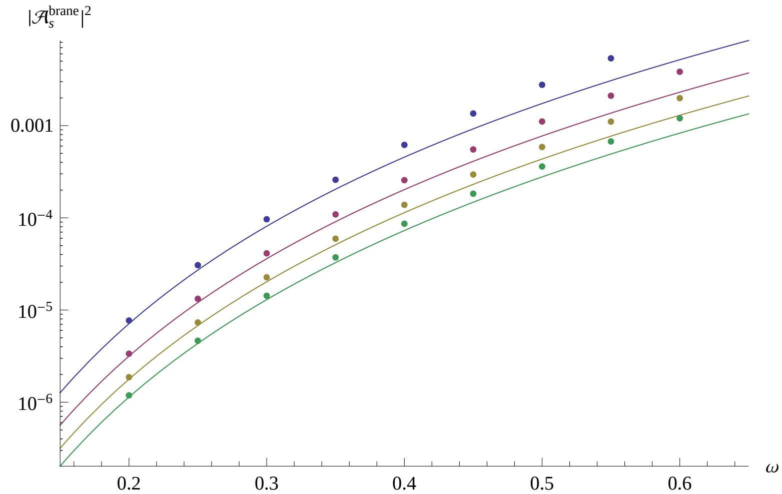

Figure 4.9: Absorption probability for brane-localized scalars ($s = 0$) as a function of ω for various values of brane tension, where $b \in \{0.4, 0.6, 0.8, 1\}$ increasing from top to bottom, with $\ell = 2, m = 1, \mu = 1$. The points on the graph come from exact numerical calculations.

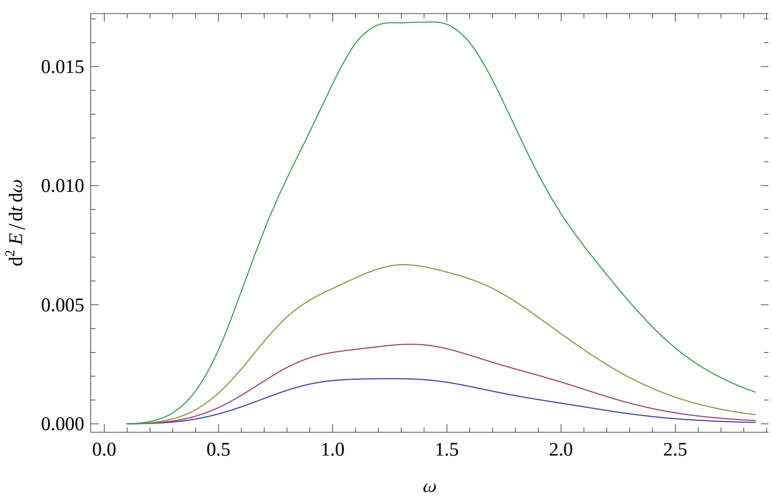

Figure 4.10: Energy emission spectrum for scalars in the bulk for various values of brane tension, with $b \in \{0.4, 0.6, 0.8, 1\}$ increasing from top to bottom.

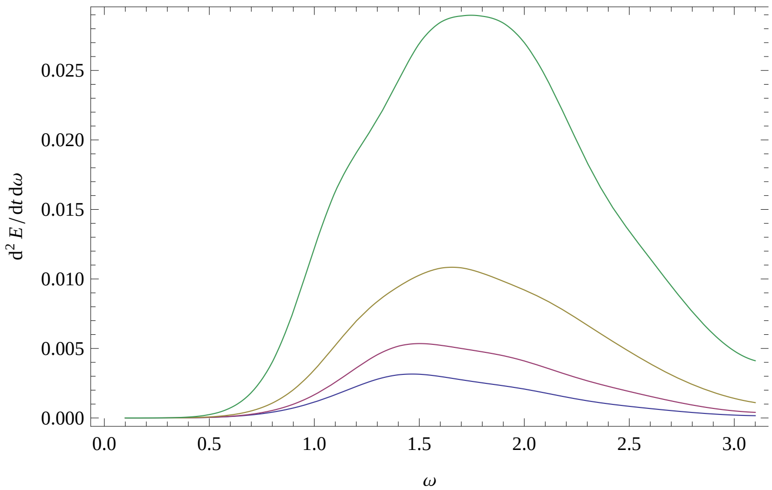

Figure 4.11: Energy emission spectrum for gauge vectors in the bulk for various values of brane tension, with $b \in \{0.4, 0.6, 0.8, 1\}$ increasing from top to bottom.

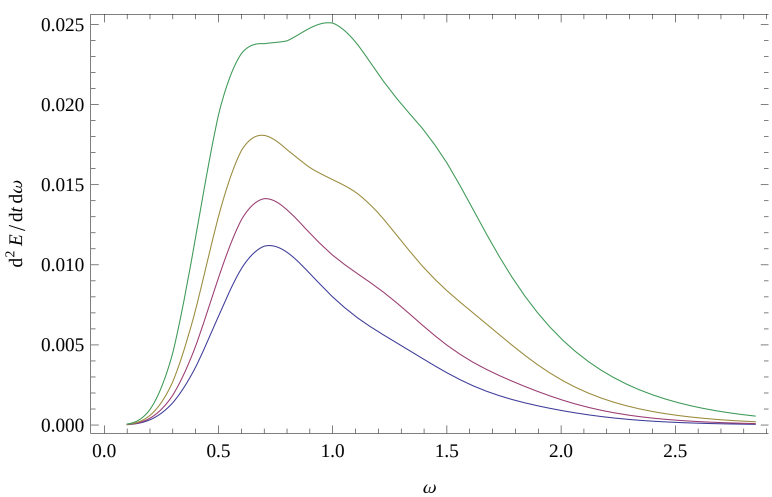

Figure 4.12: Energy emission spectrum for gauge vectors on the brane for various values of brane tension, with $b \in \{0.4, 0.6, 0.8, 1\}$ increasing from top to bottom.

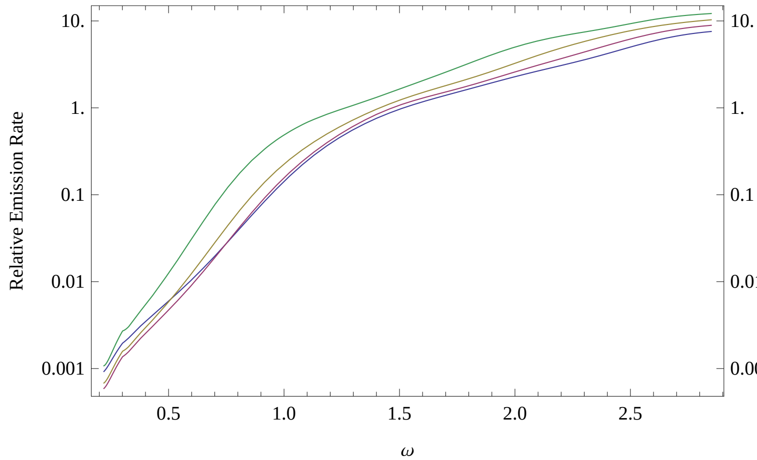

Figure 4.13: Relative bulk-to-brane emissivity for gauge vectors for different values of brane tension, with $b \in \{0.4, 0.6, 0.8, 1\}$ increasing from top to bottom.

4.3 Summary and Conclusions

In this chapter we explored some of the implications of the codimension-2 model on grey-body factors for various types of bulk and brane emissions from a black hole residing on a brane of finite tension.We saw that the results presented follow primarily from two modifications: (a) the enhancement of the horizon radius, which enhanced the emission spectra with increasing tension, and (b) the increase of the angular eigenvalues with tension, which resulted in an amplified absorption probability on the brane. We calculated analytically grey-body factors in the low-frequency regime for the perturbations considered (in the case of gravitational scalars, the calculation was not purely analytical, because it relied on an approximate potential). We obtained expressions that had a nontrivial dependence on the brane tension with observable implications which we discussed. In particular, we saw that the observable emission rates got enhanced for both bulk and brane emissions, yet we obtained a higher rate on the brane. It should be stressed that in the case of rotating black holes our results are modified due to superradiance. We also obtained analytic results in the case of large imaginary frequency.We derived expressions for grey-body factors in the bulk and on the brane for a Schwarzschild black hole in an arbitrary number of dimensions.

The special case of two extra dimensions with tension was seen to follow from a simple modification of the Hawking temperature.

We compared our analytic expressions in the two asymptotic regimes of low and high frequencies, respectively, with exact numerical solutions and discussed the range of intermediate frequencies where our analytic expressions are not accurate. The size of this intermediate range varies depending on the different parameters of the setup. Interestingly, this range is shifted toward high frequencies with increasing tension, indicating a wider range of validity of our analytic low-frequency expressions.

Chapter 5

Loop Amplitudes from Tree Amplitudes

As mentioned in the Introduction, starting from an insight by Witten (2004), Britto et al. (2005a) were able to construct a method for breaking down tree diagrams into simpler trees by placing a propagator inside the diagram on-shell. We first offer a quick derivation of the method, then investigate its applicability to 1-loop diagrams.

5.1 Outline of the BCFW Method

The BCFW relations can be easily derived with the help of Cauchy's integral theorem applied to tree-level amplitudes. We now outline a derivation of the method, and then look at possibility of going beyond tree-level applications.

Cauchy's theorem tells us that a closed-loop contour like the one figure (5.1) is given by:

$$\frac{1}{2i\pi}\oint_C dz \frac{\mathcal{A}(z)}{z} = 0 \tag{5.1}$$

where $\mathcal{A}(z)$ could have simple poles or branch cuts. If we treat $\mathcal{A}(z)$ as a tree-amplitude then clearly we do not have to worry about branch-cuts, and we only need to concentrate on poles, and the behavior of the integrand for large z. For loops,

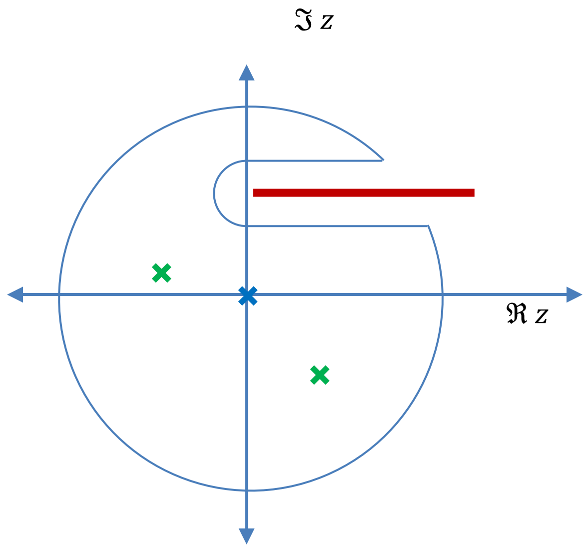

Figure 5.1: Generic contour for integrating a complexified 1-loop integral.

branch-cuts have to be included. In general we may write this:

$$\frac{1}{2i\pi}\oint_C dz \frac{\mathcal{A}(z)}{z} = \mathcal{A}(0) + \sum_{\text{poles}} \underset{z\to z_i}{\text{Res}} \frac{\mathcal{A}(z)}{z} + \underset{z\to\infty}{\text{Res}} \frac{\mathcal{A}(z)}{z} \quad \int_0^B \frac{dz}{z} \text{Disc}_B \mathcal{A}(z) \tag{5.2}$$

The last term accounts for the branch-cut discontinuity at loop level. The first term, $\mathcal{A}(0)$, is simply the original amplitude, which we would like to calculate, and the other two terms are residues at poles of $\mathcal{A}(z)$ and the residue at infinity. What BCFW did was introduce a complex variable z in the form of a complex shift on two external legs such that momentum conservation is preserved. Let the shift take the following form:

$$k_i \to k_i + zq, \qquad k_j \to k_j \quad zq \tag{5.3}$$

where k_i and k_j are different momenta, assumed both coming in here. Evidently, to preserve momentum conservation we must have:

$$q^2 = 0, \qquad k_{i,j} \cdot q = 0 \tag{5.4}$$

A suitable choice of q would therefore be a polarization vector. In this work we will consistently choose that to be ϵ_i. The resulting structure for the sum of residues is a sum of products of simpler trees:

$$\mathcal{A}(0) = \sum \mathcal{A}_L(z) \frac{1}{p^2 - m^2} \mathcal{A}_R(z) \tag{5.5}$$

where p is a propagator connecting two parts of the diagrams. What we have done is effectively 'cut' that propagator to form a split diagram with left $\mathcal{A}_L(z)$ and right $\mathcal{A}_R(z)$ trees.

So far this is the traditional application of the BCFW. Our work investigates the possibility of extending this to loop-level amplitudes. What we will do is investigate the integrand of the 1-loop rather than looking at the full integral, thereby side-stepping the issue of considering branch-cuts. Some initial investigations have already been carried out by Boels (2010). Our work offers a concrete example for gluons and shows that the integrand of 1-loop diagrams can be treated like trees, and is thus calculable via tree-level techniques.

5.2 Conventions and Assumptions

A massless vector boson in D dimensions possesses $D-2$ polarization states that can be represented by $D-2$ independent vectors ϵ^μ_λ transverse to the momentum k^μ, where $\lambda \in \{1, 2, \ldots, D-2\}$:

$$k_i \cdot \epsilon_i = 0 \tag{5.6}$$

In what follows we will not be concerned with polarization. Therefore, to simplify calculations, and without loss of generality, we will make specific choices of polarization vectors. The first is to choose null-polarization:

$$\epsilon^2 = 0 \tag{5.7}$$

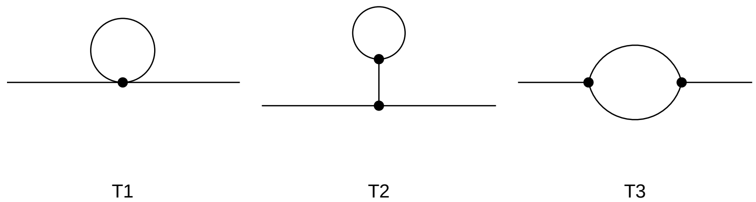

Figure 5.2: Diagrams contributing to $g \to g$ amplitude at one-loop.

Additional relations constraining polarization will be stated at the time of use.

The calculations of the next sections will employ Feynman rules written in the Feynman gauge for its simplicity ($\xi = 1$). These rules are shown in Appendix B.

5.3 Two-point One-Loop

The diagrams contributing to the 1-loop 2-gluon amplitude $\mathcal{A}_{g\to g}^{1-\text{loop}}$ are shown in fig. 5.2. In these diagrams we will take the left leg to be incoming and carrying momentum k_1, polarization ϵ_1 and color index a. The right leg will be outgoing, with momentum k_2, polarization ϵ_2^* and color index b. Clearly, from momentum conservation, incoming momentum k_1 is the same as outgoing momentum k_2; let us refer to either as k, which means that:

$$k_{1,2} \cdot \epsilon_1 = k_{1,2} \cdot \epsilon_2^* = 0 \tag{5.8}$$

$$\mathcal{A}_{g\to g}^{1-\text{loop}} = T_1 + T_2 + T_3 \tag{5.9}$$

Applying the Feynman rules, we find the following:

$$T_1 = \frac{9i\alpha_s}{4\pi^3}\delta^{ab}\epsilon_1 \cdot \epsilon_2^* \int \frac{d^D\ell}{\ell^2} \tag{5.10}$$

$$T_2 \propto f^{abc}f^{cdd} = 0 \tag{5.11}$$

$$T_3 = -\frac{3i\alpha_s}{8\pi^3}\delta^{ab}\int d^D\ell \frac{10\,(\ell\cdot\epsilon_1)\,(\ell\cdot\epsilon_2^*) + \left[\ell^2 + (\ell-k)^2\right]\epsilon_1\cdot\epsilon_2^*}{\ell^2(\ell-k)^2} \tag{5.12}$$

5.3.1 BCFW Shift

We will use the following shift:

$$k_1 \to k_1 + z\epsilon_1, \qquad k_2 \to k_2 + z\epsilon_1 \tag{5.13}$$

This shift doesn't conserve the relations found in (5.8), so that we need to shift ϵ_2^*:

$$\epsilon_2^* \to \epsilon_2^* - z\frac{\epsilon_1 \cdot \epsilon_2^*}{k_1^2}k_1 \tag{5.14}$$

We will consider only T_1 and T_3, since T_2 vanishes due to the anti-symmetry of the structure factor.

Our aim is to calculate contributions for large z. For the case of T_1 we see that only the external legs are shifted, so that the whole diagram survives when taking the limit $z \to \infty$, but as will be pointed out below that diagram vanishes, which means it does not contribute at infinity. As for T_3, according to figure (5.3), if we put the upper propagator on-shell the shifted integrand becomes:

$$I_3(z) = -\frac{15i\alpha_s}{4\pi^3}\delta^{ab}\frac{(\ell \cdot \epsilon_1)\left(\ell \cdot \epsilon_2^* - z\frac{\epsilon_1 \cdot \epsilon_2^*}{k_1^2}k_1 \cdot \ell\right)}{\ell^2\left[(\ell - k_1)^2 - 2z\ell \cdot \epsilon_1\right]} \tag{5.15}$$

which has a single pole at:

$$z_0 = \frac{(\ell - k_1)^2}{2\ell \cdot \epsilon_1} \tag{5.16}$$

Here is the residue at infinity:

$$\operatorname*{Res}_{z\to\infty} I_3 = -\frac{15i\alpha_s}{8\pi^3}\delta^{ab}\frac{\left(\frac{\epsilon_1 \cdot \epsilon_2^*}{k_1^2}k_1 \cdot \ell\right)}{\ell^2} \tag{5.17}$$

Because this has an odd power of loop momentum the integral of this would vanish.

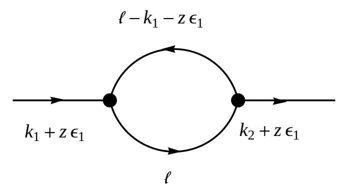

Figure 5.3: BCFW shift for 2-point 1-loop

5.3.2 Calculating the Diagrams

Looking at the three diagrams, we can readily see that the first two must vanish, and in fact so must the third. But, let us show this explicitly. For T_1, we see that the integral is calculated using (A.20) with $r = 0$ and $s = 1$:

$$\int \frac{d^D q}{(2\pi)^D} \frac{1}{(q^2 - \Delta)} = -\frac{i}{(4\pi)^{D/2}} \Gamma\left(1 - \frac{D}{2}\right)\left(\frac{1}{\Delta}\right)^{1-\frac{D}{2}} = \frac{i\Delta}{8(2\pi)^4 \varepsilon} + \mathcal{O}(\varepsilon) \tag{5.18}$$

Since $\Delta = m^2 = 0$, we see that

$$T_1 = 0 \tag{5.19}$$

In T_3 the expression between square brackets will not contribute because it can be reduced to the form (5.18), so that we only need to evaluate this:

$$T_3 = -\frac{15 i \alpha_s}{4\pi^3} \delta^{ab} \left(\epsilon_1\right)_\alpha \left(\epsilon_2^*\right)_\beta \int d^D \ell \frac{\ell^\alpha \ell^\beta}{\ell^2 \left(\ell - k\right)^2} \tag{5.20}$$

We can evaluate this by Feynman parameters followed by an application of (A.21). Using (A.26) first, we get:

$$\frac{1}{\ell^2 (\ell - k)^2} = \int_0^1 \frac{dx}{\left[x\ell^2 + (1-x)(\ell - k)^2\right]^2} \tag{5.21}$$

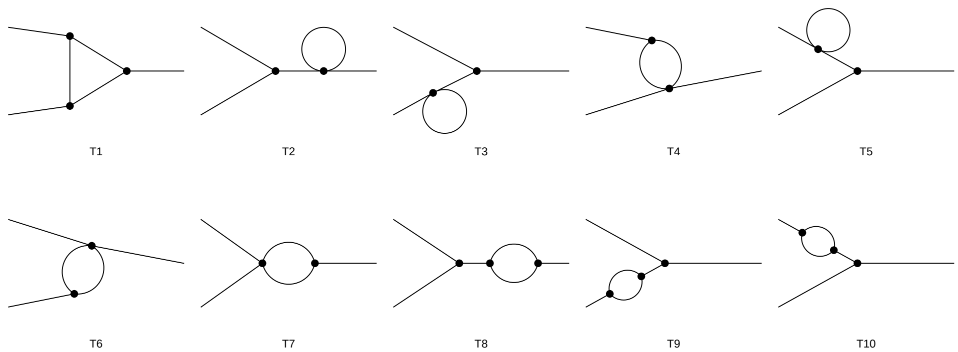

Figure 5.4: Diagrams contributing to $2g \to g$ amplitude at one-loop.

Let $\ell \to q + (1-x)k$, then:

$$\frac{1}{\ell^2(\ell-k)^2} = \int_0^1 \frac{dx}{\left[q^2 - \Delta\right]^2} \tag{5.22}$$

where $\Delta = 0$, which, in combination with an application of (A.21) shows T_3 vanishes:

$$T_3 \sim \int_0^1 dx \int d^D q \frac{q^\alpha q^\beta}{\left[q^2 - \Delta\right]^2} = \frac{i\Delta}{16\varepsilon} \tag{5.23}$$

5.4 Three-point One-Loop

Moving now to the 3-point functions, we see in this case that have two legs incoming, k_1 and k_2, and one outgoing, k_3, with correspondingly indexed polarization vectors and color indices a, b, and c, respectively. By momentum conservation we have:

$$k_3 = k_1 + k_2 \tag{5.24}$$

However, it is obvious that in such a case we cannot satisfy this if all legs are massless, and we must take one leg off-shell, which we choose to be the outgoing one, k_3. In doing so we are breaking gauge-invariance and we shall see that this will affect the final outcome below.

Let us further make the following convenient choice for polarization:

$$k_i \cdot \epsilon_j = 0, \qquad i \in \{1, 2\} \tag{5.25}$$

This implies that

$$k_3 \cdot \epsilon_i = 0, \qquad i \in \{1, 2\} \tag{5.26}$$

Dotting (5.24) with ϵ_3^* gives $0 = k_1 \cdot \epsilon_3^* + k_2 \cdot \epsilon_3^*$, and this would be satisfied if we choose ϵ_3^* to be:

$$\epsilon_3^* = a\,(k_1 - k_2) \tag{5.27}$$

for some constant a. From this we see that:

$$\epsilon_{1,2} \cdot \epsilon_3^* = 0 \tag{5.28}$$

We see from figure (5.4) that many diagrams immediately vanish. In particular, $\{T_2, T_3, T_5\}$ contain massless tadpoles that vanish, as demonstrated for T_1 in the 2-point case. Also, $\{T_9, T_{10}\}$ contain massless bubbles, which also vanish, as we've seen in T_3 for the 2-point case. As for $\{T_4, T_6, T_7\}$, their integrals reduce to ones similar to those containing bubbles, but they also vanish by anti-symmetry of structure factors. For instance, in the case of T_7 we have:

$$T_7 \sim (\epsilon_1 \cdot \epsilon_2)\, f^{aei} f^{bdi} \left(f^{cde} + f^{ced}\right) \int d^D \ell \frac{\ell \cdot \epsilon_3^*}{\ell^2\,(k_3 + \ell)^{\,2}} \tag{5.29}$$

The vanishing of all these diagrams was also established using `FormCalc`. Thus, we are only left with T_1 and T_8:

$$\mathcal{A}_{2g \to g}^{1-\text{loop}} = T_1 + T_8 \tag{5.30}$$

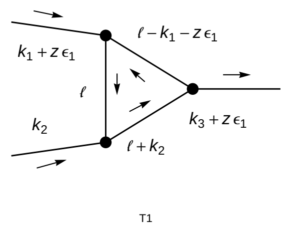

(a) Shifted T_1

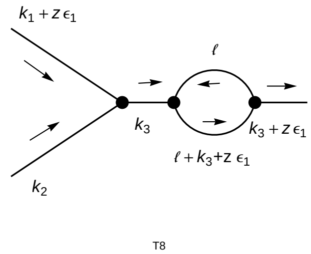

(b) Shifted T_8

Figure 5.5: BCFW shift of the non-vanishing diagrams in the 3-point case

Where

$$T_1 = \frac{3g_s^2}{16\pi^4} f^{abc} \int \frac{d^D\ell}{\ell^2\,(\ell-k_1)^{\,2}\,(\ell+k_2)^{\,2}} \left\{\epsilon_1\cdot\epsilon_2\left[k_1\cdot\epsilon_3^*\left(-k_1\cdot\ell+k_2\cdot\ell-3k_1\cdot k_2+3\ell^2\right)\right.\right.$$
$$\left.\left.-\ell\cdot\epsilon_3^*\left(-k_1\cdot\ell+k_2\cdot\ell-7k_1\cdot k_2+\ell^2\right)\right]+9\ell\cdot\epsilon_1\ell\cdot\epsilon_2\left(k_1\cdot\epsilon_3^*-\ell\cdot\epsilon_3^*\right)\right\} \tag{5.31}$$

and

$$\begin{aligned} T_8 = -\frac{3g_s^2 f^{abc}\,(\epsilon_1\cdot\epsilon_2)}{32\pi^4} \int d^D\ell \frac{1}{(k_1\cdot k_2)\,\ell^2\,(\ell+k_3)^{\,2}} \\ \times\left\{k_1\cdot\epsilon_3^*\left[2\ell^2+2\,(k_3\cdot\ell)\right]+5\ell\cdot\epsilon_3^*\,(k_1\cdot\ell-k_2\cdot\ell)+10k_1\cdot k_2k_1\cdot\epsilon_3^*\right\} \end{aligned} \tag{5.32}$$

5.4.1 BCFW Shift

We would like to shift k_1 and k_3 as in figure (5.5), so that:

$$k_1 \to k_1 + z\epsilon_1 \qquad k_3 \to k_3 + z\epsilon_1 \tag{5.33}$$

All of the previous relations (5.25-5.28) are still valid, and we do not need to shift ϵ_3^* like we did in the 2-point case. Applying the shift to the first diagram we get:

$$
\begin{aligned}
I_1 = {} & \frac{3g_s^2}{16\pi^4} f^{abc} \frac{1}{\ell^2 \left[(\ell - k_1)^{\,2} - 2z\ell\cdot\epsilon_1 \right] (\ell + k_2)^{\,2}} \\
& \times \left\{ \epsilon_1 \cdot \epsilon_2 \left[k_1 \cdot \epsilon_3^* \left(-k_1 \cdot \ell - z\ell \cdot \epsilon_1 + k_2 \cdot \ell - 3k_1 \cdot k_2 + 3\ell^2 \right) \right.\right. \\
& \left.\left. - \ell \cdot \epsilon_3^* \left(-k_1 \cdot \ell - z\ell\cdot\epsilon_1 + k_2 \cdot \ell - 7k_1 \cdot k_2 + \ell^2 \right) \right] + 9\ell\cdot\epsilon_1 \ell\cdot\epsilon_2 \left(k_1 \cdot \epsilon_3^* - \ell \cdot \epsilon_3^* \right) \right\}
\end{aligned} \tag{5.34}
$$

which has a single pole at $(\ell - k_1)^{\,2} / (2\ell \cdot \epsilon_1)$. The residue of this expression at infinity takes the following form:

$$
\operatorname*{Res}_{z\to\infty} I_1 = \frac{3g_s^3 f^{abc}}{32\pi^4} \left[\frac{\ell\cdot\epsilon_3^*}{\ell^2 \left(2k_2\cdot\ell + \ell^2\right)} - 9k_1\cdot\epsilon_3^* \frac{1}{\ell^2\left(2k_2\cdot\ell + \ell^2\right)} \right] \epsilon_1 \cdot \epsilon_2 \tag{5.35}
$$

We can Feynman-parametrize this with by setting $\ell \to q + (x-1)k_2$, which gives us the following integral:

$$
\operatorname*{Res}_{z\to\infty} T_1 = \frac{3g_s^3 f^{abc}}{32\pi^4} \epsilon_1 \cdot \epsilon_2 \int dx \left[(x-1)k_2 \cdot \epsilon_3^* - 9k_1 \cdot \epsilon_3^* \right] \int \frac{d^d q}{\left(q^2 - \Delta\right)^2} \tag{5.36}
$$

where $\Delta = x(x-1)k_2^2 \to 0$. Then using eq. (A.20) and expanding around $\varepsilon = 0$, we get:

$$
\operatorname*{Res}_{z\to\infty} T_1 = -17 \frac{3ig_s^3 f^{abc}}{32\pi^2} k_1 \cdot \epsilon_3^* \epsilon_1 \cdot \epsilon_2 \left[\frac{1}{\varepsilon} - \frac{1}{2}\left(\gamma_E + \ln\pi\right) + \mathcal{O}\left(\varepsilon^1\right) \right], \tag{5.37}
$$

which is a clearly non-vanishing result. Let us now turn our attention to T_8 using the same shift:

$$
\begin{aligned}
T_8 = {} & -\frac{3g_s^2 f^{abc} \left(\epsilon_1\cdot\epsilon_2\right)}{32\pi^4 \left(k_1 \cdot k_2\right)} \int d^D\ell \frac{1}{\ell^2 \left[(\ell + k_3)^{\,2} + 2z\ell\cdot\epsilon_1 \right]} \left\{ 10k_1\cdot k_2 k_1 \cdot \epsilon_3^* \right. \\
& \left. + k_1 \cdot \epsilon_3^* \left[2\ell^2 + 2\left(k_3 \cdot \ell + z\ell\cdot\epsilon_1\right) \right] + 5\ell\cdot\epsilon_3^* \left(k_1\cdot\ell + z\ell\cdot\epsilon_1 - k_2\cdot\ell\right) \right\}
\end{aligned} \tag{5.38}
$$

which has a single pole at $z_0 = -(\ell + k_3)^{\,2} / 2\ell\cdot\epsilon_1$. At infinity we have:

$$
\begin{aligned}
\operatorname*{Res}_{z\to\infty} I_8 = {} & -\frac{3g_s^3 f^{abc}\left(\epsilon_1\cdot\epsilon_2\right)}{32\pi^4} \\
& \times \frac{k_1\cdot\epsilon_3^* \left(2\ell^2 + 2\left(k_3\cdot\ell\right)\right) + 5\ell\cdot\epsilon_3^*\left(k_1\cdot\ell - k_2\cdot\ell\right) + 10k_1\cdot k_2 k_1\cdot\epsilon_3^*}{\left(k_1\cdot k_2\right)\ell^2\left(\ell + k_3\right)^{\,2}}
\end{aligned} \tag{5.39}
$$

Then using shifting momentum to $\ell \to q + (x-1)k_3$ and taking $\Delta = x(x-1)k_3^2$, we get the Feynman-parametrized expression:

$$\operatorname*{Res}_{z\to\infty} I_8 = -\frac{3g_s^3 f^{abc}\,(\epsilon_1\cdot\epsilon_2)}{32\pi^4\,(k_1\cdot k_2)}\frac{1}{(q^2-\Delta)^2}\left\{2k_1\cdot\epsilon_3^*\left[q^2+q\cdot k_3(2x-1)\right.\right.$$
$$\left.\left.+k_3^2x(x-1)\right]+5q\cdot\epsilon_3^*\,(k_1-k_2)\cdot q+10k_1\cdot k_2k_1\cdot\epsilon_3^*\right\} \tag{5.40}$$

Upon integrating as before, then expanding around small ε we find

$$\operatorname*{Res}_{z\to\infty} T_8 = -\frac{ig_s^3}{16\pi^2}f^{abc}\,(\epsilon_1\cdot\epsilon_2)\,(k_1\cdot\epsilon_3^*)$$
$$\times\left\{\frac{19}{\varepsilon}+\frac{1}{6}\left[104-57\gamma_E+57\ln\left(-\frac{1}{\pi k_3^2}\right)\right]+\mathcal{O}\left(\varepsilon^1\right)\right\} \tag{5.41}$$

Like T_1, this is divergent.

Now, when checking for residues at infinity we are interested in the behavior of the entire amplitude rather than that of individual diagrams. Therefore, we are supposed to look at the combined residue, which clearly is still divergent, as it goes like $1/\varepsilon$. By itself, this result does not necessarily say that we cannot apply the BCFW shift, and the reason for this has to do with the fact that by putting one leg off-shell the diagrams are now gauge-dependent, so that the divergence we are seeing is in fact inherited from the diagrams before the complex shift:

$$\text{Divergence}\,(T_1) = \frac{39ig_s^3f^{abc}}{32\pi^2}\epsilon_1\cdot\epsilon_2\epsilon_3\cdot k_1\frac{1}{\varepsilon} \tag{5.42}$$

and

$$\text{Divergence}\,(T_8) = \frac{19ig_s^3f^{abc}}{32\pi^2}\frac{\epsilon_1\cdot\epsilon_2\epsilon_3^*\cdot k_1}{k_1\cdot k_2}\frac{1}{\varepsilon} \tag{5.43}$$

Some other gauges would not exhibit this behavior. For example, the background-field gauge (see for example Abbott (1982); Bern and Chalmers (1995)), has the property of giving gauge-invariant expressions with respect to the external legs. In al Binni et al. (2011) the calculation was done using a combination of the Background-field gauge and the Gervais and Neveu (1972) gauge. The two resulting diagrams are

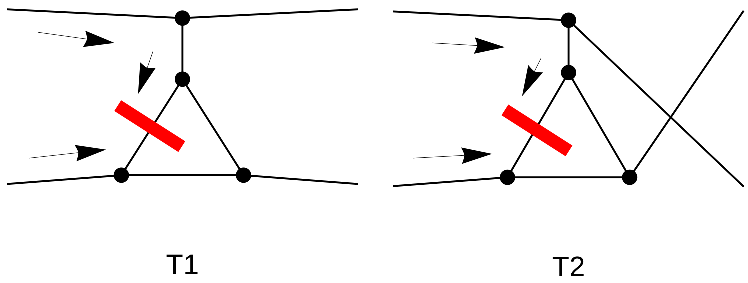

Figure 5.6: Non-vanishing triangle diagrams contributing to $2g \to 2g$ 1-loop amplitude. Arrows show the direction of flow of $z\epsilon_1$.

individually divergent, but the combination is finite. Further, the residue at infinity of each diagram vanishes.

5.5 Four-point One-Loop

For the 4-point case we shall divide the legs as two incoming and two outgoing. The full topology list contains 99 diagrams, or 74 if we exclude tadpoles. These diagrams are shown in Appendix B. Of these only 5 are non-vanishing, and they are displayed in figures (5.6) and (5.7). The fact that the others vanish was established using `FormCalc`, but looking at these diagrams it is not difficult to show that they vanish based on arguments like those used for the 2- and 3-point cases above. The amplitude is then made up of the remaining 5 diagrams:

$$\mathcal{A}_{2g\to 2g}^{1-\text{loop}} = T_8 + T_{10} + T_{13} + T_{14} + T_{15} \tag{5.44}$$

We will make now some assumptions about polarization that would simplify shifted expressions later on. First, we assume that

$$k_i \cdot \epsilon_j = 0, \qquad i \in \{1, 2\} \tag{5.45}$$

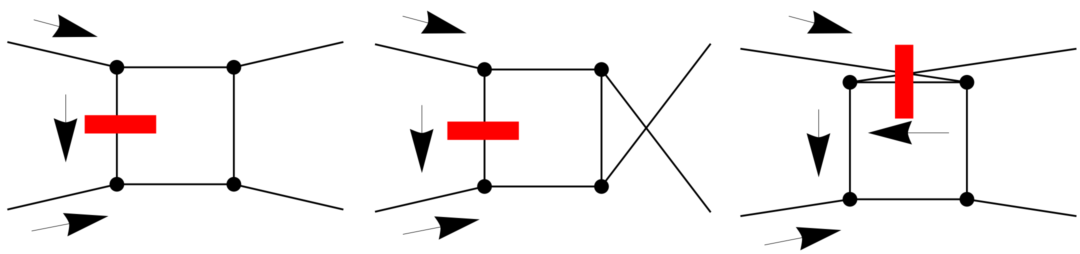

Figure 5.7: Non-vanishing diagrams contributing to $2g \to 2g$ 1-loop amplitude. Arrows show the direction of flow of $z\epsilon_1$.

And we can always write the other two polarizations in terms of k_1 and ϵ_1:

$$\epsilon_i^* = a_i k_1 + b_i \epsilon_1, \qquad i \in \{3, 4\} \tag{5.46}$$

or by multiplying by k_i and rearranging:

$$\epsilon_i^* = b_i \left(\epsilon_1 - \frac{\epsilon_1 \cdot k_i}{k_1 \cdot k_i} k_1 \right), \qquad i \in \{3, 4\} \tag{5.47}$$

And finally:

$$\epsilon_1 \cdot \epsilon_2 = 0 \tag{5.48}$$

T_8 and T_{10} are related by simple transformations, and so are T_{13}, T_{14} and T_{15}, which would facilitate things. So, let us start by looking at T_8:

$$T_8 = \int d^D \ell \frac{3 i g_s^4 f^{bce} f^{ade} k_3 \cdot \epsilon_1}{16 \pi^4 k_2 \cdot k_4 \ell^2 \left(\ell - k_2\right)^2 \left(\ell - k_4\right)^2} \left[-8 k_2 \cdot \epsilon_4^* \left(\ell \cdot \epsilon_2 k_2 \cdot \epsilon_3^* + k_3 \cdot \epsilon_2 \ell \cdot \epsilon_3^* \right) \right.$$
$$\left. + \ell \cdot \epsilon_4^* \left(k_2 \cdot \epsilon_3^* \left(8 k_3 \cdot \epsilon_2 + 9 \ell \cdot \epsilon_2 \right) - 9 \ell \cdot \epsilon_2 \ell \cdot \epsilon_3^* \right) \right] \tag{5.49}$$

For T_{10} we switch k_3, ϵ_3^* with k_4, ϵ_4^*:

$$T_{10} = \int d^d\ell \frac{-3ig_s^4 k_3 \cdot \epsilon_1 f^{bde} f^{ace}}{16\pi^4 k_2 \cdot k_3 \ell^2 \left(\ell - k_2\right)^2 \left(\ell - k_3\right)^2} \left\{-8k_2 \cdot \epsilon_3^* \left(\ell \cdot \epsilon_2 k_2 \cdot \epsilon_4^* + k_4 \cdot \epsilon_2 \ell \cdot \epsilon_4^*\right)\right.$$
$$\left.\ell \cdot \epsilon_3^* \left[k_2 \cdot \epsilon_4^* \left(8k_4 \cdot \epsilon_2 + 9\ell \cdot \epsilon_2\right) - 9\ell \cdot \epsilon_2 \ell \cdot \epsilon_4^*\right]\right\} \tag{5.50}$$

And here are the other three:

$$T_{13} = \int d^D\ell \frac{-ig_s^4 f^{aeh} f^{bei} f^{chj} f^{dij}}{8\pi^4 \ell^2 \left(\ell + k_1\right)^2 \left(\ell + k_2\right)^2 \left(\ell + k_2 - k_4\right)^2} \ell \cdot \epsilon_1 \left\{16\ell \cdot \epsilon_2 k_2 \cdot \epsilon_3^* k_2 \cdot \epsilon_4^*\right.$$
$$\left.+17\ell \cdot \epsilon_3^* \ell \cdot \epsilon_2 \left(k_2 \cdot \epsilon_4^* + \ell \cdot \epsilon_4^*\right) + 16k_3 \cdot \epsilon_2 \left(k_2 \cdot \epsilon_4^* \ell \cdot \epsilon_3^* - k_2 \cdot \epsilon_3^* \ell \cdot \epsilon_4^*\right)\right\} \tag{5.51}$$

$$T_{14} = \int d^D\ell \frac{-ig_s^4 f^{aeh} f^{bei} f^{cij} f^{dhj}}{8\pi^4 \ell^2 \left(\ell + k_1\right)^2 \left(\ell + k_2\right)^2 \left(\ell + k_2 - k_3\right)^2} \ell \cdot \epsilon_1 \left\{16\ell \cdot \epsilon_2 k_2 \cdot \epsilon_3^* k_2 \cdot \epsilon_4^*\right.$$
$$\left.+17\ell \cdot \epsilon_4^* \ell \cdot \epsilon_2 \left(k_2 \cdot \epsilon_3^* + \ell \cdot \epsilon_3^*\right) + 16k_3 \cdot \epsilon_2 \left(k_2 \cdot \epsilon_4^* \ell \cdot \epsilon_3^* - k_2 \cdot \epsilon_3^* \ell \cdot \epsilon_4^*\right)\right\} \tag{5.52}$$

$$T_{15} = \int d^D\ell \frac{-ig_s^4 f^{aeh} f^{bij} f^{cei} f^{dhj}}{8\pi^4 \ell^2 \left(\ell + k_1\right)^2 \left(\ell - k_3\right)^2 \left(\ell + k_2 - k_3\right)^2} \ell \cdot \epsilon_1 \left\{16\ell \cdot \epsilon_2 k_2 \cdot \epsilon_3^* k_2 \cdot \epsilon_4^*\right.$$
$$\left.+17\ell \cdot \epsilon_3^* \ell \cdot \epsilon_4^* \left(\ell \cdot \epsilon_2 - k_3 \cdot \epsilon_2\right) + 16k_3 \cdot \epsilon_2 \left(k_2 \cdot \epsilon_4^* \ell \cdot \epsilon_3^* - k_2 \cdot \epsilon_3^* \ell \cdot \epsilon_4^*\right)\right\} \tag{5.53}$$

5.5.1 BCFW Shift

We would like to shift these expressions according to the following rules:

$$k_1 \to k_1 + z\epsilon_1 \qquad k_2 \to k_2 - z\epsilon_1 \tag{5.54}$$

Referring to figures (5.6) and (5.7), we can see that this shift cuts one propagator in each diagram, and each such cut gives a simple pole. However for T_8 and T_{10} we also get poles from the vertical neck above the triangle resulting in two poles in those two cases. Table (5.1) lists the diagrams and their poles At this point comes the role of the polarization choice we made. If we look at the shifted numerators we see that nothing is changed under the shift. Therefore we may write the integrand for any of

Table 5.1: Poles of BCFW-shifted 4-point diagrams.

Diagram	Poles
T_8	$z_1 = \frac{k_2 \cdot k_4}{\epsilon_1 \cdot k_4},\ z_2 = -\frac{(\ell - k_2)^2}{2\ell \cdot \epsilon_1}$
T_{10}	$z_1 = \frac{k_3 \cdot k_4}{\epsilon_1 \cdot k_3},\ z_2 = -\frac{(\ell - k_2)^2}{2\ell \cdot \epsilon_1}$
T_{13}	$z_1 = -\frac{\ell^2}{2\ell \cdot \epsilon_1}$
T_{14}	$z_1 = -\frac{\ell^2}{2\ell \cdot \epsilon_1}$
T_{15}	$z_1 = -\frac{\ell^2}{2\ell \cdot \epsilon_1}$

the diagrams in this general form:

$$I_i(z) = \frac{\mathcal{N}_i}{(z - z_1)\,(z - z_2)^{\,s_i}}, \qquad i \in \{8, 10, 13, 14, 15\} \tag{5.55}$$

where $\mathcal{N}_i$ is independent of z, and s_i is 1 for $i = 8$ and $i = 10$ and zero for the rest. The residue at infinity can then be readily found:

$$\operatorname*{Res}_{z \to \infty} I_i(z) = \lim_{z \to \infty} \frac{\mathcal{N}_i}{z^{1+s_i}} = 0 \tag{5.56}$$

This result means that for the 4-point amplitude the residues at the poles correspond to the diagrams themselves:

$$\operatorname*{Res}_{z \to z_1} \frac{(z - z_1)\, I_i(z)}{z} + \operatorname*{Res}_{z \to z_2} \frac{(z - z_2)\, I_i(z)}{z} = -I_i(0) \tag{5.57}$$

5.5.2 Calculating the Diagrams

For completeness, we now calculate two representative diagrams below. We start with T_8 by shifting the internal momentum $\ell \to q + (xk_4 + yk_2)\, p$ to prepare for Feynman parametrization, which gives us:

$$T_8 = \frac{27 i g_s^4}{16\pi^4} f^{bce} f^{ade} \frac{k_3 \cdot \epsilon_1 k_3 \cdot \epsilon_2 k_2 \cdot \epsilon_3^* k_2 \cdot \epsilon_4^*}{k_2 \cdot k_4} \int_0^1 dx \int_0^{1-x} dy \int d^D q \frac{xy\ (x + y - 1)}{(q^2 - 2xy k_2 \cdot k_4)^{\,3}} \tag{5.58}$$

Upon integration, we get a finite result:

$$T_8 = -\frac{9ig_s^4}{64\pi^2} f^{bce} f^{ade} \frac{k_3 \cdot \epsilon_1 k_3 \cdot \epsilon_2 k_2 \cdot \epsilon_3^* k_2 \cdot \epsilon_4^*}{(k_2 \cdot k_4)^{\,2}} \tag{5.59}$$

The other one will be T_{13}. The momentum shift this time will be

$$\ell \to x k_4 - y k_1 - (x+z) k_2$$

After some simplifications, we end up with this integral (see section C.2.3):

$$T_{13} = \frac{AF^{abcd}}{4} k_3 \cdot \epsilon_1 k_3 \cdot \epsilon_2 k_2 \cdot \epsilon_3^* k_2 \cdot \epsilon_4^* \int dx\, dy\, dz\, d^D q \frac{x^2 z(x+z-1)}{(q^2-\Delta)^4} \tag{5.60}$$

where

$$\Delta = 2x(1-x-z) k_2 \cdot k_4 + 2y(x+z) k_1 \cdot k_2 - 2xy k_1 \cdot k_4 \tag{5.61a}$$

$$A = -\frac{17ig_s^4}{288\pi^2} \tag{5.61b}$$

$$F^{abcd} = f^{aeh} f^{bei} f^{chj} f^{dij} \tag{5.61c}$$

After integration and cleaning up, we get this final result:

$$T_{13} = AF^{abcd} \frac{4t^2 - s^2 - 4st \log\left(\frac{s}{-2t}\right)}{(s+2t)^3 t} \left(k_3 \cdot \epsilon_1 k_3 \cdot \epsilon_2 k_2 \cdot \epsilon_3^* k_2 \cdot \epsilon_4^*\right) \tag{5.62}$$

where $s = 2k_1 \cdot k_2$ and $t = -2k_1 \cdot k_3$ are Mandelstam variables.

5.6 Beyond 4-point, Beyond 1-loop

At this point, the natural question to ask is whether we can generalize this to an arbitrary number of external legs n. The answer is yes. Looking at the result of the 4-point, we have seen that when we did the BCFW shift only the denominators experienced the shift, while the numerators stayed intact. We can understand the reason for this, and the way to generalize the result, by looking at the structure of a diagram in terms of its vertices and propagators and their eventual contraction with polarization vectors, and for concreteness we will refer to the Feynman rules in Appendix (B).

The two main ingredients of this are our assumptions about polarization, namely, that all vectors are writable as linear combinations of k_1 and ϵ_1, and that $k_i \cdot \epsilon_j = 0$ for $i, j \in \{1, 2\}$. Which implies that for n-point diagrams, with $n \geq 4$, the product of any two polarizations vanishes. Let us note that in a given diagram, a 3-vertex contributes one power of momentum, but a 4-vertex contributes none. In terms of Lorentz indices an n-point all-gluon diagram that has no 4-vertices is made up of contraction of a product of n polarization vectors with linear combinations of n momenta, which are $n-1$ external momenta and one internal. A fully contracted term would be made up of a product of n dot products between these $2n$ vectors. Because of our choice of polarization one can see that some product will not appear, namely products of the form $\ell \cdot k_i$. To show that, suppose such a product is present. It would have to be multiplied by $n-1$ other dot products, and these would be made up of the n polarization vectors and $n-2$ momenta, some momenta possibly repeating. In this we must have at least one dot product of the form $\epsilon_i \cdot \epsilon_2$, which means that the whole term vanishes. Only terms of the form $\ell \cdot k_i$ would make the z appear in the numerator when k_i is one of the two shifted momenta, and we see that such terms cannot appear. In fact the numerator can contain only terms made up of products of dot products of the form $\epsilon_i \cdot p$, where p is a momentum vector. We can see this in the expressions above for the 4-point diagrams. Moreover, we notice that this choice of polarization eliminates the appearance of 4-vertices completely for similar reasons.

The implication of this for our investigation is that when we shift two external legs, which do not necessarily have to be adjacent on the diagrams, and impose the aforementioned conditions for polarization, we end up with a complex function that has the z appearing only in the denominator, forming simple poles. The residue at infinity for such a function is clearly zero, so that the condition for BCFW is met for all n-point diagrams.

Chapter 6

Conclusions and Outlook

With the LHC now in operation, the next few years could bring about interesting breakthroughs in our understanding of high-energy physics. While much progress has happened over the last few decades in putting forth potential models of physics beyond the Standard Model and in improving precision through new computational techniques, there is still much to be done. On the hand, more theoretical work needs to be done in two respects; the first is refining predictions of new theories and understanding observational implications, the other is going to more precise predictions, which is done by improving computational methods. On the other hand, without the input from experiment that would start the usual cycle of theory-experiment dialectic, little progress can only be made. The LHC, its upgrades, and subsequent projects (such as the International Linear Collider) are efforts to get that cycle going.

The present work investigated some theoretical and computational ideas relevant to that search for new physics going on at the LHC. The possibility of experimentally testing many of the theories that go beyond the Standard Model is a realistic one now. Detecting black holes in high-energy collisions, if observed, would offer for a first time the opportunity of probing the realm of quantum gravity and would bring with it the resolution of some the important puzzles of 20th century physics. This means we need to be well-prepared with realistic predictions to interpret the possible observations.

In the study of the quasi-normal frequencies and the creation and evaporation of mini black-holes, a main prediction of brane-world models, brane tension has often been neglected, and while predictions are not radically modified by including it, the fact that we are trying to observe something we have never observed before makes it imperative to strive to be as realistic and accurate as possible. As a first approximation, one can neglect brane tension for black-holes of a large mass, but as a point of principle, tension represents the defining feature of branes in the context of String Theory, making it an essential factor to be considered. However, finding solutions of the Einstein equations in the presence of brane tension is quite challenging. In the special case of 6-dimensions (a codimension-2 setup) an exact solution has been found by Kaloper and Kiley (2006) for a non-rotating black-hole and then extended to describe the rotating case by Kiley (2007). These solutions offer an opportunity to study the effect of brane tension on black-hole observables. The two main observables being quasi-normal modes and Hawking radiation. The first part of the present work represents a study of these two phenomena in the presence of brane tension for a non-rotating black-hole localized on a codimension-2 brane.

In chapter 2 we reviewed some features of the codimension-2 solution, where the problem of including brane tension is solved owing to the fact that in that special case, vacuum energy on the brane is off-loaded into the bulk cusping it into a cone centered at the brane, leaving the brane flat, and thereby resulting in a black-hole solution that looks like a modified Schwarzschild solution. We provided an exact solution for the angular eigenvalue problem that results in studying the propagation of Standard Model fields in the vicinity of such a black-hole (al Binni and Siopsis (2007)). The resulting eigenvalues are modified regular sphere solutions, where a dependence on quantum number m appears in the case of a non-vanishing tension in terms of the deficit angle parameter b. We then proceeded to verify our result by reproducing the previously known numerical results of Dai et al. (2007) and the perturbative approximation of Chen et al. (2007).

In chapter 3 we used our solution of the eigenvalue problem to study quasi-normal frequencies of a black-hole localized on a codimension-2 brane, where we used 3rd order WKB approximation to find frequencies for low-lying quasi-normal modes, where we examined the effect of tension on these frequencies (al Binni and Siopsis (2007)). At low tension we recovered the known results of spherical geometrically. For high tension ($b \to 0$), we found that the imaginary part of the frequency, related to damping, went to zero as $b^{1/3}$, while the oscillatory part exhibited behavior reminiscent of the Zeeman effect, where the $m = 0$ case vanishes for high, but all other m's diverged as $b^{-2/3}$.

Next, in Chapter 4, we studies the effects of tension on Hawking radiation emission from a black-hole on a codimension-2 brane, where we calculated grey-body factors for low-frequency emissions as well as high-frequency, and we looked at various types of field perturbations (see al Binni and Siopsis (2009)). The results get modified in two main ways; through the enhancement of horizon radius with tension, resulting in enhanced emission, and the increase in angular eigenvalues with tension. Combined these two effects result in an amplification of emission on the brane and in the bulk, but more on the brane, which is an attractive prospect in terms of experimental searches for extra-dimensional black holes at the LHC. We compared our analytical results with numerical solutions, and we also discussed the intermediate frequency regime, where our analytic results are not accurate. We noted that the size of that intermediate range varies with tension, so that it gets shifted towards high-frequencies with increasing tension, indicating that a wider range of validity for the low-frequency results.

Chapter 5 was the second part of this work, and it studied a computational theme, where we explored the question of extending the BCFW method beyond tree-level to 1-loop, and we did so by establishing the validity of applying the BCFW to integrands of n-gluon 1-loop amplitudes. We demonstrated that by doing a BCFW shift on the external legs, the residue at infinity of the complexified integrand vanishes, thus demonstrating that diagrams making up these 1-loop amplitudes can be described purely in terms of the poles of the integrands. Doing the complex shift puts on propagator on-shell, effectively 'cutting' that propagator and turning the integrand into a form that can be treated as a tree-level diagram.

There are various possible directions to pursue starting from the results of our work. For the case of studying black-holes on branes, a next logical step is to try to go beyond the codimension-2 model and to generalize to other geometries and to other codimensions. The codimension-2 case is a special one in terms of simplification because of its self-tuning mechanism. In other extra-dimensional cases things are considerably more difficult, but not impossible, especially if one considers perturbative solutions. Other geometries also present interesting challenges, specifically, it would be interesting to consider black holes in non-asymptotically flat geometries, such as in the work started by Karasik et al. (2005). Some promising directions in exploring codimension-1 already exist, as we already know a perturbative solution by Middleton and Siopsis (2005) in the DGP model, and that solution could accommodate the inclusion of brane-tension. As far as detection goes, like other models of Beyond the Standard Model physics, simulation of events in detectors provide and invaluable aid in interpreting and understanding real results. Black-hole event generators are already available, starting with `CHARYBDIS`, introduced in Harris et al. (2003), simulates production and decay of black-holes, but does not include the effects of tension. More recently Dai et al. (2008) developed another black-hole event generator called `BlackMax` that does include the effects of tension, but only in 6-dimensions. Getting solutions in other codimensions should enhance the power of such simulators.

As for the BCFW method. By themselves, our results are a first step towards implementing the BCFW with all its simplifications at loop level, something that has not been done yet. We have seen that we now have the guarantee that we can safely treat 1-loop integrands as tree diagrams, and apply the BCFW to calculate those trees, and the BCFW has demonstrated great efficiency in doing such calculations.

It would also be of great benefit to go beyond 1-loop towards higher loop levels. At 2-loops we would like to reduce the integrands to 1-loop by cutting a propagator and putting it on-shell. Such a technique would be very useful in NNLO calculations at the LHC, but would also be relevant to calculations of perturbative quantum gravity.

Bibliography

Bibliography

Abbott, L. F. (1982). Introduction to the background field method. *Acta Physica Polonica*, B13(1-2):33–50. 66

Abdalla, E., Cuadros-Melgar, B., Pavan, A. B., and Molina, C. (2006). Stability and thermodynamics of brane black holes. *Nuclear Physics B*, 752:40. `arXiv:1103.1848v2 [hep-th]`. 18

al Binni, U. A., Kharel, S., and Siopsis, G. (2011). Gauge theory loop amplitudes from tree amplitudes. *To appear soon*. 66

al Binni, U. A. and Siopsis, G. (2007). Quasinormal modes of a black hole localized on a codimension-two brane of finite tension. *Physical Review D*, 76(10):104031. `arXiv:0708.3363`. 14, 74, 75

al Binni, U. A. and Siopsis, G. (2009). Particle emission from a black hole on a tense codimension-2 brane. *Physical Review D*, 79(8):084041. `arXiv:0902.2194`. 11, 75

Andersson, N. and Howls, C. (2004). The asymptotic quasinormal mode spectrum of non-rotating black holes. *Classical and Quantum Gravity*, 21:1623. `arXiv:gr-qc/0307020`. 40, 43

Antoniadis, I., Arkani-Hamed, N., Dimopoulos, S., and Dvali, G. R. (1998). New dimensions at a millimeter to a fermi and superstrings at a tev. *Physics Letters B*, 436:257. `arXiv:hep-ph/9804398`. 4

Argyres, P. C., Dimopoulos, S., and March-Russell, J. (1998). Black holes and sub-millimeter dimensions. *Physics Letters B*, 441:96. arXiv:hep-th/9808138. 18

Arkani-Hamed, N., Dimopoulos, S., and Dvali, G. R. (1998). The hierarchy problem and new dimensions at a millimeter. *Physics Letters B*, 429:263. arXiv:hep-ph/9803315. 4

Arkani-Hamed, N., Dimopoulos, S., and Dvali, G. R. (1999). Phenomenology, astrophysics and cosmology of theories with sub-millimeter dimensions and tev scale quantum gravity. *Physical Review D*, 59:086004. arXiv:hep-ph/9807344. 4

Ashtekar, A. and Lewandowski, J. (1997). Quantum theory of gravity i: Area operators. *Classical and Quantum Gravity*, 14:A55. arXiv:gr-qc/9602046. 18

Banks, T. and Fischler, W. (1999). A model for high energy scattering in quantum gravity. arXiv:hep-th/9906038. 18

Barbero, J. F. (1995). Real ashtekar variables for lorentzian signature space-times. *Physical Review D*, 51:5507. arXiv:gr-qc/9410014. 17

Bern, Z. (2002). Perturbative quantum gravity and its relation to gauge theory. *Living Reviews in Relativity*, 5(5):57. arXiv:gr-qc/0206071. 8

Bern, Z., Carrasco, J. J., Dixon, L. J., Johansson, H., and Roiban, R. (2011). Amplitudes and Ultraviolet Behavior of N=8 Supergravity. arXiv:1103.1848v2. 8

Bern, Z., Carrasco, J. J. M., and Johansson, H. (2010a). Perturbative Quantum Gravity as a Double Copy of Gauge Theory. *Physical Review Letters*, 105:061602. arXiv:1004.0476v2. 8

Bern, Z., Carrasco, J. J. M., and Johansson, H. (2010b). The Structure of Multiloop Amplitudes in Gauge and Gravity Theories. *Nucl. Phys. Proc. Suppl.*, 205-206:54–60. arXiv:1007.4297v1. 8

Bern, Z. and Chalmers, G. (1995). Factorization in one-loop gauge theory. *Nuclear Physics B*, 447:465–518. arXiv:hep-ph/9503236. 66

Bern, Z., Dennen, T., Huang, Y.-t., and Kiermaier, M. (2010c). Gravity as the square of gauge theory. *Physical Review D*, 82(065003):17. arXiv:1004.0693. 8

Bern, Z., Dixon, L. J., Dunbar, D. C., and Kosower, D. A. (1994). One-loop n-point gauge theory amplitudes, unitarity and collinear limits. *Nuclear Physics B*, 425:217–260. arXiv:hep-ph/9403226. 5

Bern, Z., Dixon, L. J., Dunbar, D. C., and Kosower, D. A. (1995). Fusing gauge theory tree amplitudes into loop amplitudes. *Nuclear Physics B*, 425:59–101. arXiv:hep-ph/9409265. 5

Bern, Z., Dixon, L. J., and Kosower, D. A. (2007). On-shell methods in perturbative qcd. *Annals of Physics*, 322(7):1587 – 1634. July 2007 Special Issue, arXiv:0704.2798v2. 5

Berti, E., Kokkotas, K. D., and Papantonopoulos, E. (2003). Stability of five-dimensional rotating black holes projected on the brane. *Physical Review D*, 68:064020. arXiv:gr-qc/0306106v2. 18

Boels, R. (2010). On bcfw shifts of integrands and integrals. *Journal of High Energy Physics*, 2010(11):1–43. arXiv:1008.3101. 58

Britto, R. (2010). Loop amplitudes in gauge theories: modern analytic approaches. arXiv:1012.4493v2 [hep-th]. 7

Britto, R., Cachazo, F., and Feng, B. (2005a). New Recursion Relations for Tree Amplitudes of Gluons. *Nucl. Phys.*, B715:499–522. arXiv:hep-th/0412308. 7, 56

Britto, R., Cachazo, F., Feng, B., and Witten, E. (2005b). Direct Proof Of Tree-Level Recursion Relation In Yang-Mills Theory. *Physical Review Letters*, 94:181602. arXiv:hep-th/0501052. 7

Cardoso, V., Cavaglia, M., and Gualtieri, L. (2006a). Black hole particle emission in higher-dimensional spacetimes. *Physical Review Letters*, 96:071301. Erratum-ibid. 96 (2006) 219902, `arXiv:hep-th/0512002v3`. 12, 33

Cardoso, V., Cavaglia, M., and Gualtieri, L. (2006b). Hawking emission of gravitons in higher dimensions: non-rotating black holes. *Journal of High Energy Physics*, 0602:021. `arXiv:hep-th/0512116v3`. 12, 30, 31

Chan, J. S. F. and Mann, R. B. (1997). Scalar wave falloff in asymptotically anti-de sitter backgrounds. *Physical Review D*, 55:7546. `arXiv:gr-qc/9612026v1`. 17

Chen, S., Wang, B., Su, R., , and Hwang, W.-Y. P. (2008). Greybody factors for rotating black holes on codimension-2 branes. *Journal of High Energy Physics*, 03:019. `arXiv:0711.3599v2 [hep-th]`. 11

Chen, S., Wang, B., and Su, R.-K. (2007). Wave dynamics of a six-dimensional black hole localized on a tensional three-brane. *Physics Letters B*, 647:282. `arXiv:hep-th/0701209v2`. viii, 11, 14, 15, 18, 22, 23, 28, 75

Chew, G. F. (1966). *The Analytic S-Matrix: A Basis for Nuclear Democracy*. W.A.Benjamin, Inc. 5

Cho, H. T. (2006). Asymptotic quasinormal frequencies of different spin fields in spherically symmetric black holes. *Physical Review D*, 73:024019. `arXiv:gr-qc/0512052v2`. 40, 48

Cho, H. T., Cornell, A. S., Doukas, J., , and Naylor, W. (2007). Split fermion quasi-normal modes. *Physical Review D*, 75:104005. `arXiv:hep-th/0701193`. 44

Cho, H. T., Cornell, A. S., Doukas, J., , and Naylor, W. (2008a). *Physical Review D*, 77:016004. `arXiv:0709.1661`. 44

Cho, H. T., Cornell, A. S., Doukas, J., and Naylor, W. (2008b). Fermion excitations of a tense brane black hole. *Physical Review D*, 77(4):041502. `arXiv:0710.5267v1 [hep-th]`. 15

Creek, S., Efthimiou, O., Kanti, P., and Tamvakis, K. (2006). Graviton emission in the bulk from a higher-dimensional schwarzschild black hole. *Physics Letters B*, 635(1):39. `arXiv:hep-th/0601126v2`. 30, 33

Cutkosky, R. E. (1960). Some applications of the generalized unitarity relation. *Physical Review Letters*, 4(12):624–626. 5

Cvetic, M. and Larsen, F. (1998). Greybody factors for black holes in four dimensions: Particles with spin. *Physical Review D*, 57:6297. `arXiv:hep-th/9712118v1`. 12

Dai, D.-C., Kaloper, N., Starkman, G., and Stojkovic, D. (2007). *Physical Review D*, 75:024043. `arXiv:hep-th/0611184v3`. 11, 14, 15, 18, 28, 38, 75

Dai, D.-C., Starkman, G., Stojkovic, D., Issever, C., Rizvi, E., and Tseng, J. (2008). BlackMax: A black-hole event generator with rotation, recoil, split branes and brane tension. *Phys. Rev.*, D77:076007. `arXiv:0711.3012 [hep-th]`. 76

Dimopoulos, S. and Landsberg, G. (2001). Black holes at the lhc. *Physical Review Letters*, 87:161602. arXiv:hep-ph/0106295v1. 18

Ellis, R. K., Kunszt, Z., Melnikov, K., and Zanderighi, G. (2011). One-loop calculations in quantum field theory: from feynman diagrams to unitarity cuts. `arXiv:1105.4319v1 [hep-ph]`. 7

Emparan, R., Horowitz, G. T., and Myers, R. C. (2000). Black holes radiate mainly on the brane. *Physical Review Letters*, 85:499. `arXiv:hep-th/0003118`. 18, 37

Feynman, R. P. (1963). Quantum theory of gravitation. *Acta Phys. Polon.*, 24:697–722. 5

Gervais, J. L. and Neveu, A. (1972). Feynman rules for massive gauge fields with dual diagram topology. *Nuclear Physics B*, 46(2):381–401. 66

Giddings, S. B. and Thomas, S. (2002). High energy colliders as black hole factories: The end of short distance physics. *Physical Review D*, 65:056010. `arXiv:hep-ph/0106219v4`. 10, 18

Hahn, T. (2001). Generating feynman diagrams and amplitudes with feynarts 3. *Computer Physics Communications*, 140:418–431. `arXiv:hep-ph/0012260v2`. 101

Hahn, T. and Pérez-Victoria, M. (1999). Automated one-loop calculations in four and d dimensions. *Computer Physics Communications*, 118:153–165. `arXiv:hep-ph/9807565`. 102

Harris, C. M., Richardson, P., and Webber, B. R. (2003). CHARYBDIS: A black hole event generator. *JHEP*, 08:033. `arXiv:hep-ph/0307305`. 76

Hawking, S. W. (1975). Particle Creation by Black Holes. *Commun. Math. Phys.*, 43:199–220. 29

Horowitz, G. T. and Hubeny, V. (2000). Quasinormal modes of ads black holes and the approach to thermal equilibrium. *Physical Review D*, 62:024027. `arXiv:hep-th/9909056`. 17

Ida, D., Oda, K., and Park, S. C. (2003). Rotating black holes at future colliders: Greybody factors for brane fields. *Physical Review D*, 67:064025. `arXiv:hep-th/0212108v4`. 30

Ida, D., Oda, K., and Park, S. C. (2005). Anisotropic scalar field emission from tev scale black hole. `arXiv:hep-ph/0501210v1`. 30

Immirzi, G. (1997). Quantum gravity and regge calculus. *Nuclear Physics B (Proc. Suppl.)*, 57:65. `arXiv:gr-qc/9701052`. 17

Ishibashi, A. and Kodama, H. (2003). A master equation for gravitational perturbations of maximally symmetric black holes in higher dimensions. *Progress of Theoretical Physics*, 110:701. `arXiv:hep-th/0305147v3`. 11, 31

Iyer, S. and Will, C. M. (1987). Black hole normal modes: A wkb approach. 1. foundations and application of a higher order wkb analysis of potential barrier scattering. *Physical Review D*, 35(12). 19

Jung, E. and Park, D. K. (2007). Bulk versus brane emissivities of photon fields: For the case of higher-dimensional schwarzschild phase. *Nuclear Physics B*, 766:269. `arXiv:hep-th/0610089v3`. 37, 49

Kaloper, N. and Kiley, D. (2006). Exact black holes and gravitational shockwaves on codimension-2 branes. *Journal of High Energy Physics*, 0603:77. `arXiv:hep-th/0601110v2`. 10, 25, 74

Kane, G. and Pierce, A., editors (2008). *Perspectives on LHC Physics*. World Scientific Publishing, Reading, Massachusetts. 1

Kanti, P. (2004). Black holes in theories with large extra dimensions: a review. *International Journal of Modern Physics A*, 19:4899. `arXiv:hep-ph/0402168v2`. 9, 18

Kanti, P. and Konoplya, R. A. (2006). Quasi-normal modes of brane-localised standard model fields. *Physical Review D*, 73:044002. `arXiv:hep-th/0512257v2`. 18

Kanti, P., Konoplya, R. A., and Zhidenko, A. (2006). Quasi-normal modes of brane-localised standard model fields ii: Kerr black holes. *Physical Review D*, 74:064008. `arXiv:gr-qc/0607048v3`. 9, 18

Kanti, P. and March-Russell, J. (2002). Calculable corrections to brane black hole decay i: The scalar case. *Physical Review D*, 66:024023. `arXiv:hep-ph/0203223v2`. 30, 33

Karasik, D., Sahabandu, C., Suranyi, P., and Wijewardhana, L. C. R. (2005). Analytic approximation to 5 dimensional black holes with one compact dimension. *Physical Review D*, 71(2):024024. `arXiv:hep-th/0410078v2`. 76

Kiley, D. (2007). Rotating black holes on codimension 2 branes. *Physical Review D*, 76(12):126002. `arXiv:0708.1016v1`. 11, 74

Kobayashi, T., Nozawa, M., and Takamizu, Y.-i. (2008). Bulk scalar emission from a rotating black hole pierced by a tense brane. *Physical Review D*, 77(4):044022. `arXiv:0711.1395v4 [hep-th]`. 11

Kokkotas, K. D. and Schmidt, B. (1999). Quasi-normal modes of stars and black holes. *Living Reviews in Relativity*, 2:2. `arXiv:gr-qc/9909058v1`. 17

Landsberg, G. (2000). Mini-review on extra dimensions. `arXiv:hep-ex/0009038v1`. 3

Landsberg, G. (2006). Black holes at future colliders and beyond: a topical review. *Journal of Physics G*, 32:R337. `arXiv:hep-ph/0607297v1`. 18

Middleton, C. and Siopsis, G. (2005). Constrained perturbative expansion of the DGP model. *Physics Letters*, B613:189–196. `arXiv:hep-th/0502020`. 76

Motl, L. and Neitzke, A. (2003). Asymptotic black hole quasinormal frequencies. *Adv. Theor. Math. Phys.*, 7(2). `arXiv:hep-th/0301173v4`. 40

Musiri, S. and Siopsis, G. (2003). Perturbative calculation of quasi-normal modes of schwarzschild black holes. *Classical and Quantum Gravity*, 20(24):L285. `arXiv:hep-th/0308168v2`. 41

Myers, R. C. and Perry, M. J. (1986). Black holes in higher dimensional space-times. *Annals of Physics*, 172(2):304 – 347. 3

Neitzke, A. (2003). Greybody factors at large imaginary frequencies. `arXiv:hep-th/0304080`. 48

Nollert, H. (1999). Topical review: Quasinormal modes: The characteristic 'sound' of black holes and neutron stars. *Classical and Quantum Gravity*, 16:R159. 17

Olive, D. I. (1964). Exploration of S-Matrix Theory. *Physical Review*, 135:745–760. 5

P. Kanti, J. M.-R. (2003). Calculable corrections to brane black hole decay ii: Greybody factors for spin 1/2 and 1. *Physical Review D*, 67:104019. `arXiv:hep-ph/0212199v3`. 12, 30, 36, 37

Park, D. K. (2006). *Physics Letters B*, 633:613. 49, 51

Passarino, G. and Veltman, M. J. G. (1979). One loop corrections for e+ e- annihilation into mu+ mu- in the weinberg model. *Nuclear Physics B*, 160(151):87. 95

Peskin, M. and Schroeder, D. (1995). *Introduction to Quantum Field Theory*. Persus Books Publishing, Reading, Massachusetts. 94

Randall, L. and Sundrum, R. (1998). A large mass hierarchy from a small extra dimension. *Physical Review Letters*, 83:3370, 4690. `arXiv:hep-ph/9905221v1`. 4

Rovelli, C. (1998). Loop quantum gravity. *Living Reviews in Relativity*, 1:1. 18

Rovelli, C. and Smolin, L. (1995). Discreteness of area and volume in quantum gravity. *Nuclear Physics B*, 442:593. `arXiv:gr-qc/9411005`. 18

't Hooft, G. and Veltman, M. (1972). Regularization and renormalization of gauge fields. *Nuclear Physics B*, 44(1):189–213. 90

't Hooft, G. and Veltman, M. (1974). One-loop divergencies in the theory of gravitation. *Annales de l'Institut Henri Poincaré*, 20(1):25. 7

Tangherlini, F. (1963). Schwarzschild field in n dimensions and the dimensionality of space problem. *Il Nuovo Cimento (1955-1965)*, 27:636–651. 10.1007/BF02784569. 3

Teukolsky, S. A. (1973). Perturbations of a Rotating Black Hole. I. Fundamental Equations for Gravitational, Electromagnetic, and Neutrino-Field Perturbations. *Astrophysical Journal*, 185:635–648. 12

van den Brink, A. M. (2004). Wkb analysis of the regge?wheeler equation down in the frequency plane. 45(1):327–335. `arXiv:gr-qc/0303095v4`. 41

Witten, E. (2004). Perturbative gauge theory as a string theory in twistor space. *Communications in Mathematical Physics*, 252:189–258. `arXiv:hep-th/0312171v2`. 7, 56

Yano, T., Ezawa, Y., Wada, T., and Ezawa, H. (2003). Can milne's method work well for the coulomb-like potentials? *Journal of Computational and Applied Mathematics*, 152(1-2):597 – 611. *Proceedings of the International Conference on Recent Advances in Computational Mathematics*. 15

Appendix

Appendix A

Calculation of One-Loop Integrals

A.1 Dimensional Regularization

The one-loop integrals appearing in Chapter 5 were calculated using standard dimensional regularization of 't Hooft and Veltman (1972) and Feynman parametrization. What follows is a summary of the method as well as a table of integrals used. We begin by stating the general form of a typical integral in a 1-loop calculation corresponding to the generic diagram in figure (A.1):

$$I_n = \int \frac{d^4\ell}{(2\pi)^4} \frac{\mathcal{N}(\ell)}{[(\ell + q_0)^2 - m_1^2]\,[(\ell + q_1)^2 - m_2^2] \ldots [(\ell + q_{n-1})^2 - m_n^2]} \tag{A.1}$$

where n is the number of external legs and $\mathcal{N}(\ell)$ is a polynomial function of loop momentum ℓ as well as the external momenta $\{k_i\}$ and polarization vector. Also,

$$q_i = \sum_{j=1}^{i} k_j \tag{A.2}$$

and by momentum conservation we have:

$$\sum_{j=1}^{n} k_j = 0 \tag{A.3}$$

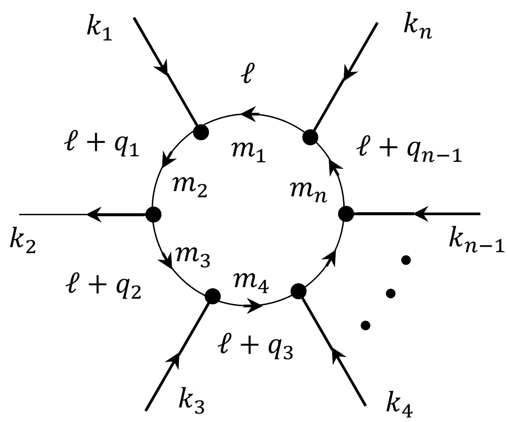

Figure A.1: Generic 1-loop n-point diagram

By power counting, the above integral could be ultra-violet divergent, in which case we need to regularize it. And we do so by considering the number of dimensions of space-time D to be

$$D = 4 - \varepsilon, \qquad 0 \leq \varepsilon \ll 1 \tag{A.4}$$

The regularized integral looks like this:

$$I_n = \int \frac{d^D\ell}{(2\pi)^D} \frac{\mathcal{N}(\ell)}{[(\ell + q_0)^2 - m_1^2]\,[(\ell + q_1)^2 - m_2^2] \ldots [(\ell + q_{n-1})^2 - m_n^2]} \tag{A.5}$$

After integration, we take the limit $\varepsilon \to 0$. As a sample calculation we will fully perform the simplest of these integrals, viz., the so-called tadpole, or 1-point scalar integral I_1, in which the numerator is $\mathcal{N}(\ell) = 1$, and the denominator comes from a single propagator:

$$I_1 = \int \frac{d^D\ell}{(2\pi)^D} \frac{1}{\ell^2 - m^2 + i\delta} \tag{A.6}$$

We will perform this integral in the complex plane of the variable ℓ^0 shown in figure

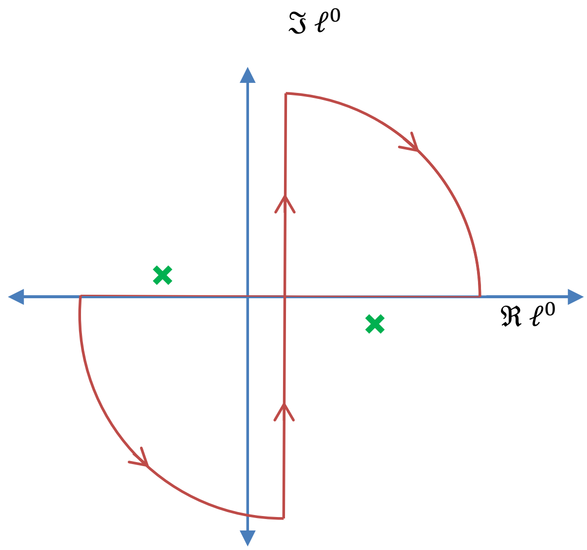

Figure A.2: Wick rotation contour

(A.2). We may rewrite this as:

$$I_1 = \int \frac{d^{D-1}\ell}{(2\pi)^D} \int d\ell^0 \frac{1}{\ell_0^2 - |\vec{\ell}|^2 - m^2 + i\delta} \tag{A.7}$$

The integrand has two complex poles $\ell^0_\pm = \pm\sqrt{|\vec{\ell}|^2 + m^2} \mp i\delta$. Using Cauchy's theorem we can switch the integration from the real axis to the imaginary:

$$\ell^0 \to i\ell^0_{\mathrm{E}} \Rightarrow \int_{-\infty}^{+\infty} d\ell^0 \to i \int_{-\infty}^{+\infty} d\ell^0_{\mathrm{E}} \tag{A.8}$$

Therefore we replace the Minkowski 4-vector with a Euclidean 4-vector:

$$\ell^2 = \left(\ell^0\right)^2 - |\vec{\ell}|^2 = -\left(\ell^0_{\mathrm{E}}\right)^2 - |\vec{\ell}|^2 \equiv -\ell^2_{\mathrm{E}} \tag{A.9}$$

Our integral becomes:

$$I_1 = -i \int \frac{d^D\ell_E}{(2\pi)^D} \frac{1}{\ell_E^2 + m^2} \tag{A.10}$$

where the $i\delta$ is no longer necessary with the denominator becoming positive-definite. Let $\bar{\ell} = \sqrt{(\ell_{\mathrm{E}}^0)^2 + |\vec{\ell}|^2}$, then:

$$\int d^D\ell_E = \int d\bar{\ell}\bar{\ell}^{D-1}d\Omega_{D-1} \tag{A.11}$$

To find the solid angle Ω_D we can start by noticing the following:

$$\sqrt{\pi} = \int_0^\infty dx e^{-x^2} \tag{A.12}$$

Therefore:

$$\begin{aligned}\left(\sqrt{\pi}\right)^D &= \left(\int_0^\infty dx e^{-x^2}\right)^D = \int_0^\infty dx^1 \ldots dx^D e^{-\sum_{i=1}^D x_i^2} \\ &= \int d\Omega_D \int_0^\infty dx x^{D-1} e^{-x^2}\end{aligned} \tag{A.13}$$

Using the definition of the Γ function:

$$\Gamma(z) = 2\int_0^\infty dx x^{2z-1} e^{-x^2}, \tag{A.14}$$

we see that:

$$\Omega_D = 2\frac{\pi^{D/2}}{\Gamma(D/2)} \tag{A.15}$$

Therefore:

$$I_1 = -2\frac{\pi^{D/2}}{\Gamma(D/2)}\frac{i}{(2\pi)^D}\int_0^\infty dx \frac{x^{D-1}}{x^2+m^2} \tag{A.16}$$

The integral is doable using the beta function:

$$B(x,y) = \int_0^\infty dt \frac{t^{x-1}}{(1+t)^{x+y}} = \frac{\Gamma(x)\Gamma(y)}{\Gamma(x+y)} \tag{A.17}$$

Using the substitution $u = x^2/m^2$, we have:

$$
\begin{aligned}
\int_0^\infty dx \frac{x^{D-1}}{x^2+m^2} &= \frac{1}{2}\left(\sqrt{m^2}\right)^{D-2} \int_0^\infty du \frac{u^{\frac{D}{2}-1}}{1+u} \\
&= \frac{1}{2}\left(\frac{1}{m^2}\right)^{1-\frac{D}{2}} \Gamma(D/2)\Gamma(1-D/2)
\end{aligned}
\tag{A.18}
$$

$$
\therefore I_1 = -i\frac{1}{(4\pi)^{D/2}}\left(\frac{1}{m^2}\right)^{1-\frac{D}{2}} \Gamma(1-D/2) \tag{A.19}
$$

If we look at the general case of the numerator function $\mathcal{N}(\ell)$, after stripping away the external momenta and polarization vectors and any spinors, we end up with polynomials of ℓ^μ. Let us restrict ourselves to forms containing products of no more than $4\ell^\mu$. Further, as we will see in examples below, the denominator of the original 1-loop integral can be reduced using Feynman parametrization to the form $(q^2-\Delta)^n$, where q is related to ℓ via a linear shift. This means that after rewriting the integral in Euclidean coordinates, and using symmetry, products in the numerator made up of an odd number of q^μ would vanish. Then following arguments similar to what we did above, it is possible to find other integrals that will be useful in evaluating other integrals coming from the original 1-loop integral. We list them, mainly, following, for example, Peskin and Schroeder (1995):

$$
\int \frac{d^Dq}{(2\pi)^D}\frac{\left(q^2\right)^r}{\left(q^2-\Delta\right)^s} = \frac{(-1)^{r-s}i}{(4\pi)^{D/2}}\frac{\Gamma\left(r+\frac{D}{2}\right)}{\Gamma\left(\frac{D}{2}\right)}\frac{\Gamma\left(s-r-\frac{D}{2}\right)}{\Gamma(s)}\left(\frac{1}{\Delta}\right)^{s-r-\frac{D}{2}} \tag{A.20}
$$

$$
\int \frac{d^Dq}{(2\pi)^D}\frac{q^\mu q^\nu}{\left(q^2-\Delta\right)^s} = \frac{(-1)^{s-1}i}{(4\pi)^{D/2}}\frac{\eta^{\mu\nu}}{2}\frac{\Gamma\left(s-\frac{D}{2}-1\right)}{\Gamma(s)}\left(\frac{1}{\Delta}\right)^{s-1-\frac{D}{2}} \tag{A.21}
$$

$$
\begin{aligned}
\int \frac{d^Dq}{(2\pi)^D}\frac{q^\mu q^\nu q^\rho q^\sigma}{\left(q^2-\Delta\right)^s} &= \frac{(-1)^{s}i}{(4\pi)^{D/2}}\frac{\Gamma\left(s-\frac{D}{2}-2\right)}{\Gamma(s)}\left(\frac{1}{\Delta}\right)^{s-2-\frac{D}{2}} \\
&\times \frac{1}{4}\left(\eta^{\mu\nu}\eta^{\rho\sigma}+\eta^{\mu\rho}\eta^{\nu\sigma}+\eta^{\mu\sigma}\eta^{\nu\rho}\right)
\end{aligned}
\tag{A.22}
$$

The last two are actually reducible to the first of these, which can be seen by noticing that by symmetry, the tensor structure in the numerator can be expressed in terms of the metric:

$$q^\mu q^\nu \longrightarrow \frac{1}{D} q^2 \eta^{\mu\nu} \tag{A.23}$$

$$q^\mu q^\nu q^\rho q^\sigma \longrightarrow \frac{1}{D(D+2)} \left(q^2\right)^2 \left(\eta^{\mu\nu}\eta^{\rho\sigma} + \eta^{\mu\rho}\eta^{\nu\sigma} + \eta^{\mu\sigma}\eta^{\nu\rho}\right) \tag{A.24}$$

In fact, it can be shown that any tensor integral is reducible to a set of scalar integrals. One popular scheme to do this is the one due to Passarino and Veltman (1979), whereby a tensor integral is written in terms of momenta and the metric tensor. For instance, if we call the integral on the left-hand-side of (A.21) $B^{\mu\nu}$, then we may write:

$$B^{\mu\nu} = B_{00}\eta^{\mu\nu} + B_{11} k_1^\mu k_2^\nu \tag{A.25}$$

The coefficients B_{00} and B_{11} are found by contracting this once with $\eta_{\mu\nu}$ and second time with $(k_1)_\mu (k_2)_\nu$.

Finally, because of the central role played by (A.20), it is worth noting that to ensure convergence we must have $D < 2(s-r)$. However, we can analytically continue that formula for all values of D except at the poles of $\Gamma(s-r-D/2)$.

A.2 Feynman Parametrization

The method we used to reduce integrals to ones like those in equations (A.20-A.22) was the Feynman parametrization method, which is based on the following general formula:

$$\frac{1}{A_1 A_2 \ldots A_n} = \int_0^1 dx_1 dx_2 \ldots dx_n \delta\left(1 - \sum_{i=1}^n x_i\right) \times \frac{(n-1)!}{\left[x_1 A_1 + x_2 A_2 + \ldots + x_n A_n\right]^n} \tag{A.26}$$

Appendix B

QCD Reference Information

B.1 QCD Color Identities

While the following were not used explicitly in the body of the work, they were used in the Mathematica implementation to simplify color factors:

$$\left[T^a, T^b\right] = i f^{abc} T^c \tag{B.1}$$

$$f^{ade} f^{bcd} + f^{bde} f^{cad} + f^{cde} f^{abd} = 0 \tag{B.2}$$

$$f^{abc} = -2i \left(\mathrm{Tr}\left[T^a T^b T^c\right] - \mathrm{Tr}\left[T^a T^c T^b\right]\right) \tag{B.3}$$

$$\mathrm{Tr}\left(T^a T^b\right) = \frac{1}{2}\delta^{ab} \tag{B.4}$$

$$f^{abc} f^{abd} = N_c \delta^{cd} \tag{B.5}$$

where N_c is the number of colors.

$$f^{ahi} f^{bhj} f^{cde} f^{eij} = \frac{3}{2} f^{abe} f^{cde} \tag{B.6}$$

Most of the time it was possible to check the results of such manipulations against `FormCalc`'s output, which was in terms of traces or double traces.

B.2 QCD Feynman Rules

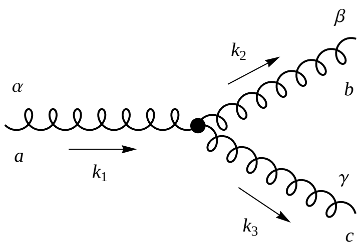

$$V^{a\,b\,c}_{\alpha\,\beta\,\gamma} = -i\,g_s\,f^{a\,b\,c}\Big[-(k_1-k_2)_\gamma\,\eta_{\alpha\,\beta} + (k_1+k_3)_\beta\,\eta_{\alpha\,\gamma} + (k_2-k_3)_\alpha\,\eta_{\beta\,\gamma}\Big]$$

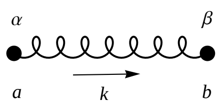

$$P^{a\,b}_{\alpha\,\beta} = -\frac{i\,\delta^{a\,b}}{k^2+i\,0}\left(\eta_{\alpha\,\beta} + (\xi-1)\,\frac{k_\alpha\,k_\beta}{k^2+i\,0}\right)$$

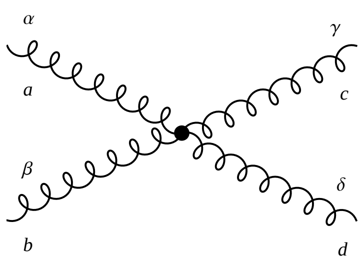

$$U^{a\,b\,c\,d}_{\alpha\,\beta\,\gamma\,\delta} = i\,g_s^2\Big[f^{a\,b\,e}\,f^{e\,c\,d}\big(\eta_{\alpha\,\delta}\,\eta_{\beta\,\gamma} - \eta_{\alpha\,\gamma}\,\eta_{\beta\,\delta}\big) + f^{a\,c\,e}\,f^{e\,b\,d}\big(\eta_{\alpha\,\delta}\,\eta_{\beta\,\gamma} - \eta_{\alpha\,\beta}\,\eta_{\gamma\,\delta}\big) + f^{a\,d\,e}\,f^{e\,c\,b}\big(\eta_{\alpha\,\beta}\,\eta_{\gamma\,\delta} - \eta_{\alpha\,\gamma}\,\eta_{\beta\,\delta}\big)\Big]$$

Figure B.1: QCD Feynman rules used by `FeynArts` for gluons.

B.3 4-gluon 1-loop diagrams

Following are the diagrams that results for the topology of one loop and four legs. Originally they number 99, but by excluding tadpoles we end up with 74.

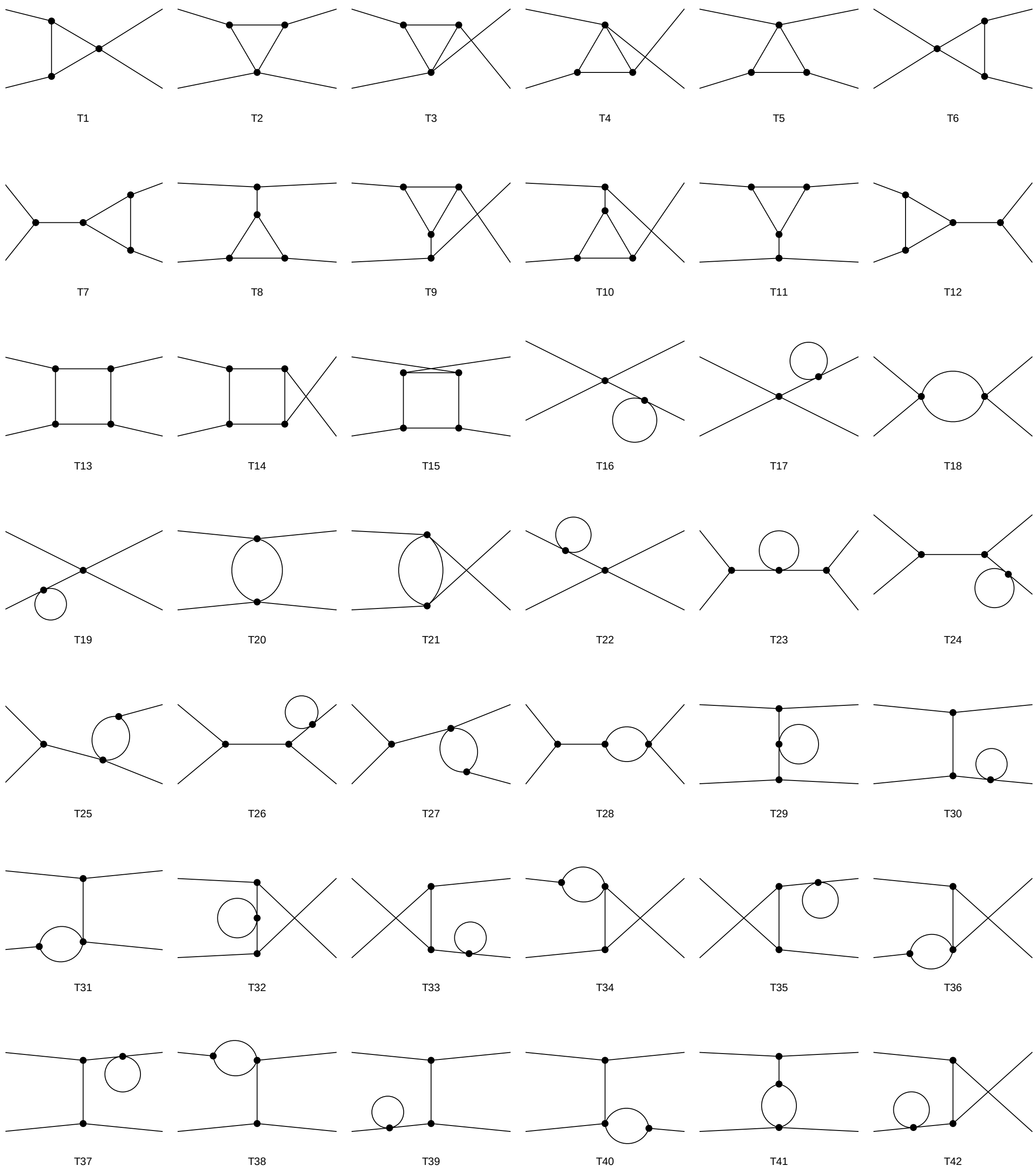

Figure B.2: 4-point diagrams 1 through 42

2 → 2

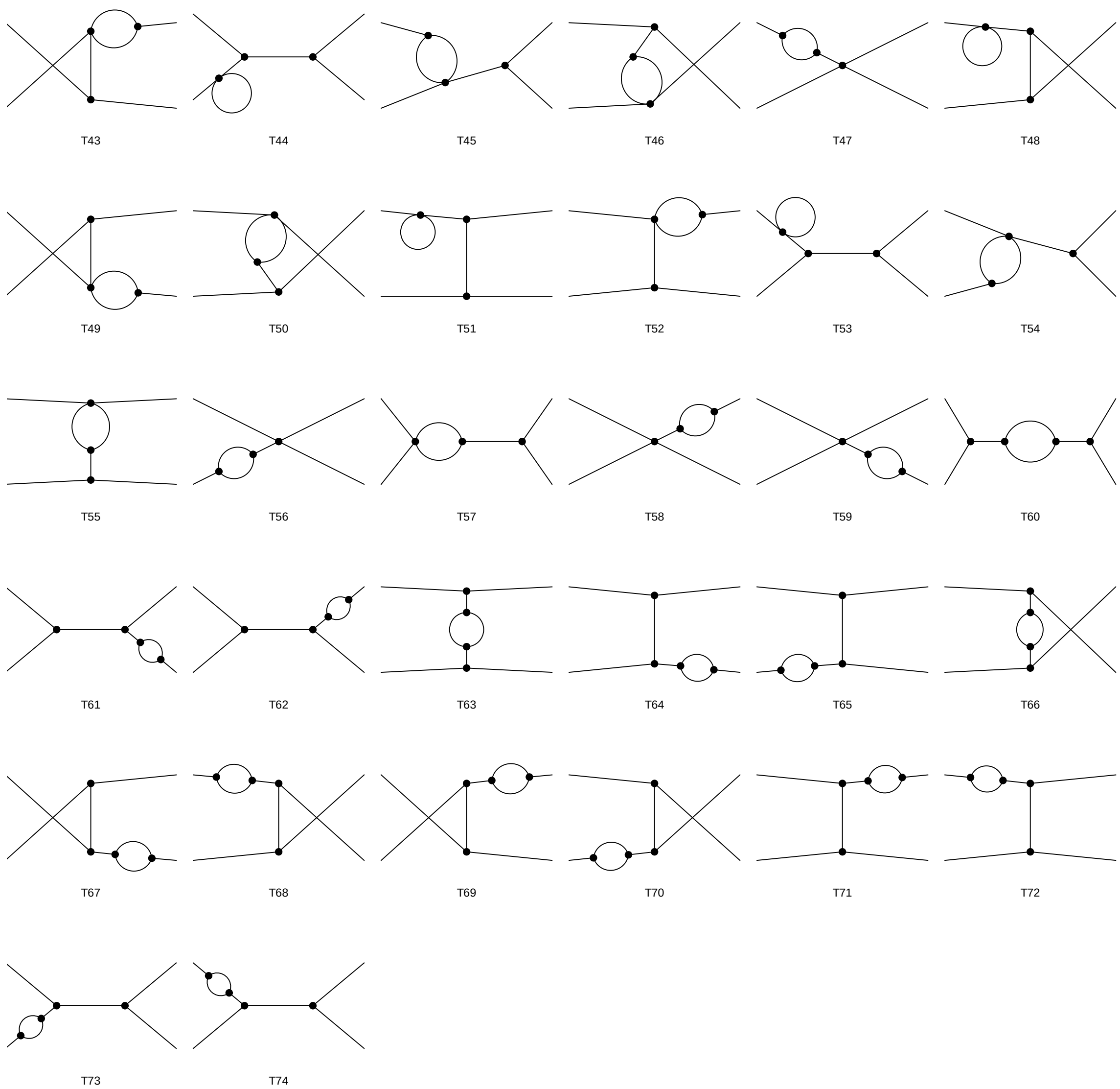

Figure B.3: 4-point diagrams 43 through 74

Appendix C

Mathematica Conventions and Sample Listings

A great deal of computations throughout this work relied on Wolfram's Mathematica system and some additional external software written in the Mathematica language, but also in the production of graphics and other miscellaneous uses.

For the case of calculating scattering amplitudes in Chapter A, both `FeynArts` and `FormCalc` were used. However, their raw output was not very useful generally without further processing. In particular, we needed an intermediate form of the expressions between `FeynArts`'s unevaluated expressions and `FormCalc`'s evaluated final ones. To do so, the output of `FeynArts` was processed to contract Lorentz and color indices, whenever possible, and the resulting expressions were then put into standard Mathematica form for further manipulation, such as imposing polarization conditions or performing complex shifts. In that form it was then possible to also perform Feynman parametrization and integration when needed. `FormCalc` was used mainly to quickly eliminate vanishing diagrams from consideration and to provide cross-checks for what was obtained by processing `FeynArts` expressions.

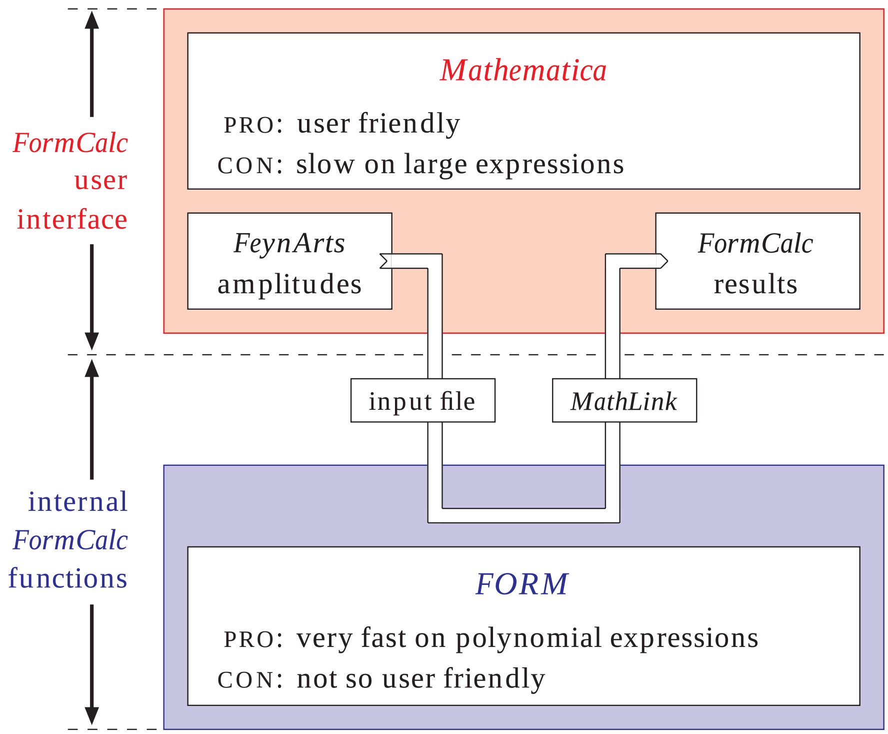

Figure C.1: Roles played by Mathematica, `FeynArts`, and `FormCalc` in a given calculation. *Figure adapted from `FormCalc` manual*

C.1 Mathematica Add-On Software Used

C.1.1 `FeynArts`

`FeynArts` is Mathematica Add-on designed to generate and manipulate Feynman diagrams. At the time of this writing the latest version was 3.6, and version 3.0 was first introduced in Hahn (2001). The program is covered by the GNU library general public license and obtainable for free from `http://www.feynarts.de/`.

The output of `FeynArts` takes the form of expressions representing the diagrams in their most general form, so that no indices are contracted, and no integrals are evaluated.

C.1.2 FormCalc

FormCalc is another Mathematica Add-on developed by the same group that made FeyArts. FormCalc is made to process diagrams calculated by FeynArts by calculating integrals and contracting indices. It is based on FORM, and uses it as back-end to manipulate and perform fast symbolic calculations. FormCalc is another GPL software and can be obtained from http://www.feynarts.de/formcalc. More information about FORM can be found at http://www.nikhef.nl/~form/.

C.1.3 LoopTools

LoopTools is an additional piece of software that integrates into the FeynArts and FormCalc suite, and is used to evaluate loop integrals numerically. It was only used infrequently to check results against those obtained in different methods. The program was first introduced in Hahn and Pérez-Victoria (1999), and can be obtained for free from http://www.feynarts.de/looptools/.

C.2 Sample *Mathematica* Listings

C.2.1 Function Definitions For FeynArts and FormCalc

The following function definitions were invoked before using FeynArts and FormCalc. Their aim was to translate the output of these two packages into forms that can be manipulated algebraically by Mathematica. They also contract indices and perform a couple of more auxiliary tasks.

```
FeynArtsToMath[amp_]:=Block[{glu={a,b,c,d,e,h,i,j},lor={\[Alpha],\[
    Beta],\[Gamma],\[Delta],\[Lambda],\[Mu],\[Nu],\[Rho],\[Sigma],\[
    Tau],\[Upsilon],\[Chi],\[Zeta],\[Xi]},ind,k,p,x,y,z,\[Alpha]\[
    Alpha],\[ScriptL],f},(Strip[amp]//.{Index[Gluon,ind_]:>glu[[ind
    ]],Index[Lorentz,ind_]:>lor[[ind]],Alfas:>GS^2/(4\[Pi]),
    MetricTensor->\[Eta],SumOver[x___]->1,SUNF[a_,b_,c_,d_]->f[a,b,
    ind]f[ind,c,d],SUNF[a_,b_,c_]->f[a,b,c],FourMomentum[Outgoing,
    ind_]->k[ind],FourMomentum[Incoming,ind_]->p[ind],FourMomentum[
    Internal,ind_]->\[ScriptL][ind],FourVector[Plus[x_,y_],\[Alpha]\[
    Alpha]_]->FourVector[x,\[Alpha]\[Alpha]]+FourVector[y,\[Alpha]\[
    Alpha]],FourVector[Times[x_,z_],y_]->x z[y],PolarizationVector[V
    [5,List[a_]],p[ind_],\[Alpha]\[Alpha]_]->\[Epsilon][ind][\[Alpha
    ]\[Alpha]],Conjugate[PolarizationVector][V[5,List[c_]],k[ind_],\[
    Alpha]\[Alpha]_]->\[Epsilon]c[ind][\[Alpha]\[Alpha]]})/.
    FourVector[x_,\[Alpha]\[Alpha]_]->x[\[Alpha]\[Alpha]]]
Strip[x_]:=Block[{w},x/.{FeynAmpList[y__][FeynAmp[u_,v_,w__]]->w,Amp
    [y__][w__]->w}]
Reducef[x___]:=(x/.{f[a_,b_,c_]:>Sort[f[a,b,c]] Signature[{a,b,c}]})
    /.f[s1_,t1_,t2_]f[s2_,t1_,t2_]:>3KroneckerDelta[s1,s2]
FeynDen[x___]:=x/.{FeynAmpDenominator->Times,PropagatorDenominator[
    y_,0]:>1/ff[y]}
Contract[amp_,amp2_:1]:=Block[{x,y,z,\[Alpha],\[Beta],A,B,ind1,ind2
    },Simplify[Expand[amp*amp2]//.{FourVector[x_,\[Alpha]_]->x[\[
    Alpha]],\[Eta][x_,y_]\[Eta][x_,z_]->Sort[\[Eta][y,z]],\[Eta][y_,
    x_]\[Eta][x_,z_]->Sort[\[Eta][y,z]],\[Eta][y_,x_]\[Eta][z_,x_]->
    Sort[\[Eta][y,z]],\[Eta][x_,y_]^2->4,\[Eta][x_,x_]->4,B_[ind1_
    ][\[Beta]_]A_ \[Eta][\[Alpha]_,\[Beta]_]->A B[ind1][\[Alpha]],B_[
    ind1_][\[Beta]_] A_ \[Eta][\[Beta]_,\[Alpha]_]->A B[ind1][\[Alpha
    ]],A_[ind1_][\[Alpha]_]B_[ind2_][\[Alpha]_]->Pair[A[ind1],B[ind2
    ]],B_[ind1_][\[Beta]_]^2->Pair[B[ind1],B[ind1]],Pair[A_[ind1_],B_
    [ind2_]]->Sort[Pair[A[ind1],B[ind2]]]}]]
ff[gg_]:=Block[{\[Sigma]=ToExpression["\[Alpha]"<>ToString[Random[
    Integer,{1,1000}]]]},(gg gg)/.x_[n_]->x[n][\[Sigma]]]
cntrct[x___]:=Contract[Numerator[Together[x]]]/Contract[Denominator[
    Together[x]]]
```

C.2.2 2-point Diagrams using `FeynArts`

The following listing finds 2-point all-gluon diagrams and calculates the amplitudes. Two types of calculations are performed, one with polarization vectors, designated `amp1a[]`, and one with uncontracted external indices, `amp1[]`. The final outcome used the latter, but the uncontracted one was used to manipulate loop integrands to look like trees by contracting some indices with polarization vectors and others with propagators.

```
top1=CreateTopologies[1,1->1];
Paint[top1,ColumnsXRows->{3,1}]
Do[ins1[i]=InsertFields[top1[[i]],V[5]->V[5],Model->SMQCD,
   InsertionLevel->{Particles},ExcludeParticles->{F[1],F[2],F[3],F
   [4],V[1],V[2],V[3],U[5]}];Print["Diagram_",i];
Paint[ins1[i],ColumnsXRows->1];
Print[amp1[i]=CreateFeynAmp[ins1[i],Truncated->True]];
Print[amp1a[i]=CreateFeynAmp[ins1[i]]],{i,Length[top1]}];
```

C.2.3 Calculation of the 4-point diagram T_3

This shows part of what has been done to arrive at expression (5.60).

```
A13=Expand[(FullSimplify[(FullSimplify[num[13]//.subs])/(I Alfas2 f[
   a,e,h] f[b,e,i] f[c,h,j] f[d,i,j] )//.subs]/.{Pair[\[ScriptL][1],
   A_[a_]]:>Pair[q[1],A[a]]-y Pair[k[1],A[a]]-(x+z) Pair[k[2],A[a]]+
   x Pair[k[4],A[a]]})//.subs];
B13=Expand[1/2 (A13+(A13/.Pair[q[1],A_[a_]]:>-Pair[q[1],A[a]]))];
C13=Simplify[(B13//.(Pair[q[1],A_[a_]] Pair[q[1],B_[b_]] Pair[cc___]
   Pair[dd___]:>(Pair[q[1],q[1]] Sort[Pair[A[a],B[b]]])/d Pair[cc]
   Pair[dd]/;(FreeQ[{cc},q[1]]&&FreeQ[{dd},q[1]])))//.subs]
D13=Normal[Series[-((2\[Pi])^(4-\[Epsilon])/(4\[Pi])^((4-\[Epsilon])
   /2)) Gamma[4-(4-\[Epsilon])/2]/Gamma[4] (1/(-(2 Pair[k[1],k[4]] x
    y+2 (Pair[k[2],k[4]] x (-1+x+z)-Pair[k[1],k[2]] y (x+z)))))
   ^(4-(4-\[Epsilon])/2),{\[Epsilon],0,1}]]
```

```
T13=Integrate[Integrate[Integrate[(-1/\[Pi]^2 (\[Pi]^2 ((I Alfas2 f[
    a,e,h] f[b,e,i] f[c,h,j] f[d,i,j] ))Simplify[C13+34Pair[q[1],\[
    Epsilon][1]] Pair[q[1],\[Epsilon][2]] Pair[q[1],\[Epsilon]c[1]]
    Pair[q[1],\[Epsilon]c[2]]])/(6 (-2 x y Pair[k[1],k[4]]-2 (-y (x+z
    ) Pair[k[1],k[2]]+x (-1+x+z) Pair[k[2],k[4]]))^2)),{y,0,1-z-x},
    Assumptions->assmpt1],{x,0,1-z},Assumptions->Assumptions->assmpt2
    ],{z,0,1},Assumptions->assmpt2]
```

where, `num[13]` and `den[13]` represent the numerator and denominator of the diagram after contracting indices. `subs` is a set of substitution, among other things imposing polarization assumptions. `assmpt`n are general assumptions necessary for guaranteeing convergence of integrals. `A13` is the actual amplitude with the suitable Feynman parametrization, `B13` and `C13` are used to eliminate odd powers of the momentum, and `D13` expands the Feynman integral in powers of ε. `T13` integrates the Feynman parameters.

Vita

Usama al-Binni was born in Amman, Jordan on February 15, 1976 to Adnan al-Binni and Majida al-Jallad. Right after getting the Jordanian high-school degree (Tawjihi) in 1994 he studied at the University of Jordan and in 1998 obtained a Bachelor of Science in Physics degree. After spending a year as a research assistant at the University of Jordan he enrolled there as a graduate student and obtained a Masters of Science in Physics degree in 2002. He worked as Instructor at the University of Jordan between 2003 and 2005, and in summer of 2005 joined the graduate program at the University of Tennessee in Knoxville and obtained a Doctorate in Physics in 2011.